SEP 23 1986
DATE ISSUED

HTGR-86-057
ORNL-6300

ORNL
MASTER COPY

HTGR

# GAS-COOLED REACTOR PROGRAMS

## HIGH-TEMPERATURE GAS-COOLED REACTOR TECHNOLOGY DEVELOPMENT PROGRAM
## ANNUAL PROGRESS REPORT FOR PERIOD ENDING DECEMBER 31, 1985

[redacted]

**AUTHORS/CONTRACTORS**

**P. R. Kasten et al., Oak Ridge National Laboratory**

Oak Ridge National Laboratory
Oak Ridge, Tennessee 37831
operated by
MARTIN MARIETTA ENERGY SYSTEMS, INC.
for the
UNITED STATES DEPARTMENT OF ENERGY
July 1986

Printed in the United States of America. Available from
the U.S. Department of Energy
Technical Information Center
P.O. Box 62, Oak Ridge, Tennessee 37830

This report was prepared as an account of work sponsored by an agency of the United States Government. Neither the United States Government nor any agency thereof, nor any of their employees, makes any warranty, express or implied, or assumes any legal liability or responsibility for the accuracy, completeness, or usefulness of any information, apparatus, product, or process disclosed, or represents that its use would not infringe privately owned rights. Reference herein to any specific commercial product, process, or service by trade name, trademark, manufacturer, or otherwise, does not necessarily constitute or imply its endorsement, recommendation, or favoring by the United States Government or any agency thereof. The views and opinions of authors expressed herein do not necessarily state or reflect those of the United States Government or any agency thereof.

HTGR-86-057
ORNL-6300
Distribution
Category UC-77T

GAS-COOLED REACTOR PROGRAMS

# HIGH-TEMPERATURE GAS-COOLED REACTOR TECHNOLOGY DEVELOPMENT PROGRAM ANNUAL PROGRESS REPORT FOR PERIOD ENDING DECEMBER 31, 1985

John E. Jones Jr., Director of Reactor Programs

Paul R. Kasten, Gas-Cooled Reactor Programs Technical Director

P. L. Rittenhouse, Base Technology Program Manager

J. P. Sanders, Summary Level Program Plan Coordinator

Date Published – July 1986

[redacted]

Prepared by the
OAK RIDGE NATIONAL LABORATORY
Oak Ridge, Tennessee 37831
operated by
MARTIN MARIETTA ENERGY SYSTEMS, INC.
for the
U.S. DEPARTMENT OF ENERGY
under Contract No. DE-AC05-84OR21400

CONTENTS

SUMMARY . . . . . vii

1. ANNUAL PLANNING AND CONTROL . . . . . 1

1.1 INTRODUCTION . . . . . 1

1.2 CHANGE PROPOSALS TO THE FY 1985 SLPP . . . . . 1

1.3 SLPP FOR FY 1986 . . . . . 2

1.4 SUBSEQUENT CHANGE PROPOSALS . . . . . 2

2. REQUIREMENTS MANAGEMENT AND EVALUATION . . . . . 3

2.1 INTRODUCTION . . . . . 3

2.2 RATING OF DIFFERENT SMALL HTGR CONCEPTS . . . . . 3

2.3 ASSESSMENT OF WATER/STEAM INGRESS . . . . . 7

2.4 RATING OF SMALL STEEL VESSEL DESIGNS USING EITHER PEBBLE OR PRISMATIC FUEL . . . . . 8

2.5 MHTGR SHIELDING CONSIDERATIONS . . . . . 9

2.6 IDENTIFICATION OF KEY DESIGN/ANALYSIS AREAS FOR THE MHTGR . 10

3. LICENSING SUPPORT . . . . . 13

3.1 INTRODUCTION . . . . . 13

3.2 LICENSING PLAN . . . . . 13

3.3 TOP LEVEL REGULATORY CRITERIA . . . . . 14

3.4 PSID OUTLINE FOR THE MODULAR HTGR . . . . . 15

3.5 PRINCIPAL DESIGN CRITERIA . . . . . 15

3.6 NRC BRIEFINGS . . . . . 16

4. PROGRAM MANAGEMENT . . . . . 17

5. INTERNATIONAL TECHNOLOGY TRANSFER . . . . . 19

5.1 AVR/KFA/ORNL COOPERATION ON HTR PHYSICS, PERFORMANCE, AND SAFETY . . . . . 19

5.1.1 Analyses of AVR Dynamic Experiments . . . . . 19

5.1.2 Analysis of Flow Reduction Test . . . . . 22

5.1.3 Analysis of Control Rod Withdrawal Test . . . . . 24

5.1.4 Analysis of Flow Increase Test . . . . . 26

5.1.5 Analysis of Rod Insertion Test . . . . . 26

5.1.6 Neutronic Analyses of the AVR . . . . . 29

5.2 COOPERATION ON HTGR BASE TECHNOLOGY . . . . . 30

5.2.1 Cooperation on Fuels . . . . . 30

5.2.2 Petten Tensile Creep Results on H451 Graphite . . . . 31

5.2.3 Cooperation on Materials . . . . . 33

5.3 REFERENCES . . . . . 35
6. FUELS AND FISSION PRODUCT BEHAVIOR . . . . . 37
6.1 INTRODUCTION . . . . . 37
6.1.1 Fuel Materials Qualification Program . . . . . 37
6.2 IRRADIATION CAPSULE ASSEMBLY AND OPERATION . . . . . 38
6.2.1 Capsules HRB-17 and -18 . . . . . 38
6.3 POSTIRRADIATION EXAMINATION OF IRRADIATION EXPERIMENTS . . . 43
6.3.1 Experiment HRB-16 . . . . . 43
6.3.2 Experiment R2-K13 . . . . . 46
6.4 EQUIPMENT DEVELOPMENT AND MAINTENANCE . . . . . 47
6.4.1 The Irradiated Microsphere Gamma Analyzer (IMGA) . . 48
6.4.2 Shielded Electron Microprobe . . . . . 49
6.5 REFERENCES . . . . . 52
7. GRAPHITE . . . . . 53
7.1 GRAPHITE MATERIALS – INTERNALS . . . . . 53
7.1.1 Chemical Impurities in Lots of 2020 Graphite . . . . 53
7.1.2 Inhibition of Oxidation by Silicon . . . . . 58
7.2 GRAPHITE MATERIALS – CORE . . . . . 62
7.2.1 Fracture Testing of Graphite . . . . . 62
7.3 GRAPHITE MATERIALS – TECHNOLOGY . . . . . 65
7.3.1 Considerations in Selection of Multiaxial Failure Criterion for Use in Design of HTR Graphite Components . . . . . 65
7.3.2 Statistical Treatment of the H451 Tensile Strength Data Base . . . . . 86
7.3.3 Modeling the Statistics . . . . . 91
7.4 REFERENCES . . . . . 93
8. MATERIALS ENGINEERING . . . . . 103
8.1 INTRODUCTION . . . . . 103
8.2 MATERIALS TECHNOLOGY PLANNING . . . . . 103
8.3 REACTOR SYSTEM MATERIALS . . . . . 103
8.3.1 Creep and Aging Behavior of Hastelloy X and Alternate Alloys . . . . . 103
8.3.2 Fatigue Behavior of Hastelloy X . . . . . 106
8.4 HEAT TRANSPORT MATERIALS . . . . . 115

8.4.1 Creep, Aging, and Decarburization of 2.25Cr-1 Mo Steel . . . . . 115

8.4.2 Fracture Mechanics . . . . . 116

8.5 REFERENCES . . . . . 127

9. REACTOR VESSEL DESIGN SUPPORT . . . . . 129

9.1 ASSESSMENT OF STEEL PRESSURE VESSELS FOR MODULAR HTGR SYSTEMS . . . . . 129

9.1.1 Background and Scope . . . . . 129

9.1.2 Vessel Material . . . . . 129

10. PLANT OPERATION AND MAINTENANCE . . . . . 131

10.1 INTRODUCTION . . . . . 131

10.2 O&M COST ESTIMATE . . . . . 131

10.3 REFERENCE . . . . . 133

11. REACTOR PHYSICS AND REACTOR SHIELDING . . . . . 135

11.1 INTRODUCTION . . . . . 135

11.2 REACTOR PHYSICS . . . . . 135

11.2.1 Reactivity Effects of Water Ingress Into the Reactor Core . . . . . 135

11.2.2 Comparisons of Reactivity Calculations . . . . . 137

11.2.3 Depletion-Perturbation Theory Application . . . . 138

11.3 REACTOR SHIELDING . . . . . 138

11.3.1 Summary of 1985 Shielding Studies . . . . . 138

11.4 REFERENCES . . . . . 148

12. ADVANCED SYSTEM DESIGN SUPPORT . . . . . 151

12.1 INTRODUCTION . . . . . 151

12.2 ADVANCED METALLIC MATERIALS . . . . . 151

12.2.1 Advanced Materials Technology Assessment . . . . . 151

12.2.2 Creep and Thermal Stability of Advanced Alloys . . 152

12.3 NUCLEAR HEAT SYSTEM DESIGN CRITERIA . . . . . 153

12.4 REFERENCES . . . . . 155

## SUMMARY

### 1. ANNUAL PLANNING AND CONTROL (WBS 0100.02)

The work for the High-Temperature Gas-Cooled Reactor (HTGR) Program at Oak Ridge National Laboratory (ORNL) was performed in accordance with the national Summary Level Program Plan (SLPP) for FY 1985 and FY 1986. This program was directed toward developing the 350-MW(t) modular HTGR (MHTGR), and markup and revisions were submitted to support this concept. Various change proposals leading to this goal were submitted during the year. In April, a draft proposal for FY 1986 was submitted, and revisions were made as appropriate to meet the programmatic objectives and budget guidance provided by the U.S. Department of Energy (DOE).

Following distribution of the SLPP for FY 1986, change proposals were submitted as needed to reflect the needs of the program.

### 2. REQUIREMENTS MANAGEMENT AND EVALUATION (WBS 0200.01)

ORNL participated in the Program Requirements Management (PRM) Task Force, which provides overall program reviews, evaluations, and recommendations to the DOE HTGR Program. In particular, ORNL rated the different small HTGR concepts and recommended that further design efforts concentrate on the side-by-side steel vessel concept. In subsequent evaluations ORNL rated specific conceptual designs utilizing prismatic and pebble fuels, respectively, and, for the concepts evaluated, recommended that the program emphasize further development of the prismatic-fueled HTGR. The major advantage of the latter concept was the higher power output achievable per reactor module for the conceptual designs evaluated.

The reactivity effects of water/steam ingress to the core of the MHTGR were assessed. Factors considered were (1) the reactivity effects due to a reduction in neutron leakage, which affects not only the core reactivity but also the reactivity worth of the control rods located in the graphite reflector, and (2) the core temperature coefficient of reactivity, which is influenced by water ingress events. Based on the recommendations of the PRM Task Force members, further calculations were carried out within the MHTGR Program to evaluate the reactivity influence of water ingress phenomena.

The PRM Task Force addressed the importance of carrying out shielding analyses to provide support to the design of reactor internals and to the design of shielding structures outside the reactor vessel. It was concluded that detailed shielding analyses are an important part of developing the conceptual design of the MHTGR.

Key design/analysis areas that need to be emphasized in the future were identified by ORNL to be experimental measurements of fission product "liftoff" from surfaces and of fission product retention by fuel coatings under postulated accident conditions, shielding analyses in support of reactor internals design, benchmarking of MHTGR reactor physics characteristics, and optimizing the design layout of the reactor system.

## 3. LICENSING SUPPORT (WBS 0300.01)

ORNL has participated in the HTGR Safety and Investment Protection Task Force, which is headed by DOE and includes HTGR Program participants. ORNL has also provided licensing support by reviewing and commenting on documents prepared for meetings of DOE and the U.S. Nuclear Regulatory Commission (NRC) on the MHTGR, and it has participated in NRC briefings. The areas of licensing support activities within the MHTGR Program have included development of the licensing plan, the top level regulatory criteria, an outline of a Preliminary Safety Information Document (PSID), and principal design criteria.

Overall, the licensing plan document has been submitted by DOE to NRC for review and comments, as was the document summarizing the proposed top level regulatory criteria. The PSID outline has been reviewed by NRC, and comments obtained are being evaluated by program participants. The principal design criteria are being developed.

## 4. PROGRAM MANAGEMENT (WBS 1000.01)

Work carried out in this activity concerns overall management of the ORNL HTGR development program and emphasizes management of the base technology efforts of the national HTGR Program. Also involved are the integration of efforts between ORNL and other program participants; review of overall efforts as needed to guide the ORNL program; program planning and scheduling; and issuance of monthly, annual, and milestone reports. During the last year, the HTGR Program office also coordinated an International Atomic Energy Agency Specialists' Meeting at ORNL on gas-cooled reactor safety and accident analysis and prepared a paper summarizing HTGR technology development in the United States for a utility-sponsored international conference on the HTGR held in the Federal Republic of Germany.

## 5. INTERNATIONAL TECHNOLOGY TRANSFER (WBS 1400.01)

Cooperative activities on HTR physics, performance, and safety were carried out with Arbeitsgemeinschaft Versuchs Reaktor (AVR) and Kernforschungsanlage Jülich GmbH (KFA) in Germany. Included in this work was ORNL analysis of dynamic experiments in the AVR reactor involving (1) changes in reactivity resulting from control rod motion with the reactor at power and (2) changes in coolant flow through the core allowing the reactor to achieve a new power level without control rod motion. Also, calculations were performed for an AVR pebble fuel element to compare core physics results over a range of temperatures with versions -IV and -V ENDF/B cross sections.

Approximately 2000 unbonded particles of each of three types of irradiated German HTR fuels are now stored at the hot cells at ORNL. Detailed visual examinations of the particles have been completed, and they are scheduled for examination by irradiated microsphere gamma analyzer (IMGA) in 1986.

The results of 900°C irradiation creep tests performed on H451 graphite at ORNL and at Petten by Germany have been compared. Tensile creep-rate coefficients (Petten experiment) were seen to be less than those determined in compressive tests (ORNL experiment). This type of behavior was not expected and suggests possible experimental errors. Control specimens (unstressed) run in both experiments were examined but provided no solution to the problem; there is no current obvious resolution of this conflict in results.

Cooperative work and technology transfer on HTGR materials are being carried out under international agreements involving the United States, the Federal Republic of Germany, and Switzerland. A meeting was held at KFA Jülich in November to review progress of the cooperative work, plan and coordinate new efforts, and update the Materials Subprogram Plan. Cooperative activities at ORNL during the year involved round-robin testing programs on low-cycle fatigue and fracture mechanics.

## 6. FUELS AND FISSION PRODUCT BEHAVIOR (WBS 1601)

The Fuel Materials and Fission Product Performance Verification Programs at ORNL are part of a national fuel and fission product development effort in close cooperation with GA Technologies (GA).

The ORNL fuel materials program is directed toward the testing of GA-fabricated fuel in irradiation capsules designed, assembled, and operated in ORNL reactors. In addition, extensive postirradiation facilities are available and are employed in the examination of the fuel from the capsule testing.

Irradiation of capsules HRB-17 and -18 began on August 17, 1985. These capsules represent the hydrolysis experiment on UCO fuel particles. In mid-December the capsules had been irradiated for nearly 102 efpd

(100 MW) in the High Flux Isotope Reactor (HFIR). During this period, four moisture injections were introduced into capsule HRB-17, resulting in the hydrolysis of "seeded" design-to-fail UCO fissile fuel. The in-reactor fission gas release from both capsules is being closely monitored to record all increases in fission gas activity caused by the moisture injections.

Postirradiation examination (PIE) efforts were concentrated on completing the analysis of the R2-K13 fuel. Final reports were issued by GA on the R2-K13 and the HRB-16 experiments. These reports contained portions describing the PIE work and analyses performed at ORNL. At the end of the report period, only German irradiated fuel remained in PIE at the High Radiation Level Examination Laboratory.

The irradiated microsphere gamma analyzer (IMGA) facility underwent a major upgrade during this report period, resulting in a significant enhancement of the IMGA capabilities. Major components replaced were the automated particle handler, high-resolution gamma detector, and pulse height analyzer. In addition, a new stereo microscope stage and uninterruptible power supply systems were installed. New software, FORTRAN based, was written for system integration, particle handler operation, data acquisition, and analysis. The upgraded IMGA system was fully operational at the end of the report period.

## 7. GRAPHITE (WBS 1602)

### Internals (WBS 1602.01)

Chemical and physical studies on agglomerated and dispersed impurities found in three lots of 2020 graphite received from The Stackpole Corporation were conducted. Each lot consisted of three billets, one shipment of off-the-shelf 2020 and two of "nuclear quality" graphite for which efforts had been taken to decrease impurity levels.

Agglomerated impurites were found in all lots of 2020 and analyzed in an effort to identify their possible sources and methods of avoiding them. The average size range of the particles was about 0.3 mm. In addition to these particulates, other inorganic ash-forming components were found to be rather more uniformly distributed internally throughout the graphite.

In a further set of studies, the 2020 material was heat treated at 2800 and 3000°C, again indicating that the thermal purification largely removes the impurities with the exception of titanium. These materials were impregnated with polycarbosilane and tested for oxidation in steam and air. Inhibition in air by the silicon was observed, but the expected inhibition in steam was not. Clearly, further experiments are required.

### Core (WBS 1602.02)

Initiating sets of fatigue data have been taken on H451 and 2020 graphites aimed particularly at determining whether Weibull-type volume

effects persist for fatigue as well as ordinary tensile strengths. The fatigue strengths at any given stress volume were of typical form, exhibiting a linear dependence of log strength on log cycles. The specimen geometries available varied the stress volume by about a factor of 10, and over this somewhat limited range a Weibull-type decrease in fatigue strength with increasing volume was observed. Numerical analysis of the data indicate that the same Weibull statistic (i.e., the same Weibull exponent $m$) applies to fatigue as to ordinary tensile strength and that, hence, a uniform statistical treatment exists for both non-cyclic and cyclic stress.

**Technology (WBS 1602.03)**

An in-depth review of the multiaxial failure strength of graphite has been completed, and an extensive set of references to the literature has been included in this progress report. Two important conclusions have been reached as a result of this survey:

First, of the phenomenological approaches to definition of the three-dimensional failure surface, the maximum stress criterion provides an excellent fit of data in the quadrants containing tensile strengths. The added complexity of the Tsai-Wu theory is not warranted for failure in the region of practical interest.

Second, the use of fracture mechanics potentially offers a much more valid approach to defining the failure surface of interest. This approach will require continued development of analytical techniques and better definitions of the flaw field, but it offers in return a mechanistic approach and a natural introduction of the statistics into the problem.

The statistical treatment of tensile strengths for three production lots of H451 graphite has been refined, and the pertinent criteria for a self-consistent one-way variance analysis have been defined. The resulting treatment leads to a bimodal statistical model satisfying pooled variance homogeneity and passes the Kolmogorov-Smirnov goodness-of-fit tests at 95% confidence.

The treatment assumes normal or log normal distributions in order to fully utilize the inferential power of the functions related to Gaussian statistics. In view of the known Weibull characteristics of the upper strength mode, this appeal to normality is justified by the Knudsen-type dependence of strength on density. It is further proposed that a treatment of the lower mode (that due to disparate flaws) should be framed around binomial and order statistics.

## 8. MATERIALS ENGINEERING (WBS 1603)

The materials engineering activity is directed toward generation of the metallic materials data base necessary for the design and licensing of MHTGR primary system components. Additionally, efforts were initiated

during the year to develop a comprehensive Metals Technology Development Program Plan, which describes the base technology work needed to satisfy design data needs for the MHTGR.

Studies continued on the tensile, creep, and aging behavior of Hastelloy X and several other nickel-base alloys considered as alternate materials for high-temperature thermal barrier cover plates. Work on the alternate materials was completed or terminated, and most of the results have been given in a series of topical reports. Fatigue testing of Hastelloy X was terminated at the end of September. Comparison of the continuous cycle fatigue data generated in HTGR helium with those obtained in air showed that the helium environment was not detrimental to fatigue life. This was true for tests conducted at 538 through 871°C. Creep-fatigue tests conducted at 760°C showed that the introduction of a hold period at the peak tensile or compressive strain amplitude of the strain cycling waveform significantly reduced the low-cycle fatigue life of Hastelloy X. Life reduction was most pronounced at low strain ranges. A limited number of creep-fatigue tests on thermally aged Hastelloy X resulted in fatigue lives lower than those for solution-annealed material.

Creep and aging tests continued on four heats of 2.25Cr-1Mo steel with some tests having reached 75,000 h. During the year, emphasis was given to the effects of decarburization on the properties of 2.25Cr-1Mo steel. Short-term tensile and creep properties were reduced by decarburization treatments that lowered the bulk carbon content from 750 to 500 ppm and then to 170 ppm.

Fracture mechanics testing of 2.25Cr-1Mo was initiated. The program for the first year focused on defining material for preliminary tests, additional development of elevated-temperature test techniques and instrumentation, characterization of material, and performance of initial tests. Tensile and Charpy V-notch testing was completed, and some creep, creep crack growth, fatigue crack growth, and compact tension specimen testing was performed.

## 9. REACTOR VESSEL DESIGN SUPPORT (WBS 1700.11)

An assessment of the steel pressure vessel selected as the reference concept for the MHTGR was performed. Particular emphasis was given to evaluation of the metallurgical characteristics and behavior of the vessel material (ASME SA-533 grade B class 1 steel). The conclusions of the study were, in general, supportive of the steel vessel concept and the material selected.

## 10. PLANT OPERATION AND MAINTENANCE (WBS 5104.01.06)

As a member of the O&M Task Force, ORNL participated in reviewing and commenting on plant design and layout from the standpoint of operation and maintenance and in the establishment of the integrated staffing requirements for operation and maintenance. Utilizing this information, along

with cost estimating procedures developed earlier by ORNL for light-water reactor plants, ORNL developed operation and maintenance cost estimates for the 4 × 250-MW(t) side-by-side steel vessel concept, utilizing pebble bed fuel, with twin turbine generators and with a single turbine generator.

## 11. REACTOR PHYSICS AND REACTOR SHIELDING (WBS 5210.04)

The reactivity effects of water ingress into the core of a pebble-bed HTGR were calculated. Water ingress causes an increase in core reactivity by decreased core leakage, and it imposes control requirements on the HTGR. The core reactivity as a function of water ingress is also influenced by the heavy-metal loading of the reactor and tends to increase with the fuel loading. Comparisons of reactivity calculations indicated the need for experimental measurement of reactivity coefficients against which calculational results can be benchmarked. Application of depletion-perturbation theory to calculating HTGR fuel reactivity lifetimes and core power distributions was completed. Due to the negative temperature coefficient of reactivity, however, the core reactivity can be compensated by an increase in fuel temperature. Water ingress also reduces the reactivity worth of reflector control rods, which leads to the need for inner-reflector control rods in the MHTGR.

Three separate shielding studies were performed during 1985. The first two studies provided successive refinements to estimates of neutron fluences and radiation dose rates for the side-by-side steel-vessel pebble-bed-core HTGR design. Particular attention was given in the second study to the lower plenum and cross duct regions since fluence levels appeared to be excessive in those important areas. The third study, which was initiated only in the last month of the year, provided the first scoping-level analysis of fluence levels in the newly selected side-by-side steel-vessel annular prismatic-core HTGR design. In addition to the design-supporting analyses, a smaller effort was performed to couple gamma-ray cross sections to a 44-neutron-group cross-section set used in previous HTGR experiment analyses.

## 12. ADVANCED SYSTEM DESIGN SUPPORT (WBS 6600)

An assessment of HTGR advanced materials technology was initiated during the final quarter of 1985. The study addresses materials needed for service in primary coolant helium and process gases at temperatures as high as 950°C.

Studies on the creep behavior and thermal stability of a number of candidate alloys for very high temperature HTGR service continued. Materials investigated included two experimental alloys from GA Technologies, several modified versions of Inconel 617, IN-519, and Cabot alloy 214. Most of this work was completed during the year.

An ASME Task Force on Very High Temperature Design has been formed to develop design rules for alloys at temperatures in excess of those covered in ASME Code Case N-47 (i.e., >815°C). It is planned that the rules will cover metal pressure boundary components designed for 20- to 40-year service. Based on Task Force deliberations to date, significant departures from Code Case N-47 are expected.

# 1. ANNUAL PLANNING AND CONTROL (WBS 0100.02)

J. E. Jones Jr., P. R. Kasten, and
J. P. Sanders

## 1.1 INTRODUCTION

The work for the High-Temperature Gas-Cooled Reactor (HTGR) Program at Oak Ridge National Laboratory (ORNL) was performed in accordance with the national Summary Level Program Plan (SLPP) for FY 1985 as issued in September 1984 and subsequently modified under the change proposal (CP) guidelines. During 1985, input was submitted and reviews were made that resulted in the SLPP for FY 1986 (Rev. 0), which was issued in September 1985.

## 1.2 CHANGE PROPOSALS TO THE FY 1985 SLPP

For 1985, the national HTGR program was directed toward developing the 350-MW(t) modular HTGR (MHTGR), and, in January 1985, a markup of the ORNL portion of the SLPP was submitted to support this concept. Various change proposals were submitted through the year: ORNL-CP-85-4 revised the international cooperative work with Germany; ORNL-CP-85-5 revised the shielding analysis task; ORNL-CP-85-6 through 85-11 were directed toward revising and redirecting work that had previously been placed in a "hold" status; ORNL-CP-85-12 redefined work related to fuel heatup and to fission product plateout and liftoff; ORNL-CP-85-13 proposed work on advanced metallic materials; ORNL-CP-85-14 proposed work related to the evaluation of fission product behavior; ORNL-CP-85-15 proposed work concerning the evaluation of operating and maintenance costs for the side-by-side steel vessel concept; ORNL-CP-58-16 requested additional funding for the shielding work at ORNL; and ORNL-CP-85-17 pertained to the closeout of work on nickel aluminides for reformer tube application.

## 1.3 SLPP FOR FY 1986

A draft SLPP change proposal was developed concerning changes in the schedule for procuring nuclear-grade Stackpole 2020 graphite. A new schedule was proposed, and changes in associated milestones were proposed. This effort resulted in ORNL-CP-85-18, which was submitted in August.

A draft copy of the SLPP for FY 1986 was submitted in April to the Oak Ridge Operations Office (ORO) of the U.S. Department of Energy (DOE). This submission covered WBS 0 and WBS 1, which were of interest at that time. Cognizance of work in the licensing area was maintained, and several documents on planned work in the HTGR program were revised. In May, input to the other pertinent areas of the FY 1986 SLPP was prepared and submitted. Then, in June, the ORNL proposal for our effort in FY 1986 was revised in accordance with the SLPP format, and it was submitted to DOE using the budget guidance provided. Revisions to the SLPP were made on a continuing basis, and, in December, a revised SLPP budget proposal was prepared for DOE. Cognizance of the SLPP status and steps to make appropriate changes were maintained throughout the year.

## 1.4 SUBSEQUENT CHANGE PROPOSALS

In October, ORNL-CP-86-1 was submitted to provide details on the proposed shielding task for the 350-MW(t) MHTGR under WBS 5210.04. The proposed activities and milestones were based on information obtained from GA Technologies, Inc., (GA) and Bechtel National, Inc., (BNI) concerning the shielding analysis needs of this concept. The purpose of this work was to assist GA in the conceptual design of the reactor internals and BNI in the assessment of site personnel radiological doses. In response to a question from DOE, more information was subsequently prepared about the coordination of this work with GA and BNI.

In November, ORNL-CP-86-2 was prepared to formalize the schedule for preparation of the fuels and fission products technology development plan. Since the work of ORNL must follow initial tasks by GA, completion dates of the ORNL contributions were related to the receipt of the design data needs from GA.

# 2. REQUIREMENTS MANAGEMENT AND EVALUATION (WBS 0200.01)

J. E. Jones Jr., P. R. Kasten, and W. P. Barthold

## 2.1 INTRODUCTION

In this area, Oak Ridge National Laboratory (ORNL) participated in the Program Requirements Management (PRM) Task Force, which provides overall program reviews, evaluations, and recommendations to the U.S. Department of Energy (DOE) High-Temperature Gas-Cooled Reactor (HTGR) Program. During CY 1985, the major ORNL activities in the PRM Task Force were:

1. rating of different small HTGR concepts,
2. assessment of water/steam ingress on core reactivity,
3. rating of small steel vessel designs with either pebble fuel or prismatic fuel,
4. identification of key design/analysis problems for the modular HTGR (MHTGR), and
5. miscellaneous items.

## 2.2 RATING OF DIFFERENT SMALL HTGR CONCEPTS

At the beginning of CY 1985, the choices among the many HTGR concepts had been narrowed down to four, two of them being steel vessel designs and two prestressed concrete reactor vessel (PCRV) designs. The steel vessel designs used spherical fuel elements (pebble fuel), whereas the PCRV designs used prismatic fuel. The major concepts considered in this evaluation were:

1. side-by-side steel vessel design with 250-MWt modules (SBS),
2. vertical in-line steel vessel design with 250-MWt modules (ILSV),
3. cylindrical PCRV design with 1170-MWt power output (1170), and
4. annular PCRV design with 1260-MWt power output (1260).

In the side-by-side steel vessel design the core and steam generator were in separate cavities below ground level, connected by a cross duct, with the steam generator being at a lower elevation than the core vessel. The helium flowed downward in a cylindrical core.

In the vertical in-line module, the steam generator was located above the core in a cylindrical vessel. Upflow cooling was employed. The module generated 250 MWt.

The 1170-MWt design had a cylindrical core with downflow cooling, in a PCRV. This PCRV design had one dedicated natural convection loop for (upflow) passive decay heat removal.

The 1260-MWt design had an annular core with downflow cooling, in a PCRV. A passive PCRV liner cooling system was used to remove decay heat by radiation and conduction.

The major design parameters of the four concepts are compared in Table 2.1.

The four concepts were compared against a set of "MUST" and "WANT" criteria consistent with an evaluation plan that defined four major categories for the evaluation as follows:

1. function accomplishment,
2. economic characteristics,
3. compatibility with power generation needs, and
4. development needs.

For example, the category "function accomplishment" consisted of three MUST criteria and three WANT criteria with 15 subcriteria. The MUST criteria for that category follow.

1. Plants designed for equivalent availability are comparable to best U.S. light-water reactors and coal plants:
   - design equivalent availability factor at least 80% over plant lifetime;
   - plant downtime 10% per year or less.
2. Extremely low probability for events leading to equipment damage that would result in permanent loss of plant or of single reactor within a multiple-reactor plant:
   - extremely low probability means no more than $10^{-5}$ per plant year;

Table 2.1. Comparison of major conceptual design parameters for small HTGRs

| Configuration description | Side-by-side | Verticle in-line | 1260 annular | 1170 enhanced |
|---|---|---|---|---|
| Net electrical output, MWe | 377 | 379 | 520 | 430 |
| Reactors per plant | 4 | 4 | 1 | 1 |
| Nuclear steam supply system | | | | |
| Vessel type | Carbon steel | Carbon steel | PCRV[a] | PCRV[a] |
| Vessel OD × height, m | 6.04 × 22.5 | 6.34 × 39.3 | 28.8 × 32.2 | 26.5 × 28.2 |
| Steam generator vessel, m | 3.6 × 17.3 | | | |
| Fuel type/configuration | Pebble/ cylindrical | Pebble/ cylindrical | Prismatic/ annular | Prismatic/ cylindrical |
| Core flow direction | Downflow | Upflow | Downflow | Downflow |
| Number of control rods/ shutdown channels | 28/16 | 28/16 | 54 pairs/51 | 37/37 |
| Refueling method | On-line | On-line | 1/3 core replaced at 18 months | ¼ core replaced annually |
| Number of steam generators | 1 | 1 | 4 | 2 |
| Number of main circulators | 1 | 1 | 4 | 2 |
| Main circulator type/driver | Centrifugal/ electric | Axial/water turbine | Centrifugal/ electric | Centrifugal/ electric |
| Number of shutdown circulators | 1 | 1 | 2 | 2 |
| Shutdown circulator type/driver | Water turbine | Water turbine | Electric motor | Axial/electric |
| Helium pressure, MPa | 7.24 | 8.68 | 7.24 | 7.24 |
| Core inlet/outlet temperature, °C | 263/693 | 257/699 | 316/689 | 318/691 |
| Core thermal power, MWt | 250 | 250 | 1266 | 1170 |
| Core diameter/height, m | 3.00/10.79 | 3.20/9.39 | 9.4 OD × 6.1 ID/7.9 | 5.91/5.88 |
| Core power density, kW/L | 3.80 | 3.80 | 3.90 | 5.80 |
| Main circulator ΔP/power, kPa/kW | 227/4877 | 110/1991 | 143/4974 | 179/12,000 |
| Boiling direction in steam generator | Uphill | Uphill | Downhill | Uphill |
| Feedwater temperature, °C | 193 | 193 | 321 | 321 |
| Outlet steam temperature/ pressure, °C/MPa | 540/17.34 | 540/17.34 | 540/17.34 | 540/17.34 |
| Core decay heat removal modes | | | | |
| Active, pressurized or depressurized | 1 main loop, 1 aux. loop | 1 main loop, 1 aux. loop | ¼ main loops, ½ aux. loops | ½ main loops, ½ aux. loops |
| Passive, pressurized | Cavity cooling system | 1 aux. loop, ½ cavity cooling system | ½ liner cooling system | 1 nat. conv. loop |
| Passive, depressurized | Cavity cooling system | ½ cavity cooling system | ½ liner cooling system | None |

[a]Prestressed concrete reactor vessel.

- permanent loss means repair costs exceed the net present value of remaining revenue stream.

3. Public acceptance of safety characteristics:
   - plant to be licensed for commercial operation by NRC and other cognizant regulatory agencies;
   - incremental risks to public to be consistent with interim NRC goals;
   - design to preclude necessity for planned evacuation of the public outside the plant exclusion area boundary;
   - uranium enrichment up to 20%, once-through fuel cycle.

The WANT criteria for the first category, "function accomplishment," follow.

1. Maintain plant operation:
   - maximum equivalent availability;
   - minimum planned outage time;
   - operation at part load during repair or expansion;
   - ease of maintenance and maintenance access;
   - minimum requirement for in-service inspection;
   - ease of in-service inspection;
   - ease of repairing or replacing components.
2. Maintain plant protection:
   - comprehensive on-site property damage insurance available at low cost;
   - ease of maintaining plant protection, in particular, long response time;
   - minimum forced outage time.
3. Maintain control of radionuclide release:
   - low man-rem exposure;
   - resistant to sabotage;
   - margin for protection of public;
   - maximum reliance on passive features;
   - safety characteristics self-evident or readily demonstrated by analysis or testing.

Similar MUST and WANT criteria were developed for the other categories.

The ORNL evaluation of the four concepts yielded the following results:

| | Weight | SBS | ILSV | 1260 | 1170 |
|---|---|---|---|---|---|
| 1. Provide maximum degree of function accomplishment | 35 | 33.5 | 30.5 | 24.7 | 23.3 |
| 2. Provide competitive power cost | 30 | 26.6 | 25.2 | 26.75 | 25.8 |
| 3. Meet power generation needs | 15 | 14.4 | 11.6 | 13.2 | 13.1 |
| 4. Require limited development cost | 20 | 15.12 | 15.12 | 17.92 | 17.9 |
| TOTAL | 100 | 89.62 | 82.42 | 82.57 | 80.1 |

(SBS = side-by-side steel vessel design, ILSV = in-line steel vessel design, 1260 = annular PCRV design, 1170 = cylindrical PCRV design.)

The ORNL evaluation showed that none of the systems is clearly superior to the others. The SBS concept was recommended by ORNL for further conceptual design. On the basis of all recommendations from HTGR Program participants, DOE adopted the SBS concept for further development.

It should be noted that the evaluation of the different concepts was based on designs that were developed to different degrees of detail. Only limited attempts were made to optimize the designs. This lack of design detail and the inherent arbitrariness of rating systems, however, were considered in the rating interpretation. There was consensus among all HTGR Program participants that the SBS design had the greatest potential for meeting the requirements set forth in a Utility/User Requirements document.

## 2.3 ASSESSMENT OF WATER/STEAM INGRESS

A leak in the steam generator is the primary cause for water/steam entering the core of the modular HTGR. This water ingress has the following effects on performance:

1. The reactivity is increased because of a reduction in neutron leakage and a softening of the core neutron spectrum, and there is a reduction in the worth of the control rods in the reflector.
2. The possibility exists for fuel hydrolysis.
3. The possibility exists for fission product wash-off.
4. A surge in primary system pressure can accompany water ingress.

If water/steam enters the core while the reactor is operating at full power, a sudden reactivity and power increase occurs and leads to a rise in fuel temperatures. The strong negative temperature coefficient of the reactor, coupled with limiting the amount of water/steam that enters the core, keeps the fuel temperatures within acceptable limits.

If water enters the reactor while it is shut down, additional control rod worth is required to compensate for the rise in reactivity. Generally, larger amounts of water can enter the core in this condition than during full-power operation. For the pebble bed reactor design, which already had only a small margin over the required control rod worth, this requirement left little or no margin when control rods also had to compensate for the water ingress reactivity.

The discussions of water ingress phenomena in the PRM Task Group led to increased efforts by the HTGR Program to assess the impact of such accidents on performance.

## 2.4 RATING OF SMALL STEEL VESSEL DESIGNS USING EITHER PEBBLE OR PRISMATIC FUEL

As the design of the pebble bed reactor progressed, perceived limitations on reactor power level led to a reassessment of the pebble vs prismatic fuel issue.

The advantages of the two fuel types are:

| Prismatic fuel | Pebble fuel |
|---|---|
| U.S. technology | Continuous refueling |
| Potential for higher power density | Demonstrated performance in Arbeitsgemeinschaft Versuchsreaktor (AVR) and design experience from Thorium Hochtemperatur Reaktor (THTR) |
| Easier reactivity control | Flexibility in locating control rods around top of reactor vessel |
| Lower core pressure drop | High quality fuel has been tested and has exceeded predicted performance |
| Easier core restraint | Easy storage of discharged fuel |
| Proven FSV refueling technique | Easy fuel handling |
| Easy replacement of graphite reflectors | |
| Lower system pressure | |
| Upper plenum is less crowded | |

The disadvantages are:

| Prismatic fuel | Pebble fuel |
|---|---|
| High quality fuel required has not yet been fabricated | Difficult to replace buttresses and radial reflector |
| More defects due to fuel fabrication process | AVR refueling machine was not as reliable as needed in MHTGR (THTR experience might be better) |
| Refueling times could be longer than estimated | High core pressure drop |
| | Higher fuel storage volume requirements |
| | Foreign fuel technology |
| | Relatively low core power density |

Using the same ground rules as for the earlier described concept evaluation, the ORNL rating gave the following results:

| | Weight | Pebble | Prismatic |
|---|---|---|---|
| 1. Provide maximum degree of function accomplishment | 35 | 35 | 33.3 |
| 2. Provide competitive power | 30 | 26.3 | 29.8 |
| 3. Meet power generation needs | 15 | 14.6 | 15.0 |
| 4. Require limited development cost | 20 | 15.22 | 20.0 |
| TOTAL | 100 | 91.12 | 98.1 |

Based on the evaluations of all program participants, the prismatic-fueled HTGR was recommended for further development. The major advantage of the prismatic fuel is the higher power output achievable per reactor module for the conceptual designs evaluated. It should be noted that annular-type pebble-bed-reactor cores were not evaluated.

## 2.5 MHTGR SHIELDING CONSIDERATIONS

Shielding considerations are of high importance to the small steel vessel MHTGR design, and the PRM Task Force adressed them several times. Because of the requirement of shop fabrication, size limits are imposed on the reactor vessel. A high power output per module is of great importance for improved reactor economics, so space inside the vessel is limited. To

provide more space for the fuel elements (i.e., higher power), neutron and gamma shielding must be very effective and achieved in small volumes. Early analysis of the pebble bed reactor identified the following regions as requiring shielding analysis: the cross duct, core support plate, side of the reactor vessel, and top of the reactor vessel. Such shielding analyses provide input to the design of the lower and upper vessel internals, the design of the vessel system, the development of in-service inspection and maintenance techniques, and the overall assessments of radiological personnel dose. Overall, the PRM Task Force identified shielding analyses as an important part of the conceptual design of the MHTGR.

## 2.6 IDENTIFICATION OF KEY DESIGN/ANALYSIS AREAS FOR THE MHTGR

As part of the PRM Task Force activities, participants identified areas where further key design/analysis/technology efforts were required. ORNL identified the following major areas where additional work appears needed:

1. fission product liftoff,
2. fuel element and core performance,
3. internals design and shielding,
4. reactor physics measurements, and
5. reactor layout.

The economic attractiveness of the MHTGR depends to a great extent on the passive safety characteristics that are achievable. These passive safety features permit many plant components and systems to be non-safety grade, and they eliminate items such as a containment building. At the same time, key technology development is needed to validate that the superior fuel performance and the retention of fission will take place as expected. In particular, fission product "liftoff" under depressurization accidents must be at a low level; to validate that behavior, experimental studies that give pertinent data and understanding to fission-product liftoff phenomena are necessary. Further, the retention of fission products within fuel coatings must be demonstrated experimentally under fuel heatup conditions to validate the expected superior fuel performance characteristics under postulated accident conditions.

Because of their importance to the conceptual design of the reactor vessel internals, more detailed shielding analyses are required for both the lower and upper internals. In collaboration with GA Technologies, Inc., Bechtel National, Inc., and Combustion Engineering, ORNL developed a shielding analysis program for the MHTGR.

With regard to reactor physics calculations for MHTGRs using low-enriched uranium fuel, there appears to be a need to benchmark such calculations against experimental criticality measurements.

Relative to the general reactor system layout, design improvements still appear possible. For example, use of coolant upflow in the MHTGR appears to provide a number of advantages over the present downflow. Advantages would be associated with decreasing the depth of the reactor silo, reducing the risk of hydraulic flow fluctuations in the reactor core, and providing natural circulation cooling of the core under various conditions. These improvements would be facilitated by placing the control rod drives below the core, moving the steam generator vessel upward relative to the reactor vessel location, and placing the shutdown heat-exchanger system at the top of the steam generator vessel. While there are no present plans to make such changes in the MHTGR plant layout, future optimizations in plant design may be possible.

# 3. LICENSING SUPPORT (WBS 0300.01)

P. R. Kasten and W. P. Barthold

## 3.1 INTRODUCTION

The major activities in licensing support during CY 1985 were focused on the following areas:

1. Licensing Plan,
2. Top Level Regulatory Criteria,
3. Outline of a Preliminary Safety Information Document (PSID),
4. Development of Principal Design Criteria (PDC), and
5. NRC briefings.

Oak Ridge National Laboratory (ORNL) participated in program meetings concerning the above areas and reviewed and commented on pertinent documents provided by other program participants.

## 3.2 LICENSING PLAN

On April 26, 1985, the U.S. Department of Energy (DOE) submitted a document entitled "Licensing Plan for the Standard HTGR" (HTGR-85-001) to the U.S. Nuclear Regulatory Commission (NRC) for review and concurrence. This licensing plan outlined the long-range objectives of the High-Temperature Gas-Cooled Reactor (HTGR) Program and steps to be taken to develop a commercially viable HTGR. The Licensing Plan proposed a series of detailed interactions between DOE HTGR Program participants and NRC as a basis for obtaining licensing guidance on the modular HTGR (MHTGR). The long-range objective is to submit an application for a standard plant review and, upon NRC approval of the standard plant design, to file for certification of the design via the rulemaking process. Current NRC policy and regulations indicate that this can be done before construction or operation of any demonstration or commercial unit.

The short-term objective of the MHTGR Program, as stated in the Licensing Plan, is to carry out a series of meetings with NRC staff over the next two years that will facilitate MHTGR licensing. These meetings are to include information on the MHTGR design and the supporting base technology program.

### 3.3 TOP LEVEL REGULATORY CRITERIA

A document entitled "Top Level Regulatory Criteria for the Standard HTGR" (HTGR-82-002) was prepared within the MHTGR Program and submitted by DOE to NRC for concurrence with respect to the completeness and acceptability of these criteria for the MHTGR Program. The top level criteria are defined as standards for judging the licensability of the HTGR, and they directly specify what are believed to be acceptable limits for protection of public health and safety and the environment. The top level criteria consider normal operation and a broad spectrum of anticipated events, including accidents. Criteria on occupational exposure were not included in the top level criteria.

The selection bases for the criteria were:

1. Criteria should represent direct statements of acceptable consequences or risks to the public or the environment.
2. Criteria should be quantifiable.
3. Criteria should not discriminate between current generations of reactors and the MHTGR.

Based on the above selection bases, the following regulatory sources were identified as containing top level criteria:

1. NUREG-0880, "Safety Goals for Nuclear Power Plant Operation";
2. 10CFR20, "Permissible Dose Levels and Activity Concentrations in Unrestricted Areas";
3. 10CFR50, Appendix I, "Numerical Dose Guidelines for Meeting the Criterion 'As Low as Is Reasonably Achievable' for Power Reactor Effluents";
4. 10CFR100, "Numerical Dose Guidelines for Determining the Exclusion Area Boundary, Low Population Zone, and Population Center Distance"; and

5. EPA-520/1-75-001, "Protection Action Guide Doses for Protective Actions for Nuclear Incidents."

These sources also contain some of the guidelines for implementation of top level criteria and therefore go beyond a statement of goals. For the MHTGR top level criteria, only the numerical consequences or risk values contained in these sources are candidates for top level criteria.

### 3.4 PSID OUTLINE FOR THE MODULAR HTGR

On October 7, 1985, a report entitled "PSID Outline for the Standard HTGR" (HTGR-85-063, July 1985) was transmitted from DOE to NRC for concurrence. This report presents an outline of the PSID for the MHTGR, which is scheduled to be submitted to NRC by September 1986. The PSID will describe the conceptual design of the Standard MHTGR Nuclear Island, and its interface with the balance of plant and a standard site. The reactor plant is divided into the Nuclear Island systems and the Power Generation systems. The description of the Power Generation systems will be limited to a functional description and identification of interfaces with the Nuclear Island, and an evaluation of those interfaces that are relevant to a radionuclide control function.

In addition, the PSID will identify the radionuclide control criteria and requirements to be applied to the design. It will present the analysis of the system performance and response to Design Basis Events to demonstrate that the criteria and requirements are met.

The PSID outline has been reviewed by NRC, and comments by NRC are being evaluated by the program participants.

### 3.5 PRINCIPAL DESIGN CRITERIA

By means of an integrated approach, user requirements and top level regulatory criteria provide guidance to the development of the reactor design. The integrated approach develops functional requirements and selections for the design. Systems, structures, and components (SSCs) are classified either as safety related or not safety related. Safety-related SSCs are selected by using results of probabilistic risk analyses (PRA) of the MHTGR. Based on their calculated frequencies for occurrence and consequences, some of the accident sequences identified in the PRA are

designated as licensing basis events (LBEs). The calculated consequences of those events are compared with dose criteria derived from 10CFR100. By using the functional analysis approach, those functions that have to be performed will be identified and specified such that the consequences of LBEs do not violate the dose criteria. Those functions are designated as safety-related functions. The SSCs that perform the above functions will then be identified, and those SSCs are called safety related. The Principal Design Criteria (PDCs) are related to performing the safety-related functions. They require design commitments that will ensure that the reactor plant will meet the dose criteria for LBEs.

The submittal of those PDCs from DOE to NRC for the standard HTGR is scheduled for CY 1986 together with submittals on licensing basis events and equipment classifications.

By using the functional analysis tree related to Goal 3, "Maintain Control of Radionuclide Releases," the retention of radionuclides in fuel particles has been identified as the only function necessary to comply with dose criteria derived from 10CFR100. This means that the MHTGR does not rely on additional retention of radionuclides in a containment, the core vessel, or even the graphite in the core in order to meet 10CFR100. As a result, the MHTGR needs only a few PDCs. At this time, four PDCs have been identified. The first one deals with the design, fabrication, and operation of the fuel; the second deals with core design and performance parameters to ensure passive core decay heat removal without having the fuel reach excessive temperatures; the third deals with the control of chemical attacks by limiting air ingress to the primary system; the fourth PDC will deal with the control of heat generation, but it has not yet been developed.

### 3.6 NRC BRIEFINGS

Meetings with NRC staff were arranged by DOE throughout the year. Those attended by ORNL personnel were held on July 31, August 1, and December 18, 1985; they covered the integrated approach, plant design, and MHTGR design update, respectively.

## 4. PROGRAM MANAGEMENT (WBS 1000.01)

J. E. Jones Jr. and P. R. Kasten

Included in this work area are overall activities required to manage the Oak Ridge National Laboratory (ORNL) high-temperature gas-cooled reactor (HTGR) development program. This involves management of the technology development programs, coordination of efforts between ORNL and other HTGR program participants, overall planning and scheduling of work, and general review of the overall national program to assist in the planning of ORNL efforts. In particular, management of technology program planning and integration is emphasized along with technical review of HTGR program reports. A number of other items are included in this activity, such as the development of the Summary Level Program Plans for the ORNL portion of the national program and the issuance of monthly, annual, and milestone reports for ORNL activities. During the last year a number of miscellaneous activities were also performed, such as coordination of an International Atomic Energy Agency Specialists' Meeting at ORNL (in May) on gas-cooled reactor safety and accident analysis, preparing a paper on U.S. HTGR technology development [which was presented at the Technische Vereinigung, Der Grosskraftwerksbetreiber E.V., Essen VGB International Conference on HTGRs held in the Federal Republic of Germany (FRG) in September], maintaining the Tower Shielding Facility at ORNL to ensure its availability for possible use in future shielding experiments, reviewing HTGR program efforts with foreign visitors, and participating in U.S. Department of Energy discussions concerning possible cooperative programs in HTGR technology development with the FRG and Japan.

# 5. INTERNATIONAL TECHNOLOGY TRANSFER (WBS 1400.01)

P. L. Rittenhouse and J. C. Cleveland

## 5.1 AVR/KFA/ORNL COOPERATION ON HTR PHYSICS, PERFORMANCE, AND SAFETY – J. C. Cleveland and D. R. Vondy

This effort involves cooperation between Arbeitsgemeinschaft Versuchs Reaktor GmbH (AVR), Kernforschungsanlage Jülich GmbH (KFA), and Oak Ridge National Laboratory (ORNL) in the physics, performance, and safety of high-temperature reactors (HTRs). This cooperation has been established and is being performed within the frame of the HTR Implementing Agreement between the U.S. Department of Energy (DOE) and the Federal Republich of Germany (FRG) Ministry for Research and Technology (BMFT). The objectives are to further the understanding of HTR performance and safety and to compare predictions of reactor behavior with experimental data. This cooperative program involves reactor physics, dynamics, and safety evaluations of small pebble bed reactors. Inherent safety and self-stabilizing features are being investigated through analysis of reactor experiments performed at the AVR. The program includes benchmarking computational methods and exchange of ideas on improvements in reactor analysis techniques, on simulation of accidental reactor behavior of modular HTRs, and on design approaches for modular systems.

### 5.1.1 Analyses of AVR Dynamic Experiments – J. C. Cleveland

The dynamic experiments that have been analyzed by ORNL are part of a series of tests performed at the AVR during 1982 and 1983 to examine the change in reactor performance as the core composition was changed from highly enriched uranium with thorium to a mixed core of low-enriched uranium and highly enriched uranium with thorium. The experiments are of two types:

1. experiments involving changes in reactivity by control rod motion with the reactor remaining at power, and

2. experiments involving changes in the speed of the circulators (and therefore the helium flow through the core) allowing the reactor to achieve a new power level without control rod motion. (Some of these tests included shutdown of the reactor by stopping the circulators.)

The analyses of these experiments provide the opportunity to

1. investigate important core characteristics that influence the reactor response, that contribute to its high degree of safety, and that provide it with self-stabilizing features, and
2. examine the modeling complexity necessary to predict the reactor response to "at-power" transients involving flow changes and/or small, slow reactivity insertions.

Because of the similarities between the AVR and modular HTRs, results of this investigation can provide useful insights relative to the level of detail required in models for modular HTRs for use in an overall plant dynamics code. Access to data from AVR performance and safety tests provides the opportunity to benchmark reactor analysis techniques and tools against actual conditions. Results reported here illustrate that simple modeling techniques can provide accurate predictions of the reactor power response for "at-power" transients involving changes in core flow and/or slow reactivity changes.

The following AVR experiments have been analyzed:

1. Flow reduction test (April 16, 1982). With the reactor initially at full power conditions, the test was initiated by reducing the speed of both circulators to 50% over 68 s, and the power was allowed to stabilize at a new level. Then both circulators were stopped. During the test there was no control rod motion.
2. Control rod withdrawal test (August 5, 1982). With the reactor initially at 82% power, the test was initiated by inserting +10.6 cents reactivity over 25.6 s through control rod motion. The reactor was then allowed to stabilize at a new power level.
3. Flow increase test (August 3, 1982). With the reactor initially at 50% power conditions, the test was initiated by increasing the speed of both circulators by 72% in 67 s (resulting in an increase in core reactivity and thermal power due to increased core cooling). The power was allowed to stabilize without control rod motion.

4. Control rod insertion test (August 2, 1982). With the reactor initially at 98% power, the test was initiated by insertion of −10.6 cents of reactivity over 5.2 s through control rod motion. The reactor was then allowed to stabilize at a new power level.

The experimental data are reported in refs. 1 and 2. These experiments illustrate the inherent stabilizing features of the HTR. Factors contributing to this response are the low power density, the high thermal capacity of the core, and the strongly negative temperature coefficient of reactivity.

The ORNL core dynamics model used for these analyses of the AVR was formulated from existing techniques developed and used at ORNL during the past 11 years for high-temperature gas-cooled reactor (HTGR) analyses, with the appropriate changes for pebble fueling. The general modeling features employed are:

1. Point (space independent) neutron kinetics representation with six groups of delayed neutron precursors.
2. A coarse-structure thermal model with heat conduction dynamics and heat convection in each axial section approximated by a model of the "average pebble" in that section.
3. Nuclear importance (flux squared) weighting of solid temperatures in the axial direction to determine the effective temperature-to-reactivity feedback to the neutron kinetics model.
4. Computation of reactivity effects due to changing $^{135}Xe$ concentration using coupled, first order, time dependent equations for the core average $^{135}I$ and $^{135}Xe$ concentrations based on the core average flux.
5. A quasi-static, one-dimensional representation of the helium temperature and flow.
6. For forced convection conditions, helium flow is computed from measured circulator speed, core inlet temperature, and pressure assuming volumetric flow is proportional to circulator speed. For natural convection conditions, helium flow is computed by balancing unrecoverable losses through the primary loop against the density difference driving head.
7. Computation of the total power including decay power as the output of a series of optimized lead-lag filters with prompt power (as

determined by the point kinetics equations) as an input and with filter coefficients and time constants selected to match afterheat generation following a step decrease influx to zero.

### 5.1.2 Analysis of Flow Reduction Test

Figures 5.1 and 5.2 show computed results and the measured flux for the flow reduction test performed on April 16, 1982. The reactor was initially at full power with a core inlet gas temperature of 271°C and a gas outlet temperature of 807°C. The test was initiated by reducing the speed of each circulator from 4000 rpm to 2000 rpm over 68 s. The speed was then held constant at 2000 rpm until shutdown of both circulators was initiated at 1085 s. During the test there was no control rod motion. When the circulator speed was reduced, the negative temperature coefficient ($-5.9 \times 10^{-5}$/°C) and the increasing fuel temperature caused the power to closely follow the flow reduction as shown in Fig. 5.1. The large heat capacity prevented excessive increases in fuel temperature. With the decrease in flux, the $^{135}$Xe burnout rate decreased resulting in a transient increase in $^{135}$Xe concentration and a negative reactivity contribution as shown in Fig. 5.2. About 300 s after initiation of the reduction in speed of the circulators, the core reactivity returned to zero with the negative contribution due to the increasing $^{135}$Xe concentration being balanced by a positive fuel temperature contribution resulting from the operation at the reduced power and flow.*

With shutdown of the circulators (initiated at 1085 s) the fuel experienced a slight heatup (note in Fig. 5.2 the dip in the reactivity contribution due to the fuel temperature increase) driving the reactor subcritical. The rate of increase in $^{135}$Xe concentration increased when the reactor went subcritical (due to the decrease in $^{135}$Xe burnout rate),

---

*At 1085 s, when the circulator shutdown was initiated, the computed $^{135}$Xe reactivity change (relative to time zero) due to the increasing $^{135}$Xe concentration was about 17 cents. If this transient had occurred in the hypothetical case before $^{135}$Xe had been built into the core, the nuclear average fuel temperature during the transient would have been higher than for the case with the $^{135}$Xe present in order to maintain reactivity at zero (i.e., to contribute a negative reactivity contribution equal to that otherwise held by the $^{135}$Xe). For example, at 1085 s, the nuclear average fuel temperature would be ~16°C higher if the flow reduction transient had been initiated without $^{135}$Xe present.

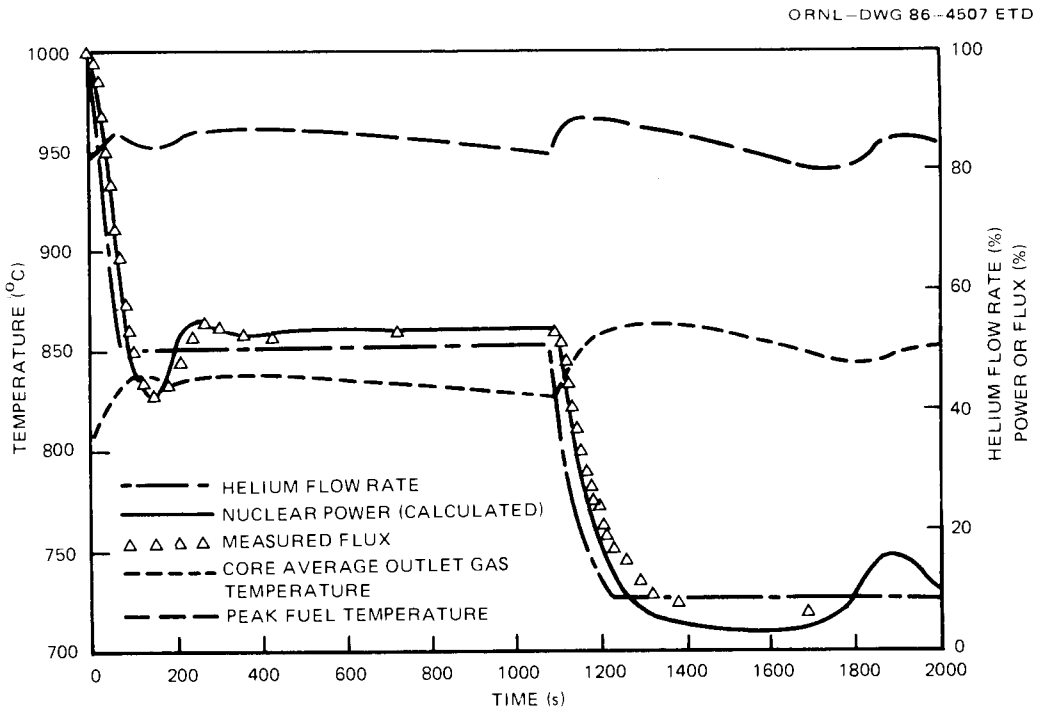


Fig. 5.1. Response of AVR to flow reduction test on April 16, 1982.

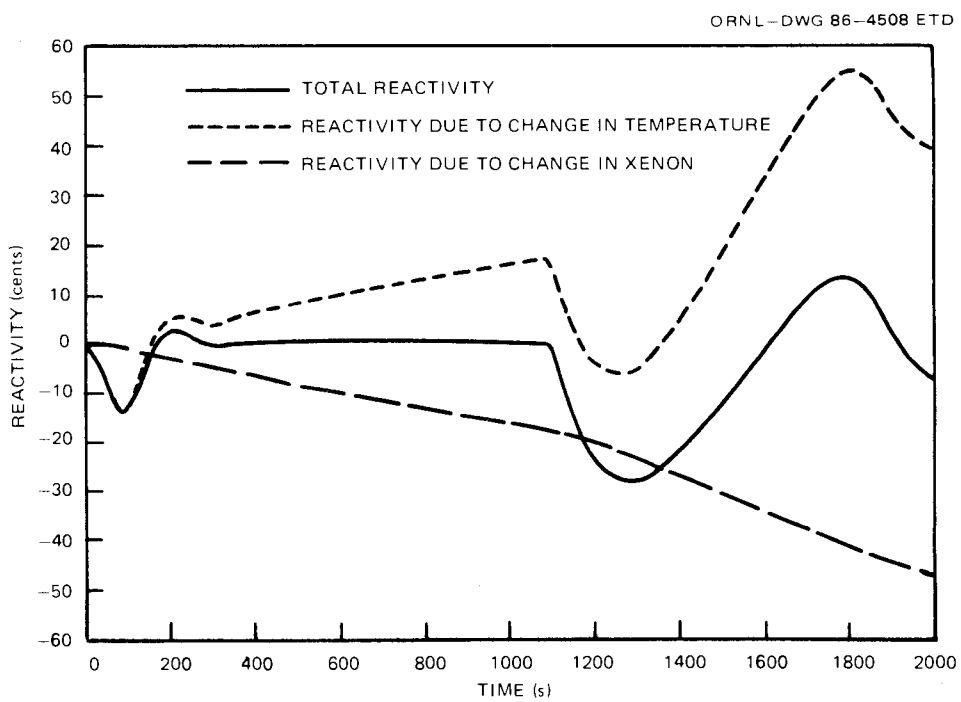


Fig. 5.2. Reactivity in AVR during AVR flow reduction test of April 16, 1982.

and the resultant additional contribution of negative reactivity was sufficient to hold the reactor subcritical to about 1600 s even with cooling of the fuel by natural convection (which the model estimates to be about 8.5% of full flow). (Note: this recriticality could have been delayed by several hours by closing the main circuit valves, as has been done in AVR tests described in ref. 3, thereby blocking natural convection gas flow through the main loop.) The prediction of nuclear power during the transient compares well with the measured flux.

Summarizing the flow reduction test, the influence of core characteristics on reactor response is:

1. The negative temperature coefficient causes the power to closely follow the rate of heat removal from the core.
2. As the reactor power (neutron flux) changes, the resulting change in $^{135}Xe$ reactivity is an important component in the overall reactivity balance.
3. With a large reduction in core flow (e.g., by 50%) and with no control rod motion, the high heat capacity of the fuel and the negative temperature coefficient combine to produce only moderate changes (on the order of 30°C) in maximum fuel temperature.
4. The reactor can be driven subcritical by stopping the circulators. The natural convection through the main gas flow loop limits the increase in fuel temperature.

Note from Fig. 5.2 that the reactivity change and rate of change are quite slow for this transient, and, as Fig. 5.1 illustrates, the power transient is predicted very well with the point kinetics model.

### 5.1.3 Analysis of Control Rod Withdrawal Test

Figures 5.3 and 5.4 show computed results and measured flux for the control rod withdrawal test performed on August 5, 1982. The reactor was initially at 82% power with a core inlet temperature of 255°C and a core outlet temperature of 845°C. The test was initiated by inserting +10.6 cents of reactivity in 25.6 s (a reactivity insertion rate of about 0.4 cents per s) by control rod motion. Because the final power level is not very different from the initial level, changes in $^{135}Xe$ concentration

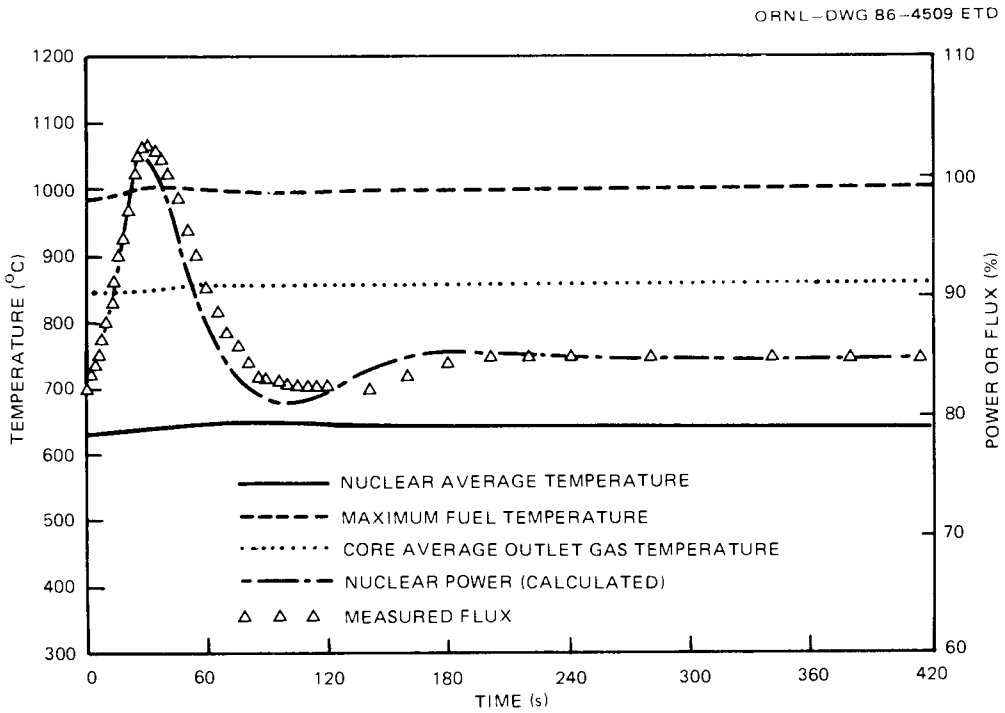


Fig. 5.3. Response of AVR to control rod withdrawal transient of August 5, 1982.

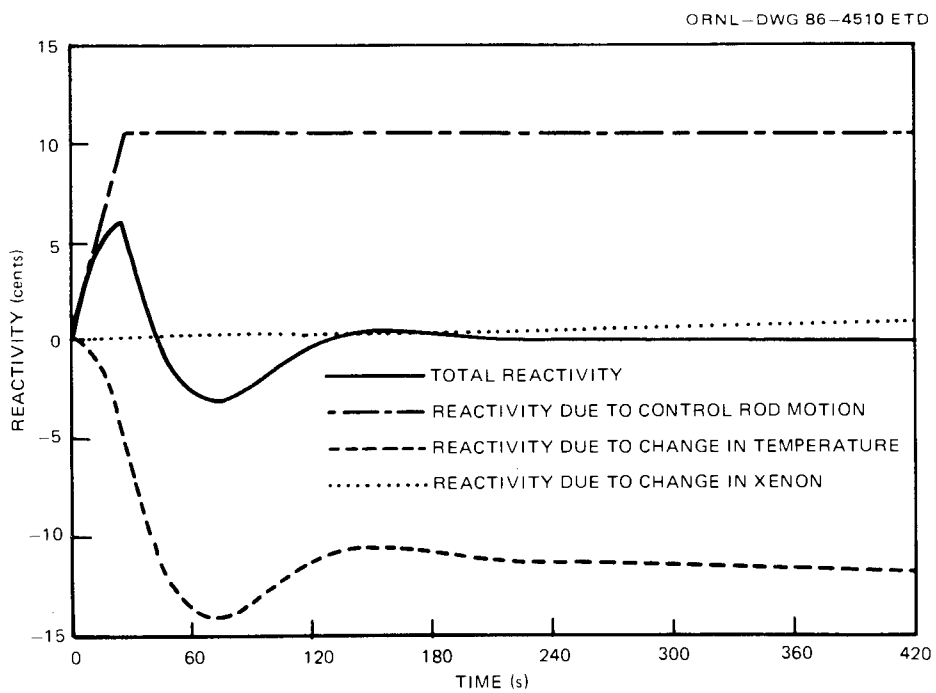


Fig. 5.4. Reactivity in AVR during control rod withdrawal transient of August 5, 1982.

are not large and have only a small influence on the transient. The increase in reactivity due to the control rod movement causes the power to increase until the fuel temperature adjusts to counter this increase in reactivity. As Fig. 5.3 indicates, the power transient is predicted very well with the point kinetics model.

The validity of a point kinetics model for gas-cooled reactor simulation has also been investigated in ref. 4. The conclusion is that point kinetics are valid for slow reactivity changes (insertions of up to \$2.0 at less than 2 cents/s) such as those resulting from slow movement of control rods. However, according to ref. 4, for transients involving large reactivity insertions and insertion rates (such as rod ejection, which can introduce \$2.0 in 0.1 s), the point kinetics model is not accurate and does not necessarily give conservative results.

### 5.1.4 Analysis of Flow Increase Test

Figures 5.5 and 5.6 show computed results and measured power for a flow increase test performed on August 3, 1982. The reactor was initially at 50% power with a core inlet temperature of 253°C and a core outlet temperature of 802°C. The speed of each circulator was then increased from 1900 rpm to 3262 rpm over 67 s without motion of the control rods. The increased core flow resulted in increased core cooling, which caused a fuel temperature decrease and an associated positive reactivity insertion. The power therefore increased until the fuel temperature returned to slightly above its initial level, with the remainder of the reactivity balance resulting from the temporarily reduced $^{135}$Xe concentration that occurred because of the increased $^{135}$Xe burnout rate at the higher flux level.

### 5.1.5 Analysis of Rod Insertion Test

Figures 5.7 and 5.8 show computed results and measured power for a control rod insertion test performed on August 2, 1982. The reactor was initially at 98% power with a core inlet temperature of 269°C and a core outlet temperature of 828°C. A reactivity change of −10.6 cents was introduced in 5.2 s via control rod motion. Again, the power adjusts until the reactivity introduced by changes in fuel temperature and $^{135}$Xe concentration counter the reactivity introduced by the rod motion.

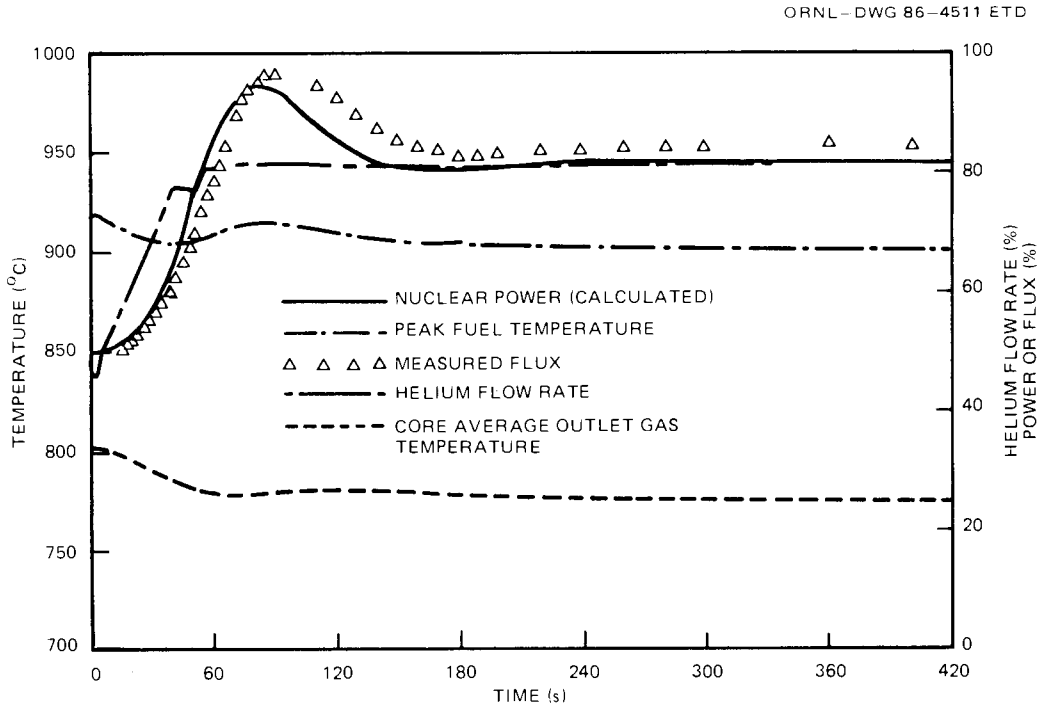


Fig. 5.5. Response of AVR to flow increase of August 3, 1982.

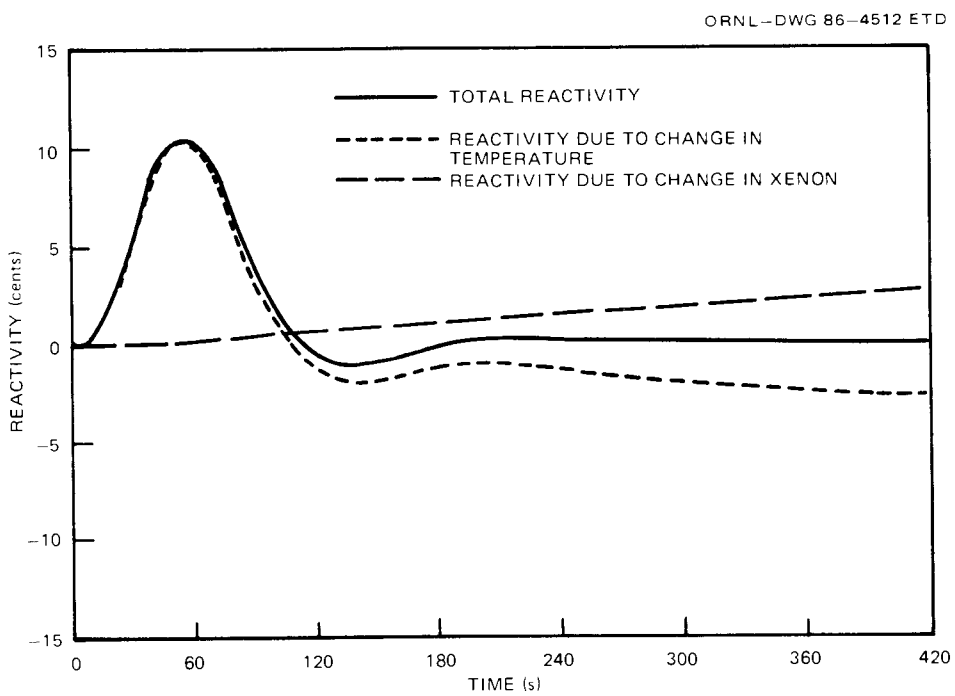


Fig. 5.6. Reactivity in AVR during flow increase test of August 3, 1982.

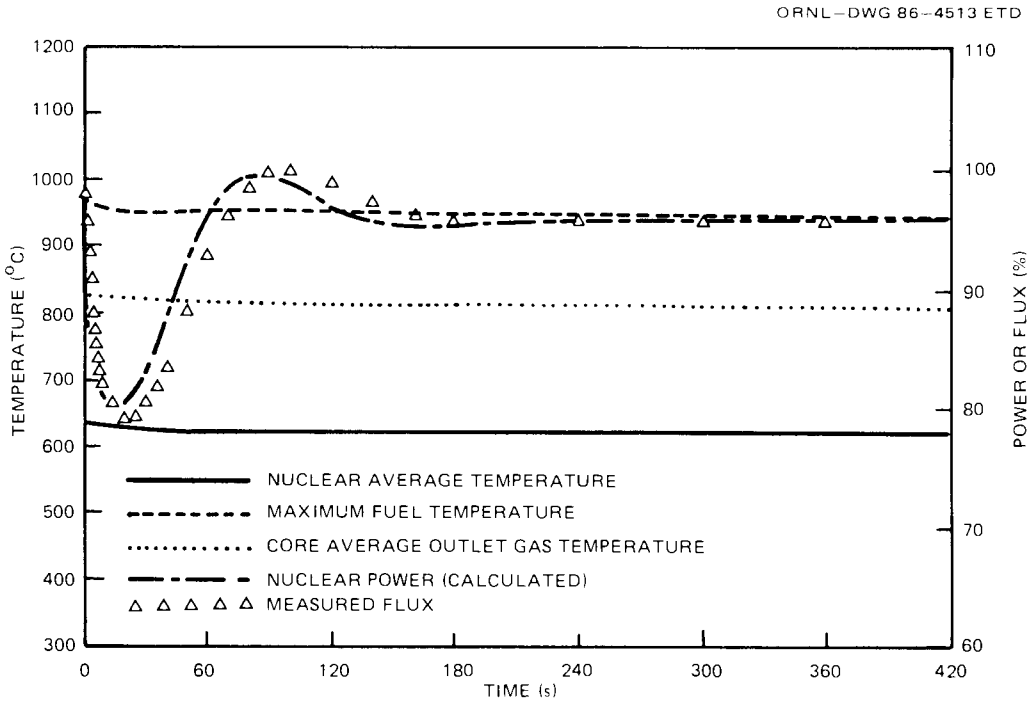


Fig. 5.7. Response of AVR to control rod insertion transient of August 2, 1982.

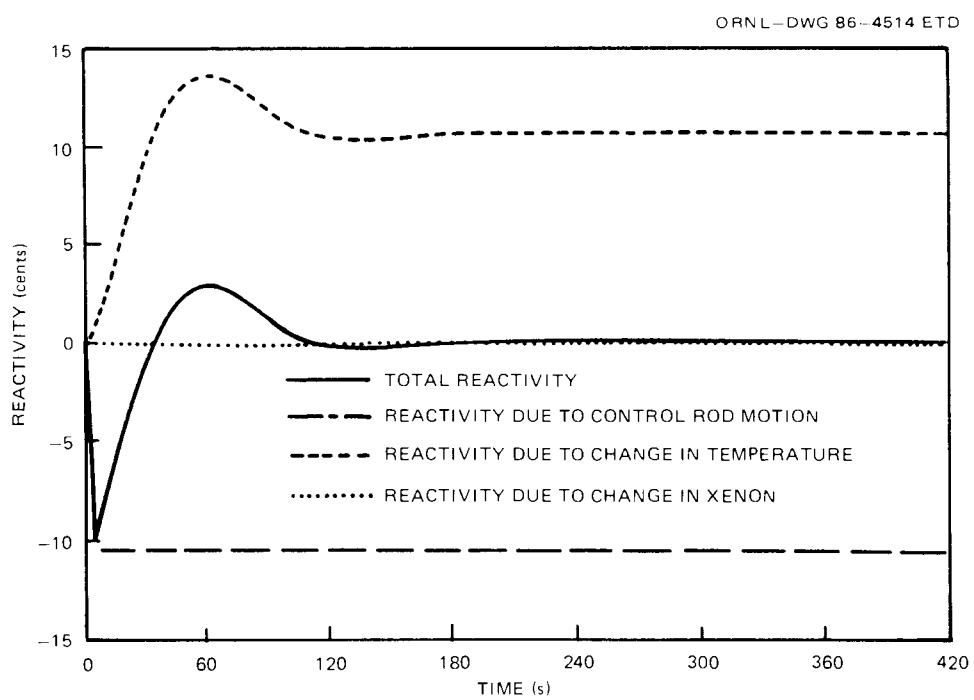


Fig. 5.8. Reactivity in AVR during control rod insertion transient of August 2, 1982.

Analyses at ORNL of the above experiments indicate that core response during "at-power" transients involving changes in core flow and/or small and slow reactivity insertions can be modeled with fairly simple dynamic analysis methods. Because of similarities between the AVR and modular HTRs, this suggests that similar methods can be used to model modular size cores for use in an overall plant dynamics code for investigating plant response to "at-power" transients. Also, the reactor response during the experiments illustrates important self-stabilizing features of HTRs.

### 5.1.6 Neutronic Analyses of the AVR – D. R. Vondy

Calculations were done for an AVR pebble fuel element to compare core physics results over a range in temperature with ENDF/B cross sections, versions -IV and -V. Of special interest are the temperature coefficients of reactivity. These results were reported to the FRG.[5] It was found that for a highly enriched uranium system with thorium, the latest data were slightly more reactive and the negative temperature coefficient of reactivity was a bit larger in magnitude. The latest graphite and thorium data were processed with improved procedures into a fine-group library, 227 groups plus resonance data for version V. The available data libraries were collapsed into few-group libraries, 28 groups for version V, facilitating data testing. Microscopic cross sections were generated with the resonances shielded in a four-group structure to generate data for review at KFA.

Continuing effort went into calculations for the AVR using the core contents described by KFA. These results and the results obtained by applying local methods to predict the core contents are being reported.[6] Nuclide reaction rates were obtained and core thermal hydraulics problems were solved for highly enriched uranium fuel with thorium. These results showed very little difference in multiplication for the core with ENDF/B version -IV and -V data, while the latest data produce negative temperature coefficients somewhat similar in magnitude. Different models of the core produced rather different fuel temperature distributions.

Primary results were obtained with an (RZ) diffusion theory model of the reactor. Four-group cross sections were generated by collapse of data for a few-group (R) traverse with discrete ordinates. Results obtained for the reactivity temperature coefficient $T\partial k/k\partial T$ are shown here:

| Cross section nuclide concentrations temperature (°K) | ENDF/B-IV KFA Model | ENDF/B-IV Calculated | ENDF/B-V KFA Model | ENDF/B-V Calculated |
|---|---|---|---|---|
| 600 | −0.0689 | −0.0720 | −0.0626 | −0.0623 |
| 1000 | −0.0844 | −0.0878 | −0.0680 | −0.0663 |
| 1600 | −0.1182 | −0.1295 | −0.0983 | −0.0990 |

Coupled neutronics and thermal hydraulics capability was used to estimate the power level reactivity coefficient. Values of $P\partial k/k\partial T$ were generated for a 20% increase in power:

| Coolant flow | ENDF/B-IV | ENDF/B-V |
|---|---|---|
| Fixed | −0.0389 | −0.0316 |
| Increased | −0.00207 | −0.00185 |

where stable conditions were assumed (not short-time response), and the increased coolant flow rate state affects the removal of heat at the reference 265°C outlet temperatures, and therefore this models a smaller temperature rise than with a fixed flow rate. This coefficient is 15% smaller in magnitude with the new data.

Calculations are planned next year to predict control rod insertion reactivity worth and to study reaction rates in fuel elements for low-enrichment uranium fuel without thorium.

## 5.2 COOPERATION ON HTGR BASE TECHNOLOGY – P. L. Rittenhouse

### 5.2.1 Cooperation on Fuels – M. J. Kania

Set 3 irradiated fuels from three German experiments, BR-2-P23, -P24, and -P25, are awaiting irradiated microsphere gamma analyzer (IMGA) examination in the High Radiation Level Examination Laboratory (HRLEL) at ORNL. Each of the three experiments contained a different candidate fuel type: BR2-P23 contained Triso-coated $UC_2$; BR2-P24 contained HTI Biso-coated $(Th,U)O_2$; and BR2-P25 contained Triso-coated $(Th,U)O_2$. Approximately 2000 unbonded particles were obtained from each of these experiments by a chemical deconsolidation performed at Kernforschungsanlage (KFA) Jülich. The unbonded particles were received at ORNL in August 1983. They have been held in HRLEL storage since that time.

The unbonded particles have undergone detailed visual examination in the IMGA cubicle. Examinations initially scheduled for August 1985 have been rescheduled for March 1986. These fuels will be the first to be examined in the IMGA facility since its upgrade was completed in June 1985.

### 5.2.2 Petten Tensile Creep Results on H451 Graphite – C. R. Kennedy

As part of the Umbrella Agreement, grade H451 graphite specimens are tensile creep-tested with the Federal Republic of Germany (FRG) grades at Petten. The results of these creep tests are compared with the ORNL compression creep tests in Fig. 5.9. Since the creep strain is inversely proportional to stress, it is convenient to compare data creep-tested under different stress levels using creep strain/stress as the ordinate. This permits a direct comparison of data, and it is immediately obvious that the data are not in good agreement. The tensile creep-rate coefficient is less than that obtained from the compression creep tests. This type of behavior is not expected and suggests that possible experimental errors may be the cause.

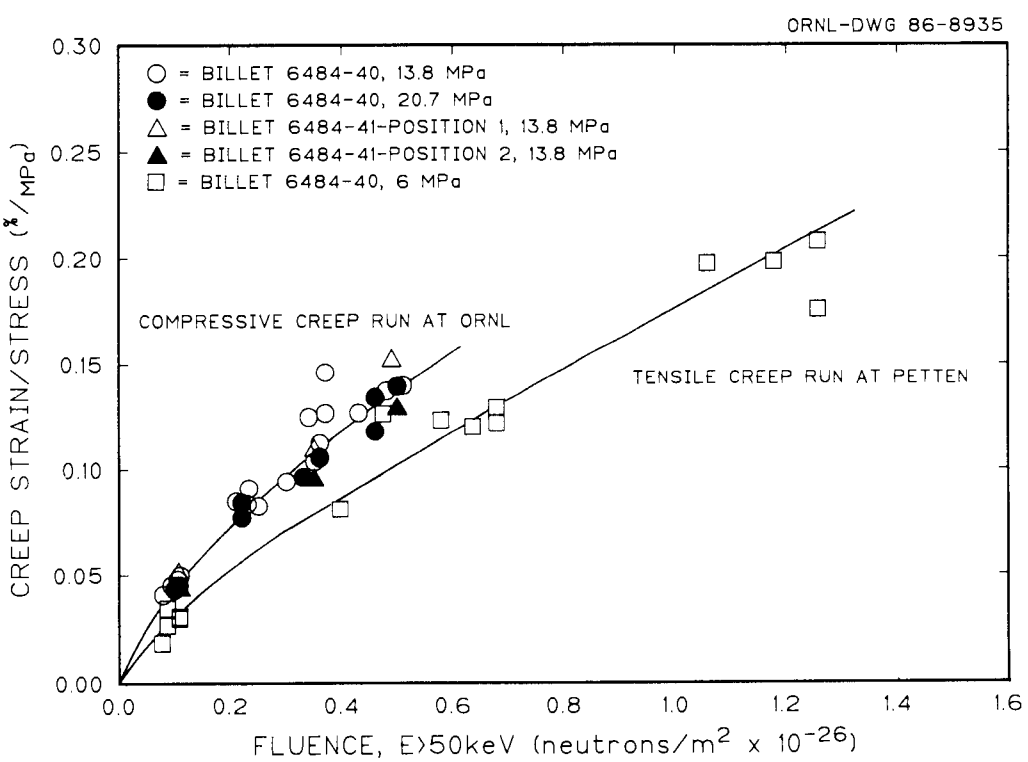


Fig. 5.9. Comparison of tensile and compressive creep results on H451 graphite.

This possibility was examined by comparing the dimensional changes of the control specimens from both Petten and ORNL creep experiments along with other irradiation test results run in the High Flux Isotope Reactor (HFIR). The results of this comparison are given in Figs. 5.10 and 5.11 for the growth in the with-grain and against-grain directions. In both figures the Petten results demonstrate similar initial growth rates; however, the growth rate then accelerates, and it appears that the volume reversal is occurring at a much lower fluence. The initial agreement in the dimensional changes suggests that the dosimetry is in agreement. The general characteristics of these data suggest that the Petten experiments were run at a higher temperature than the ORNL experiments. This, however, is in conflict with the lower creep-rate results, which suggest that the Petten experiments were possibly run at a lower temperature. There is not an obvious resolution of this conflict in results. The Petten results with increased growth rates and reduced creep rates can more than double calculated stresses within the large graphite blocks.

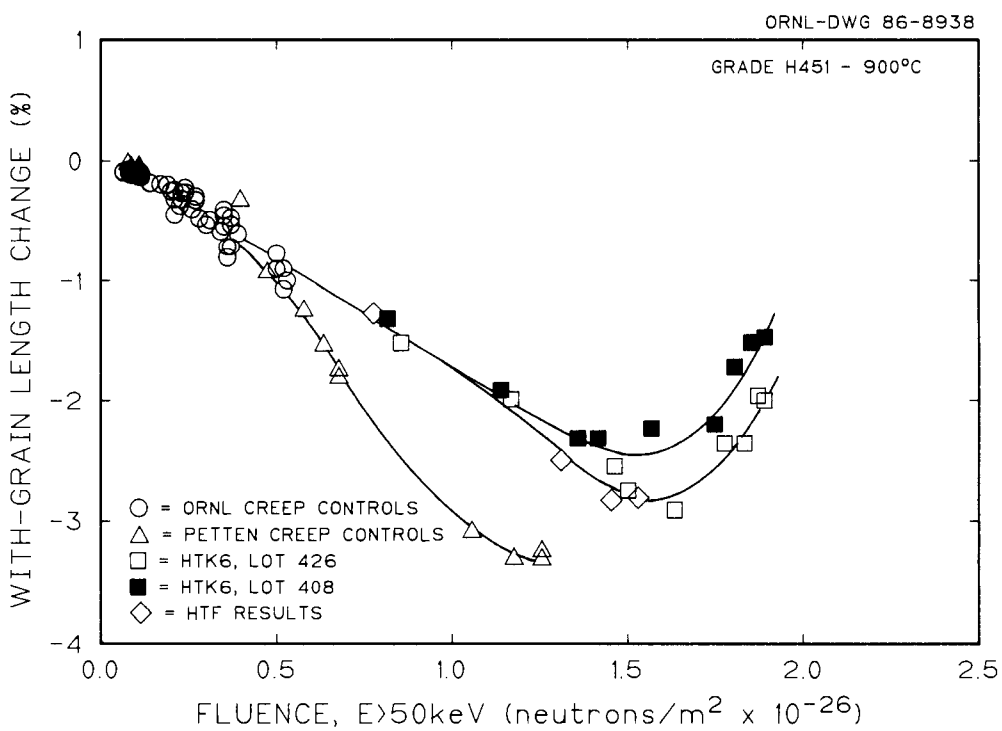


Fig. 5.10. With-grain dimensional changes of H451 graphite as a function of neutron fluence.

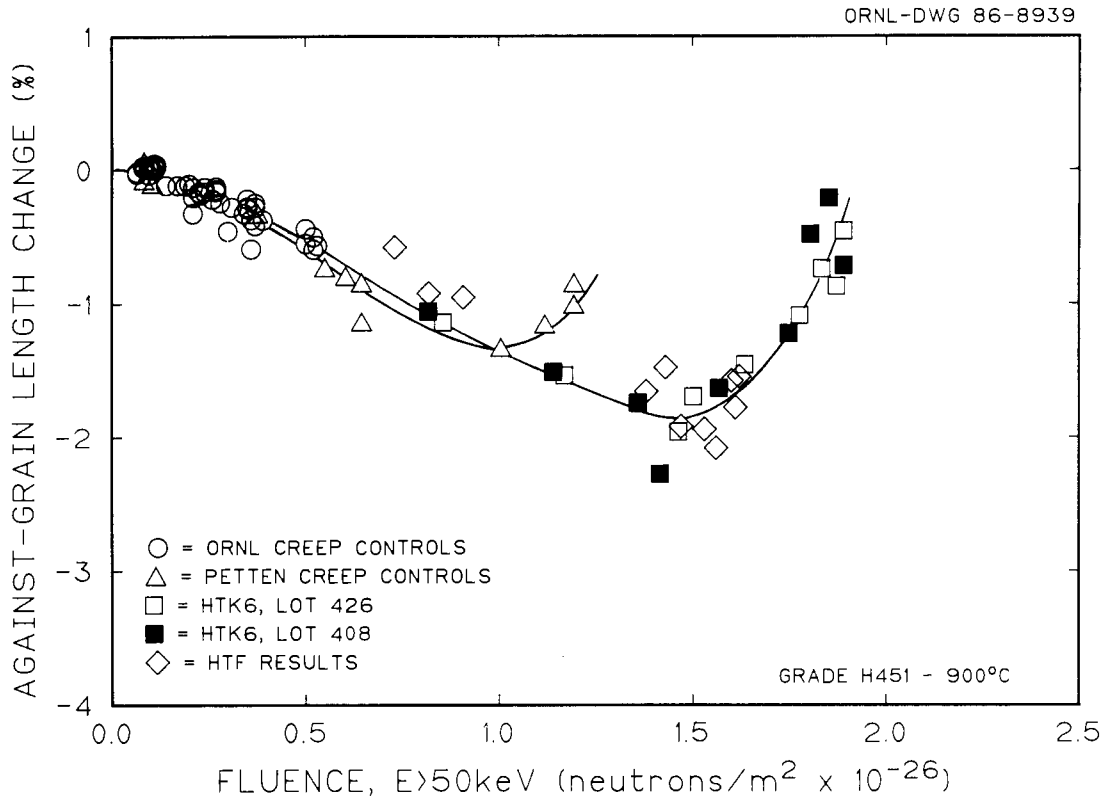


Fig. 5.11. Against-grain dimensional changes of H451 graphite as a function of neutron fluence.

### 5.2.3 Cooperation on Materials – P. L. Rittenhouse and J. P. Strizak

#### 5.2.3.1 US/FRG/CH Materials Subprogram

Cooperative work and technology transfer on HTGR materials are being carried out under international agreements involving the United States, the FRG, and Switzerland. Details of the cooperation are described in the Materials Subprogram Plan updated annually by the Subprogram managers. During 1985, cooperation involved over a dozen task areas covering various aspects of surface phenomena, mechanical properties, and structural design methods. Work on three tasks (Project Work Statements) was completed during the year.

In November 1985, the Subprogram Managers met at KFA Jülich in the FRG to review progress of the cooperative work, plan and coordinate new efforts, and update the Subprogram Plan. Major activities to be carried out in 1986 were agreed on, and the updated and revised Plan was issued in December for review by all participants.

### 5.2.3.2 ORNL PWS Activities

Oak Ridge National Laboratory is participating in round-robin testing programs on low-cycle fatigue (PWS M-1) and fracture mechanics [J-integral testing (PWS M-5)]. A number of factors (experimental variables) are important in obtaining and evaluating fatigue and fracture mechanics data. These factors include specimen design, mode of test control, strain and load measurement techniques, environment, strain rate, and wave form. The common objective of the subject round-robins is to compare and assess experimental equipment and test methods being employed in the United States, the FRG, and Switzerland in order to recommend test practices, improve data confidence, and provide a basis for possible future cooperation in high-temperature-fatigue and fracture-mechanics programs. GA Technologies (GA), General Electric Company (GE), and ORNL are joined in these tasks by Gesselschaft für Hochtemperatur-Technik MGH/Interatom GmbA (GHTIA), Brown, Boveri, & Cie Aktiengesellscraft (BBC), and KFA in the FRG and by Eidenoessiches Institut für Reaktor forschung (EIR) in Switzerland.

The participants have conducted a series of fully reversed, strain-controlled low-cycle fatigue tests on a single heat of solution-annealed Alloy 800H hot-rolled bar stock provided by KFA. Testing at three strain ranges (0.3, 0.6, and 1.0%) was done at 850°C in air employing a triangular waveform with a strain rate of $4 \times 10^{-3}$/s. The individual laboratories conducted triplicate tests at each strain range. The data were sent to KFA, and all participants have received a detailed compilation (>600 pages) of stress-strain curves, stress versus cycle curves, test techniques, etc. The round-robin program shows that the mean values of peak stress and of specimen life obtained by the individual laboratories differ by more than a factor of seven at the lowest strain range (0.3%), while the scatter of the data originating from one laboratory was typically in the range of a factor of two. A report giving possible reasons for the differences in results is to be prepared by KFA for discussion with all the participants. It is hoped that a joint final report on the round-robin will be available by August 1986.

J-integral tests on Alloy 800H material (30-mm-thick plate) provided by KFA have been conducted by GA, GE, and ORNL. Each laboratory conducted two room-temperature tests employing 25.4-mm-thick compact tension (CT)

specimens, and ORNL conducted an additional test with a 12.7-mm-thick specimen. Both GA and ORNL used the partial unloading compliance method to determine crack extension, while GE employed a displacement based key-curve method developed at GE. The agreement in $J_{Ic}$ values obtained at GA and ORNL was very good even for the two specimen sizes; the $J_{Ic}$ values ranged from 1014 to 1157 $kJ/m^2$. The $J_{Ic}$ values obtained at GE using the key-curve method were somewhat higher (1182 and 1340 $kJ/m^2$).

Determination of $J_{Ic}$, though, is largely dependent on the accuracy of crack extension measurement. The specimen sizes used were inadequate to measure the high toughness of the Alloy 800H material; an estimated 100-mm-thick specimen would be required for valid $J_{Ic}$ determination according to ASTM Standard E813.

The $J_{Ic}$ data generated at GA, GE, and ORNL have been exchanged with EIR, the lead organization. The tests at EIR were conducted on three-point bend specimens using an electric potential drop method for measuring crack extension. As with the CT specimens used by GA, GE, and ORNL, the three-point bend specimens did not meet the E813 size criteria. Nonconformance with the E813 size criteria was recognized prior to testing but was not expected to preclude an informative round-robin. It was encouraging to note that application of the ASTM data analysis procedure to several of the EIR tests produced good agreement, considering the specimen geometry difference and inadequate size for valid toughness determination.

Test data from KFA, GHTIA, and BBC will be sent to EIR by March 1986. A detailed compilation of the round-robin test data will be provided to each participant. An evaluation report is scheduled for June 1986.

## 5.3 REFERENCES

1. P. Pohl, "Zusammenstellung der Messdaten zum dynamischen Experiment beim Abfahren des Reaktors am 16.4.1982," AVR Aktennotiz, June 21, 1982.

2. P. Pohl, "Zusammenstellung der Messdaten zu der dynamischer Experimenten vom 2. bis 5.8.82," AVR Aktennotiz, Oct. 20, 1982.

3. G. Ivens and K. Krüger, "Safety-Related Experiences with the AVR-Reactor," presented to IAEA Specialists' Meeting on Safety and Accident Analysis for Gas-Cooled Reactors, Oak Ridge, Tennessee, May 13-15, 1985.

4. R. Brogli and R. Froehlich, "Space and Spectrum Effects for Rod Removal Transients in an HTGR," *Trans. Am. Nucl. Soc.* **13**, (June–July 1970).

5. D. R. Vondy, "Cross Section Data Evaluation in Application to the German AVR," attachment to letter J. C. Cleveland, Oak Ridge National Laboratory, to K. Krüger and E. Teuchert, Kernforschungsanlage Jülich, May 1985.

6. D. R. Vondy, "Application of ENDF Data to the AVR Reactor with Highly Enriched Uranium Fuel and Thorium Feed," in process.

# 6. FUELS AND FISSION PRODUCT BEHAVIOR (WBS 1601)

M. J. Kania

## 6.1 INTRODUCTION

The Modular High-Temperature Gas-Cooled Reactor (MHTGR) Fuel Materials Program and the Fission Product Performance Verification Program at Oak Ridge National Laboratory (ORNL) continue as part of a national fuel and fission product development effort in cooperation with GA Technologies (GA).

### 6.1.1 Fuel Materials Qualification Program – M. J. Kania

The Fuel Materials Qualification Program is conducted in close cooperation with GA. The ORNL portion is directed toward irradiation planning and testing of GA-fabricated fuel in test capsules designed and assembled at ORNL and operated in ORNL reactors. ORNL is also responsible for extensive postirradiation examinations (PIE) on the irradiated fuel in special examination facilities developed and maintained specifically for this purpose. The GA responsibilities include interface with core designers and inclusion of data derived from the irradiation tests into fuel performance models; GA also has the responsibility for fuel manufacturing, process development, and quality control.

In addition to the cooperation with GA, the ORNL fuels program includes specific cooperative tasks with the German Nuclear Research Center at Jülich [Kernforschungsanlage (KFA) Jülich]. This cooperation with KFA is part of the formal agreement between the U.S. and Federal Republic of Germany (FRG) governments for high-temperature reactor development. Only one active area of cooperation in the fuel development remains between ORNL and KFA. The work conducted in this area for this report period is reported in Chapter 5, Section 5.2.

## 6.2 IRRADIATION CAPSULE ASSEMBLY AND OPERATION

### 6.2.1 Capsules HRB-17 and -18 – M. J. Kania and R. L. Senn

Capsules HRB-17 and -18 represent an experiment designed to evaluate the in-reactor performance of failed UCO fuel particles when subjected to moisture levels simulating various water ingress accidents.[1] In the presence of moisture, it is known that fissile kernel material will undergo hydrolysis depending on the amount of moisture available. In a reactor environment, hydrolysis results in a substantial increase in the fission gas release fraction from the exposed kernel. This experiment, and a much larger follow-up experiment HFR-B1 (ref. 2), will provide definitive data on which to base a fission gas release model for hydrolyzed fuel.

Progress during 1985 included completion of the installation and checkout of the capsule control and monitoring instrumentation at the High Flux Isotope Reactor (HFIR) site. This instrumentation includes (1) the moisture injection, control, and monitoring equipment; (2) the gas chromatograph, hydrogen detector, and accompanying Spectra Physics integrating system; (3) the fission gas sampling system; and (4) an integrated computer system and software for automated fuel temperature and capsule pressure monitoring and alarms. The capsules were inserted into the Removable Beryllium Reflector and the irradiation initiated on August 17, 1985.

#### 6.2.1.1 Capsule Fabrication and Assembly

The fabrication and assembly of capsules HRB-17 and -18 were completed in June 1984 and had been held in storage until their use was required. Both capsules contained the nearly identical test specimens, which included (1) six fuel rods, each containing approximately 3% designed-to-fail UCO particles intermixed with normal TRISO-coated particles in bonded fuel rods; (2) unbonded particles in a sealed Incoloy-clad container; (3) a graphite diffusion sample experiment in a sealed niobium-clad container; and (4) piggy-back samples of encapsulated UCO particles and short silver dosimeter wires.

#### 6.2.1.2 Irradiation in HFIR

In August 1985, capsule HRB-17 was installed in position RB-5 and capsule HRB-18 in position RB-7. On August 17, 1986, the irradiation began

and both capsules were brought to their normal operating temperature of 800°C. A summary of the operating history through December 1985 is shown in Table 6.1. At the end of the fifth HFIR irradiation cycle, 273, the fuel had been exposed to nearly 2443 h of full reactor power at 100 MW(t). This represents a total of 101.8 effective full power days of HFIR operation.

Table 6.1. Irradiation history for capsules HRB-17 and -18 through December 1985

| HFIR cycle | Start | | End | | Irradiation times[a] | |
|---|---|---|---|---|---|---|
| | | | | | Cycle | Cumulative |
| 269 | 0900 | 8/17/85 | 2350 | 9/03/85 | 422.8 | 422.8 |
| 270 | 0406 | 9/05/85 | 0400 | 9/26/85 | 503.9 | 926.7 |
| 271 | 2100 | 9/30/85 | 0209 | 10/22/85 | 508.9 | 1435.6 |
| 272 | 2338 | 10/23/85 | 0140 | 11/14/85 | 506.0 | 1941.6 |
| 273 | 1154 | 11/24/85 | 0908 | 12/17/85 | 501.2 | 2442.9 |
| 274 | (Both capsules out of the reactor during this cycle) | | | | | |

[a]Time at full reactor power of 100 MW(t).

### 6.2.1.3 Capsule Operation

Capsules HRB-17 and -18 were operated at the same temperature, as near as possible, for the first five irradiation cycles. Figure 6.1 shows the operating temperature history for capsule HRB-17 for this period. A similar operating temperature history for HRB-18 is shown in Fig. 6.2. The operating temperature histories are displayed as a function of time from beginning of irradiation, and the three plots in each figure represent the maximum fuel, mean fuel, and minimum fuel temperatures. The data shown were obtained from thermocouples placed along the centerline of the six fuel rods in each capsule.

In October 1985, ORNL and GA agreed that the initially planned eight-cycle irradiation for capsules HRB-17 and -18 should be shortened to six HFIR cycles. This decision was based on the full life exposure requirements for the MHTGR system, which was more closely represented by a

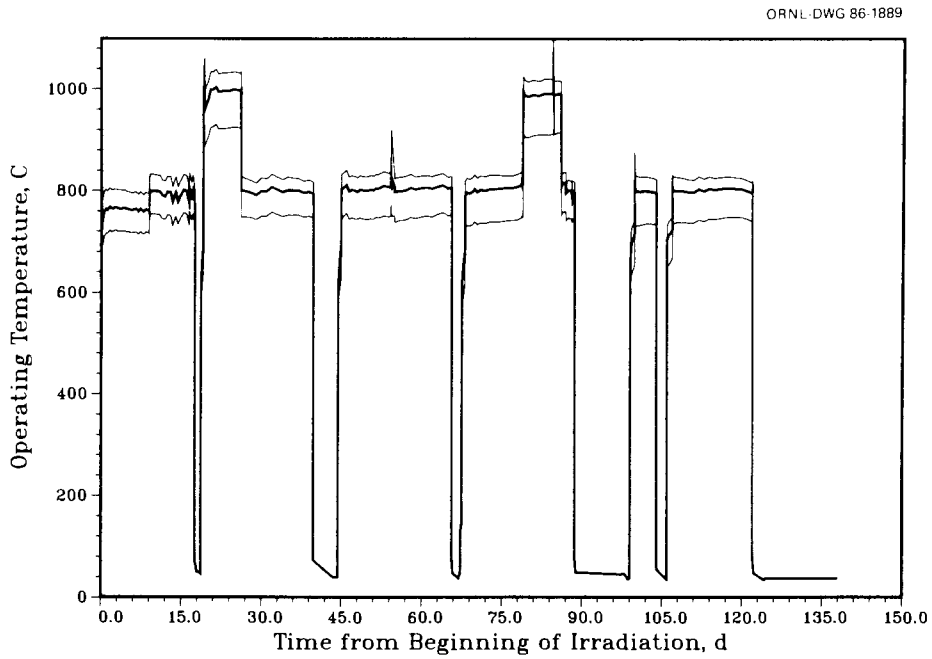


Fig. 6.1. Operating temperature history for fuel rods under irradiation in capsule HRB-17. The curves represent, from top, the maximum fuel, mean fuel, and minimum fuel temperatures derived from thermocouples located along centerline of fuel rods.

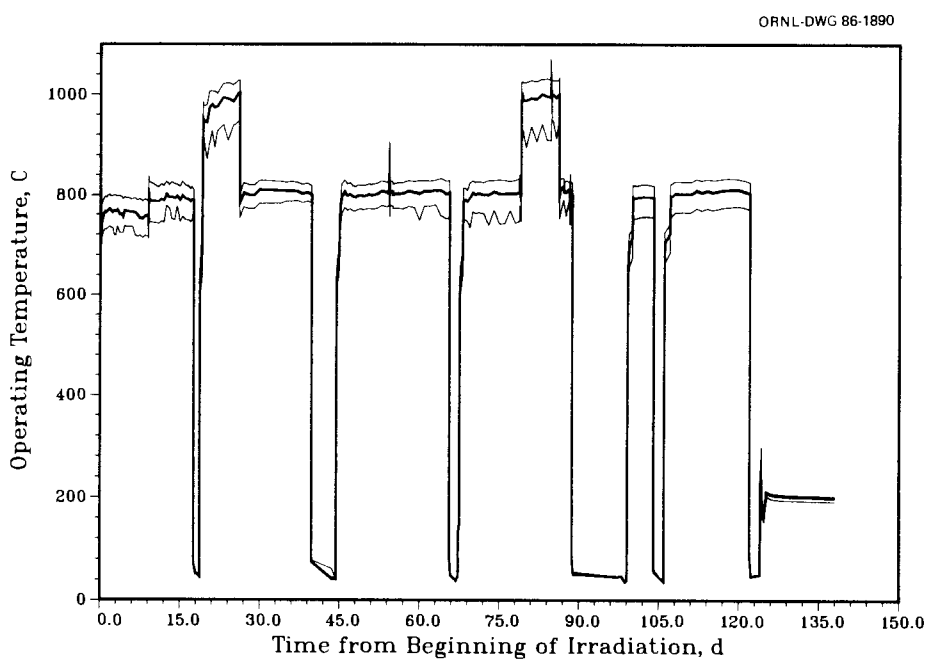


Fig. 6.2. Operating temperature history for fuel rods under irradiation in capsule HRB-18. The curves represent, from top, the maximum fuel, mean fuel, and minimum fuel temperatures derived from thermocouples located along centerline of fuel rods.

six-cycle irradiation. When these capsules were initially planned, the reference HTGR was the 2200-MW(t) unit, and to achieve full-life exposure in HFIR required eight full cycles.

During the first five irradiation cycles, four moisture injections were carried out in capsule HRB-17. In cycle 270, a single moisture injection at 100 ppm was introduced into the capsule. During cycle 271, two moisture injections occurred; the first was at 100 ppm and lasted for about 7 days, and the second was at 100 ppm and lasted for about 13 days. In cycle 273, a fourth moisture injection at 1000 ppm occurred for about six days. The effects of the moisture injections on fission gas release-rate to birth-rate ratios (R/B) are shown in Fig. 6.3. The data shown are for the isotope Kr-85m and in general are representative for the other short-lived radioactive fission gases. In the case of the second 100-ppm moisture injection, no R/B samples were taken. However, the activities of a number of samples were measured, and they exhibited a twofold increase over the measuring period.

As a comparison with the HRB-17 fission gas release data are the HRB-18 R/B data, Fig. 6.4, where no moisture was injected. Both capsules contained the same number of designed-to-fail particles and experienced the same operating temperature and neutron environment. The effects of the moisture in capsule HRB-17 are dramatic. At the end of the fifth irradiation cycle, the R/B in capsule HRB-18 was about three times lower than in capsule HRB-17, $3.2 \times 10^{-4}$ compared with $1.3 \times 10^{-4}$. During the two periods when the 1000-ppm moisture occurred, the HRB-18 R/B values were 20 to 25 times lower than those for HRB-17, $1.2 \times 10^{-4}$ compared with about $2.3 \times 10^{-3}$. Until the first 1000-ppm moisture injection, the R/B for the two capsules were at the same level of about 8 to $9 \times 10^{-5}$.

At the end of the fifth HFIR irradiation cycle, 273, both capsules were removed from their in-core position and placed in the reactor pool. Just prior to the reactor shutdown, a 10,000-ppm moisture injection was introduced into capsule HRB-18. This large amount of moisture was used to simulate a large water ingress during a reactor shutdown. Capsule HRB-18 was placed in an in-pool furnace, out of the reactor, and will be operated at 200°C during the down cycle 274. Capsule HRB-17 will remain in the pool and will be maintained at the pool temperature, 55°C.

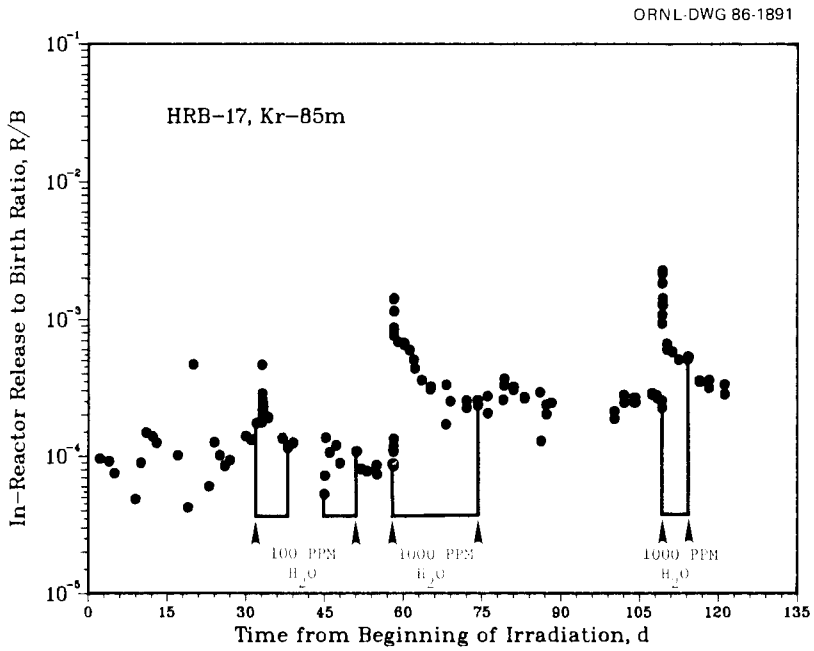


Fig. 6.3 Fission gas release-rate to birth-rate ratio (R/B) for the isotope Kr-85m in capsule HRB-17 as a function of accumulated time in reactor. The data shown represent R/B sampling for the first five HFIR irradiation cycles.

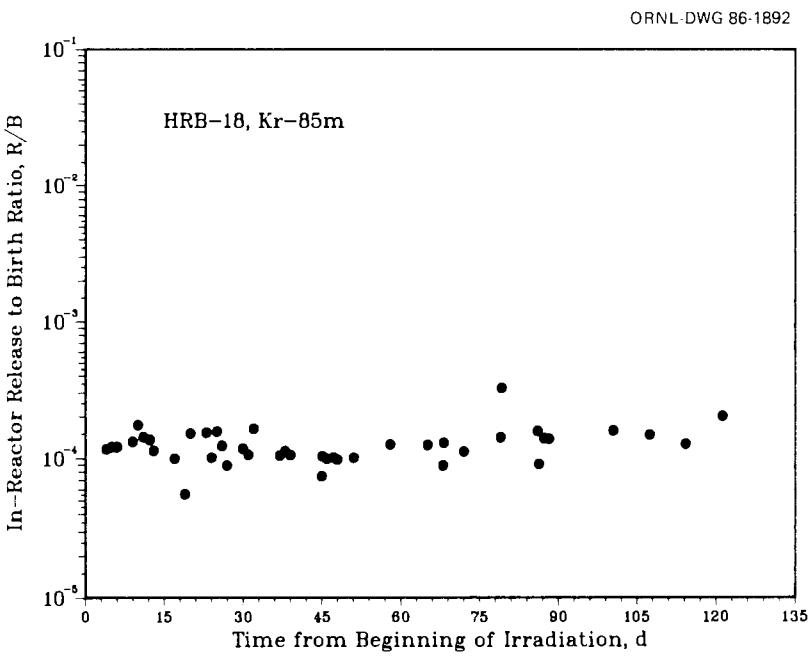


Fig. 6.4 Fission gas release-rate to birth-rate ratio (R/B) for the isotope Kr-85m in capsule HRB-18 as a function of accumulated time in reactor. The data shown represent R/B sampling for the first five HFIR irradiation cycles.

At the end of this report period, about 170 fission gas R/B samples from HRB-17 and about 70 R/B samples from HRB-18 were analyzed. Each sample was analyzed for the radioactive krypton isotopes KR-85m, Kr-87, and Kr-88 and for the zenon isotopes Xe-133, Xe-135, and Xe-138. GA and ORNL worked closely to monitor and evaluate the data from capsules HRB-17 and -18. As planned, one additional irradiation cycle will occur at the end of cycle 274. Both capsules will be reinstalled in the reactor and the irradiation continued.

Completion of the capsule irradiations is expected in early February 1986. At that time, the two capsules will be removed from the HFIR, allowed to cool in the pool-side facility for a period of two weeks, and then sent to the High Radiation Level Examination Laboratory (HRLEL) where the postirradiation examination will be carried out.

## 6.3 POSTIRRADIATION EXAMINATION OF IRRADIATION EXPERIMENTS

Postirradiation examinations conducted during this report period were in support of the evaluation of GA-fabricated fuels irradiated in capsules HRB-16 and R2-K13. A final report prepared for each of these experiments by GA included portions prepared by ORNL in regard to the PIE results and analysis conducted here. A summary of the conclusions reached in experiment HRB-16 is provided in Section 6.3.1, and similarly for experiment R2-K13 in Section 6.3.2. At the end of this report period, only German irradiated fuels for set 3 under the U.S./FRG cooperative agreement remained in PIE at the HRLEL.

### 6.3.1 Experiment HRB-16 – M. J. Kania

Irradiation experiment HRB-16 successfully irradiated several low-enriched fissile and fertile particle fuel types to peak burnups of 29% FIMA fissile burnup and 6% FIMA fertile burnup and accumulated neutron fluences of $6.3 \times 10^{25}$ neutrons/m$^2$ (E > 29 fJ) HTGR. Time-averaged operating temperatures were less than 1100°C. Details of the irradiation, operating conditions, postirradiation examinations, and analyses are presented in ref. 3. Specific conclusions derived from the postirradiation examinations are provided below.

1. Kernel migration up to 65 μm was observed in $UO_2$ TRISO particles in metallographic studies of HRB-16 fuel rods. The kernel migration coefficient back-calculated from the measured kernel displacements was within the 95% confidence bound on the design curve for $UO_2$. By contrast, no migration at all was seen in ZrC-gettered $UO_2^*$ TRISO particles, in some cases in the same fuel rods which had ungettered $UO_2$ TRISO particles which did migrate.

2. The performance of the $UO_2^*$ TRISO particles irradiated at the peak exposure conditions in HRB-16 was excellent. A comparison with the other low-enriched uranium (LEU) fuel types also irradiated in HRB-16 showed the $UO_2^*$ performance superior in terms of kernel stability, fission product retention, and low failure fractions.

3. The SiC coatings on the UCO TRISO particles in HRB-16 showed severe fission product attack to the point of failure in some cases. This degradation of the barrier coatings on these particles also resulted in a high failure fraction (3.5% at 95% confidence based on cesium release) and widely varying fission product retention. It is believed that the poor performance of these UCO batches was primarily coating-related and may in some cases be due to effects of the accelerated irradiation.

4. Postirradiation gas analyzer (PGA) results on HRB-16 fuels showed that failure fraction determinations based on gaseous fission product retention can vary significantly from those based on retention of metallics. In particular, particles irradiated without OPyC layers apparently retained a high percentage of their krypton and zenon inventories while losing a large percentage of cesium. This probably indicates significant holdup of fission gases within the particle, say by intact IPyC layers or by the kernel itself.

5. The HRB-16 fuel rods were in excellent condition following irradiation. Their integrity was good with little or no debonding, cracking, or chipping. Irradiation-induced dimensional changes of these fuel rods were in good agreement with Fuel Design Data Manual predictions at fast fluences less than $4.5 \times 10^{25}$ n/m$^2$ but were in fair to poor agreement with predictions above this fluence level, shrinking less than predicted on the average.

6. Failures of OPyC coatings at the several percent level were seen in the TRISO-coated HRB-16 particles. This observation is consistent with other recent capsule data showing OPyC failure levels in the 0% to 10% range in TRISO particles of 750 to 900 μm total diameter.

7. Pressure vessel failures in highly faceted and high defective fraction SiC particles were less than 5% compared with preirradiation predictions of 5% to 20% failure. This finding, along with other irradiation test evidence, has led to a recent revision to a higher assumed SiC strength in the current fuel particle performance models.

8. A test of the effect of matrix impregnation in the OPyC layers of TRISO-coated fuel particles proved inconclusive as a result of particle spillage in the one unbonded particle sample containing these particles.

9. As a result of a reduced workscope in the HRB-16 postirradiation examination, two unbonded particle samples (Trays 6 and 27) with ZrC-TRISO coatings were not examined in any but a visual manner.

10. The calculated and measured fission product inventories for the encapsulated piggyback samples were shown to be in agreement except for discrepancies that apparently could be removed by careful selection of cross sections as indicated by the analysis of the inventory data.

11. In general, the release of fission product metals from fuel kernels was greatest for Cs, intermediate for Ag, and smaller for Ce, Eu, Sb, Ru, and Zr. The high release of Eu from $UC_2$ and of Ag from $ThO_2$ were prominent exceptions.

12. A strong dependence of fission product metal release on burnup was confirmed for Cs release from oxide kernels. At the same burnup, the diffusion of Cs in $ThO_2$ was more rapid than in $UO_2$, due presumably to uranate formation of Cs in the latter fuel.

13. The release of fission product metals from fuel kernels was larger at larger neutron flux or fluence. This effect on release decreased as the carbon content of the fuel decreased.

14. The release of Cs and Ag was smaller in hydrolyzed, annealed, and irradiated fuel kernels than in corresponding unhydrolyzed kernels of $UC_2$ or UCO. In $UO_2$ kernels, the release was slightly greater in the hydrolyzed fuel.

15. The release of fission product metals and of Kr-85 in particles with exposed buffer layers was proportional to the extent of further densification during irradiation.

16. The release of fission product metals in particles with exposed inner pyrocarbon layers was small but proportional to the penetration depth of the hole that exposed the layer. No Kr-85 was released from particles with exposed, intact, inner pyrocarbon layers.

### 6.3.2 Experiment R2-K13 – M. J. Kania

This irradiation experiment was a cooperative effort between GA and KFA Jülich conducted under the U.S./FRG Umbrella Agreement on High-Temperature Reactor Development. The experiment was conducted in the R2 reactor at Studsvik, Sweden, for a 517 equivalent full power day irradiation. The capsule contained four independent cells, with cells 2 and 3 containing GA fuels and cells 1 and 4 containing German fuels. Details of the postirradiation examinations conducted on the GA-irradiated fuels are presented in ref. 4. This report presents the results of the postirradiation examinations conducted primarily at KFA Jülich, with some work being performed at ORNL, Studsvik, and GA. Conclusions and results derived from experiment R2-K13 are listed below.

1. The intact coated fissile and fertile particles in fuel rods performed satisfactorily, showing negligible SiC-fission product interaction and no significant amoeba migration in the TRISO LEU UCO particles. However, the particles failed to an extent beyond acceptable limits.

2. The reference-type fuel rods cured in place in multihole graphite bodies were in excellent condition at the end of irradiation, and the fabrication process was verified.

3. No deleterious effects of volatile spacers and lumped burnable poison wafers on fuel rod performance were observed.

4. The fuel performance models were verified in predicting fission gas release to within a factor of three; further work on the constituent fuel failure models is required to improve the agreement between observations and predictions.

5. The data on fission gas release during irradiation provided a basis for an improved model; the in-reactor, postirradiation measurement of zenon decay showed the steady-state fractional release of iodine to be less than or equal to that of xenon.

6. During irradiation, not more than 0.4% of the fission products escaped from the fuel rods, and less than 0.1% escaped from the graphite body. Less than 4% of the key fission product metals, cesium and silver, escaped from the particles except in the high-temperature cell where the silver release was about 60%.

7. The measurement of the distribution of cesium between the fuel rod matrix material and H-451 graphite confirmed the corresponding sorption isotherms and demonstrated the importance of irradiation damage in increasing the sorptivity of H-451 graphite.

8. The release of cesium and silver from the kernels of intact fissile particles was significantly less than that from similar particles with exposed kernels; for fertile particles no difference was found. Extensive formation of the fission product metal uranates was postulated to account for these observations.

9. Core heatup simulation tests were conducted with fuel rods containing TRISO LEU UCO and $ThO_2$ particles.

## 6.4 EQUIPMENT DEVELOPMENT AND MAINTENANCE

The irradiated microsphere gamma analyzer (IMGA), the shielded electron microprobe, and the postirradiation gas analyzer (PGA) are three major systems that are integrated into the PIE efforts at ORNL. Although they are used in routine PIE, they continue to require upgrading and maintenance in order that their reliability and capabilities to provide meaningful data are consistent with present day requirements.

During the past report period, the IMGA system has undergone a significant upgrade. The total system, with the exception of the remote cubicle, was replaced with new updated equipment. The remote cubicle was decontaminated and the interior modified to accept the new particle handler. A full description of the IMGA upgrade is provided in Section 6.4.1. Only a small amount of work was performed on upgrading the shielded electron microscope because of the higher priority IMGA work.

The state of the present system was thoroughly reviewed and recommendations made for new equipment. The PGA system was not utilized during this report period.

### 6.4.1 The Irradiated Microsphere Gamma Analyzer (IMGA) – M. J. Kania, C. A. Baldwin, and J. M. Keller

As reported in ref. 5, failure of the singularizer portion of the automated particle handler resulted in a significant decrease in the availability of IMGA in 1984. As a result, it was decided that, beginning in 1985, the IMGA cubicle would be decontaminated, the original handler removed, and, in its place, the new automated particle handler[6] installed. Preparation began in January 1985, and the upgrade of the IMGA system was completed in June 1985. The upgrade is a significant enhancement of the original IMGA system, which was put into operation in 1976.

Over the past two years, capital equipment to replace the original pulse height analyzer (PHA) system, the stereo microscopy stage, and the gamma selector had been obtained but not installed. In addition, the new automated particle handler, built in 1979–80, was also available. These items were not integrated into the IMGA system (replacing obsolete or non-supported equipment) because of the backlog in particle examinations. However, with the completion of capsule HRB-16 PIE and the delay in start-up of capsules HRB-17 and -18, sufficient time was available to complete the IMGA system upgrade.

Essential tasks that were completed to accomplish the IMGA system upgrade were as follows:

1. replaced the TP-5000PHA with a multi-user, multi-tasked ND-6700 PHA system integrated to the new automated particle handler hardware;
2. developed automated control software (FORTRAN based) for the particle handler to perform irradiated fuel examinations and analysis of gamma energy spectra;
3. replaced the original Ge(Li) detector with a new high-resolution gamma/X-ray detector capable of spectrometry in the energy range of 5 to 10 MeV;
4. installed an uninterruptable power supply system, with battery backup for one hour, for independent IMGA operation; and

5. modified the IMGA cubicle and installed the new automated particle handler.

The new particle handler was installed in July 1985. In-cubicle electrical and mechanical connections to permit external control of the handler were made. Figure 6.5 shows the particle handler and its electrical and mechanical connections through the cubicle wall. Figure 6.6 shows the new stereo microscope stage installed at the same time as the handler. Complete handler operation under control from the ND-6700 was demonstrated, and all components appeared to operate satisfactorily. For the next several months, the automated handler was tested under computer control to insure that all components of the IMGA system operated properly. Reliability was demonstrated in simulated particle examination runs for consecutive time periods in excess of 100 h. In November, all of the contaminated equipment removed during decontamination was returned to the cubicle. The alpha-shield was replaced, maintenance on the elevator to main cell area was completed, and the cubicle was sealed for remote operation.

Irradiated fuel from set 3 under the U.S./FRG cooperative program on fuel development was introduced to the IMGA cubicle shortly after its closure. These fuels will be the first examined with the upgraded system.

### 6.4.2 Shielded Electron Microprobe – J. M. Keller and M. J. Kania

A survey of the shielded electron microprobe facility located at the HRLEL indicated a need to upgrade and/or replace many of the current electronic components. The microprobe is based on out-of-date technology, and the original vendor of the probe is no longer in business. The current vacuum-tube electronics employed in the large power supplies provided questionable reliability and work performance characteristics relative to present-day standards. The probe was originally purchased in 1968 and over the years has required some new components, but it lacks many capabilities of microprobes available today. With no vendor support, maintenance problems requiring replacement parts are virtually impossible to correct.

The electronic components identified for replacement include the power supply modules, the beam-scanning electronics, and the wave-length dispersive spectrometers. The current single-channel analyzers need to be replaced with a computer-based multichannel analyzer system that will also

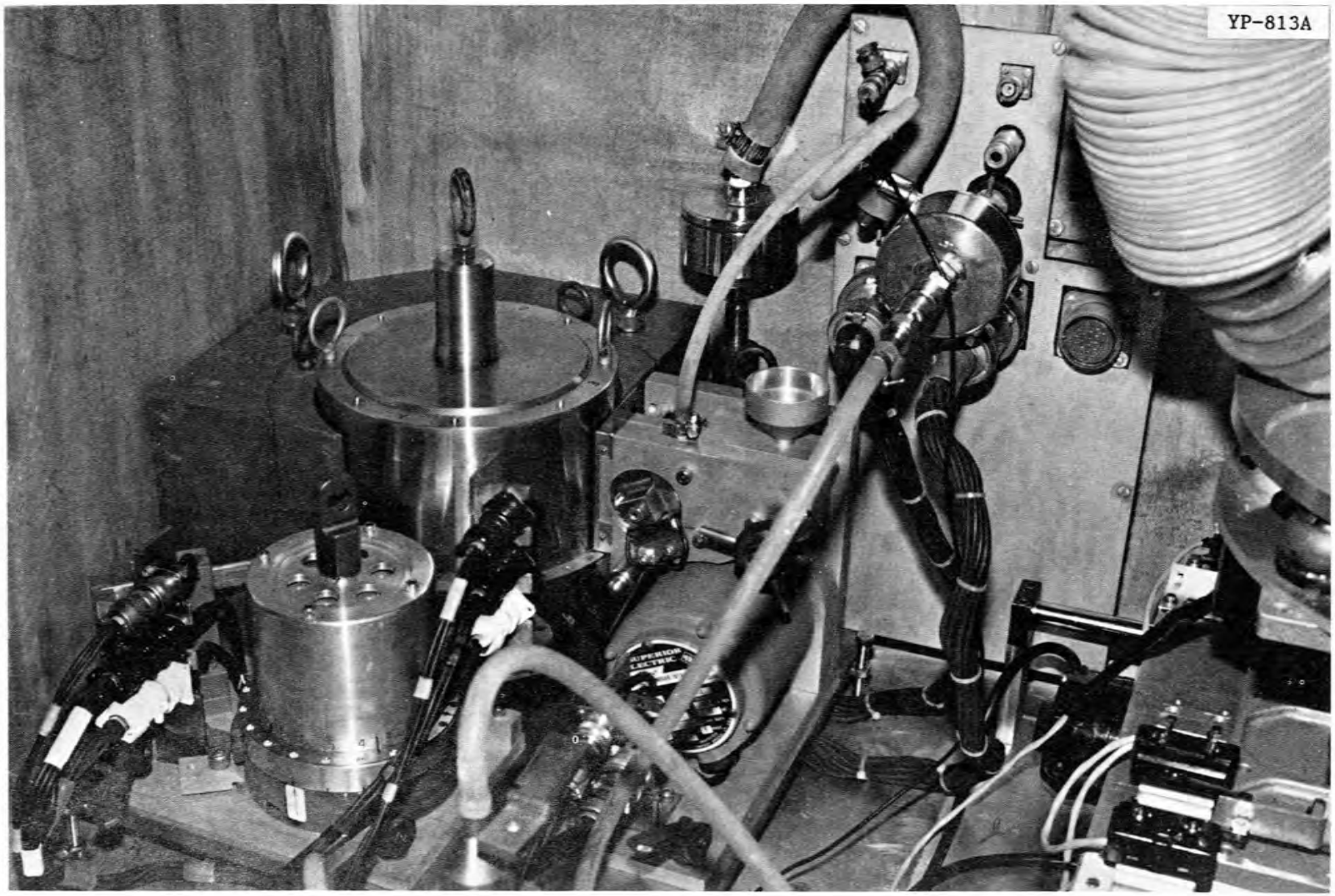


Fig. 6.5. The new automated particle handler installed in the IMGA cubicle. Electrical and mechanical connections pass through the cubicle wall to facilitate remote control with a computer-based operating system.

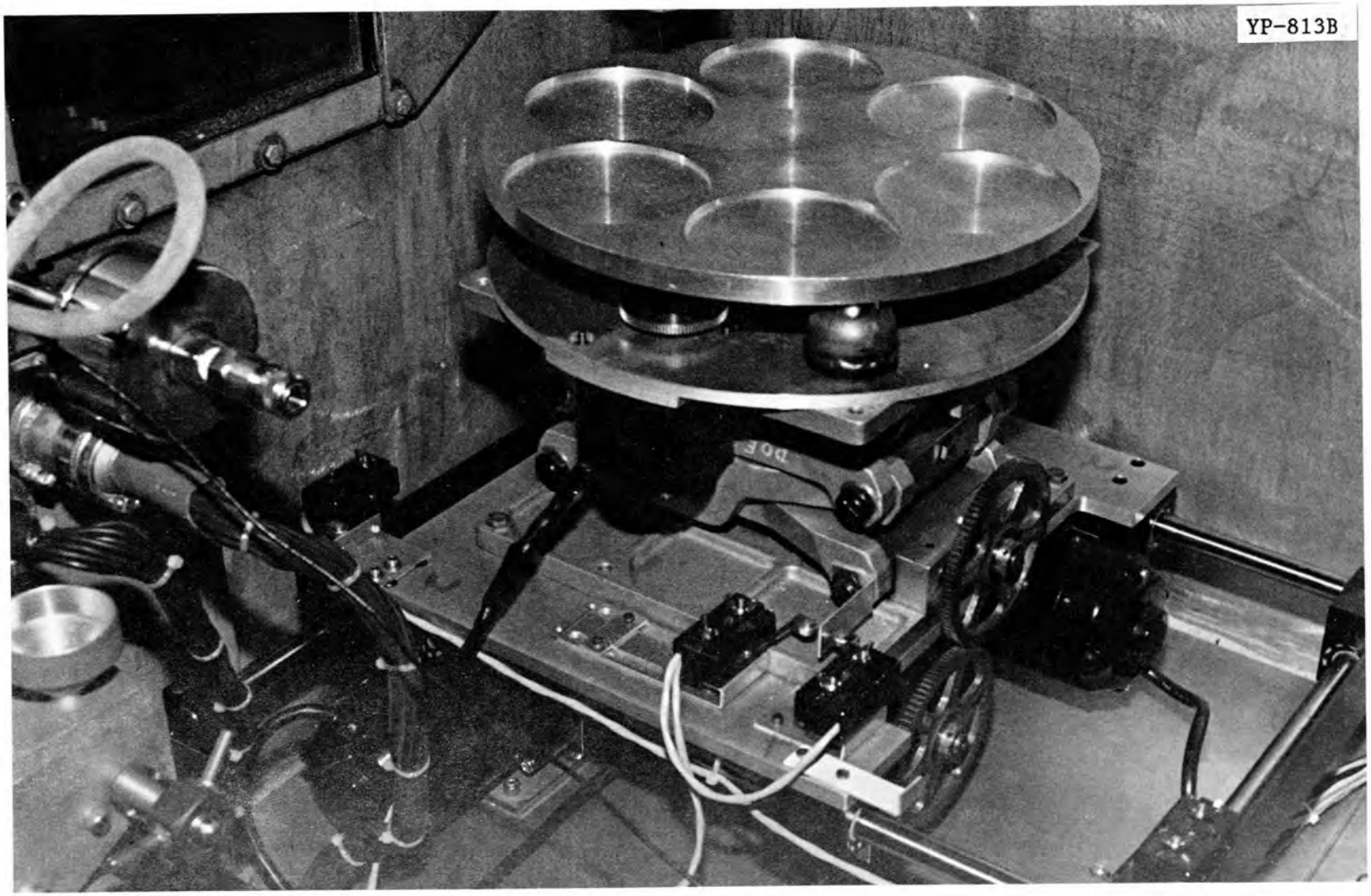


Fig. 6.6. The stereo microscope stage installed in the IMGA cubicle. This stage in conjunction with the stereomicroscope permits the visual characterization of coated particle fuels examined with the IMGA system.

provide advanced image processing capabilities. The vacuum and cooling systems require replacement or complete overhaul. To meet projected needs of the Fuels and Fission Product Behavior Programs, a shielded energy dispersive spectrometer needs to be installed and integrated with the pulse height analysis systems.

A small amount of work was completed on upgrading the vacuum and cooling systems. The vacuum system (diffusion pump, air valves, and mechanical connections to the beam column) has been replaced with a turbomolecular pump with air cooling and new mechanical connections. The beam column was also examined, and many defective vacuum seals were replaced. A vacuum sufficient to start up the probe was achieved and the system brought on line. However, the vacuum was insufficient to maintain operation. Continuation of the electron microprobe upgrade was halted because of the needs of the ongoing IMGA system upgrade.

## 6.5 REFERENCES

1. R. L. Senn, "Hydrolysis Experiments HRB-17 and -18," pp. 8–9 in *High-Temperature Gas-Cooled Reactor Technology Development Program Annual Progress Report for Period Ending December 31, 1982*, ORNL-5960, June 1983.

2. R. L. Senn and M. J. Kania, "Hydrolysis Experiments HRB-17 and -18," pp. 44–46 in *High-Temperature Gas-Cooled Reactor Technology Development Program Annual Progress Report for Period Ending December 31, 1984*, ORNL-6192, July 1985.

3. *Capsule HRB-16 Postirradiation Examination Report*, HTGR-85-053, September 1985.

4. *Capsule R2-K13: Final Report on Cells 2 and 3*, HTGR-85-068, September 1985.

5. M. J. Kania and G. A. Moore, "Irradiated-Microsphere Gamma Analyzer (IMGA)," pp. 71–72 in *High-Temperature Gas-Cooled Reactor Technology Development Program Annual Progress Report for Period Ending December 31, 1984*, HTGR-85-062, July 1985.

6. M. J. Kania, T. N. Tiegs, and G. A. Moore, "Irradiated Microsphere Gamma Analyzer," pp. 71–75 in *High-Temperature Gas-Cooled Reactor Technology Development Program Annual Progress Report for Period Ending December 31, 1980*, ORNL-5753, August 1981.

# 7. GRAPHITE (WBS 1602)*

W. P. Eatherly

## 7.1 GRAPHITE MATERIALS – INTERNALS (WBS 1602.01)

### 7.1.1 Chemical Impurities in Lots of 2020 Graphite – R. A. Strehlow

Three shipments (lots) of 2020 graphite were received at the Oak Ridge National Laboratory (ORNL) for tests and evaluation. Each lot consisted of three cylindrical billets measuring about 180 cm long by 25 cm in diam. The first lot was a standard or off-the-shelf 2020 graphite and was used in Test Zero of the Core Support Performance Test (CSPT) series.

The second and third shipments were the first iteration in the development of a nuclear-quality material by the manufacturer. These two shipments were designated nuclear lot 1 and lot 2.

It had been recognized earlier that stock or off-the-shelf 2020 graphite was not a satisfactory material for application as a permanent component in a gas-cooled reactor because of agglomerated impurities in the graphite and the variability of impurities from billet to billet.

The development plan involved the use of specially selected raw materials in order to avoid the agglomerated impurity problem and the use of a higher graphitization temperature in order to decrease the billet-to-billet variability. Nuclear-quality lot 1 was found still to have billet variability. It also was found still to have agglomerated impurities, but only after nuclear lot 2 had already been committed. As a consequence, the differences between lots 1 and 2 were not great, and a more detailed examination of the impurities was needed.

---

*These studies are jointly supported by the HTGR Technology Program and the Ceramic Technology for Advanced Heat Engines Project.

#### 7.1.1.1 Methods and Results

**Detection of agglomerates**

Agglomerate particles were detected by radiography of machined slab specimens that were routinely obtained. The specimens were 6.36 ± 0.13 mm (0.250 ± 0.005 in.) thick, machined to an rms 0.006-mm (250-microinch) smoothness. This precision has been found adequate to permit the obtaining of high-quality radiographic images. Sixty-nine radiographs of slab specimens were obtained adjacent to the regions from which samples for chemical analysis had been obtained. All of the radiographs for the three shipments showed agglomerated impurities.

No correlation was found between the number density and size range of the agglomerates and the chemical analysis of the adjoining graphite regions. Qualitatively, it appeared that a common size for the impurity agglomerates was about 0.3 mm. The number density of agglomerate particles estimated for several of the specimens fell in the range of 20 to more than 100 distinguishable particles per cubic centimeter. In general, the higher number densities were in regions of the specimen in which the particles were somewhat smaller, and conversely. Specimens of the nuclear-quality materials appeared to have the widest range of both size and number density as compared with the off-the-shelf graphite.

**Isolation and analysis of agglomerates**

Samples from some of the slab specimens were prepared for destructive examination in order to obtain isolated particles of the agglomerated impurities. Portions of slab specimens were cut to provide 6.4-mm-thick (1/4-in.) pieces about 25 by 152 mm (1 by 6 in.) in size, including the billet axis and the material along a radius to the circumference. Specimens of off-the-shelf material and of selected representative portions from lots 1 and 2 were used. These specimens were heated in air at about 900°C for 16 h on heavy platinum foil. This procedure oxidized the graphite, leaving an ash containing the inorganic impurities of the graphite in oxidized form. The ash that was formed in this procedure was examined visually, and portions were petrographically examined with a polarizing microscope. The off-the-shelf graphite specimens had numerous

regions of reddish-brown material with an extremely fine-grained structure and other regions of a white or cream-colored fine-grained structure, in which were observed particulates in the same size range as the agglomerates observed in the radiographic examination. Material from nuclear quality lots 1 and 2 showed no evidence of any colored material, but the appearance otherwise was similar to that of the off-the-shelf graphite.

Petrographic examination of the ash showed no crystalline areas larger than 20 μm or so. Most of the material was too small for petrographic study (<1-2 μm). The larger particles were agglomerates of very finely divided material. This inhomogeneity has not yet been explained. In the off-the-shelf graphite, more particles were found in areas of higher iron content.

Portions of the ash produced for these observations were subsequently examined by scanning electron microscopy and energy dispersive X-ray analysis. The results are shown in Table 7.1. These results are not calibrated and have only a relative significance with uncertainties of 10 to 20% of the specified value for those elements present in amounts of more than a few percent.

The table lists descriptions of different fields of view that were seen for each of the specimens listed. Because of the variation from field to field, qualitative phrases are used to refer to the different morphologies of the ash, e.g., particle, fines, plates, agglomerate, course material (relatively as compared with fine). Different parts of the billet produced ash that is described as being from the interior (near the billet axis), at the billet surface, or from an intermediate radius.

As seen in Table 7.1, agglomerate particles appeared to be dominantly calcium silicate with iron present in significant amounts only in the off-the-shelf material (billet 220).

The marked variability of composition from point to point in ash specimens of such widely differing types is not surprising. Some small particles showed distinct crystallinity and were found to contain high concentrations of titanium and vanadium in the case of samples from billet 24. Crystals such as the plates observed in the specimen from billet 220 might have been calcium sulphate after oxidation. These,

Table 7.1. Energy dispersive X-ray analysis results for ash from selected Stackpole 2020 graphite specimens[a]

| Billet number | Description | Analysis (wt % as element, assumed as oxide) | | | |
|---|---|---|---|---|---|
| | | Ca | Si | Fe | Other elements |
| 220 | Interior | | | | |
| | Particle | 6.0 | 4.7 | 38.6 | Ti, 14.5; V, 1.1 |
| | Fines | 22.0 | 21.1 | 7.1 | Cr, 0.5; Ti, 4.8; V, 2.2 |
| | Plates | 33.2 | 9.1 | 0.5 | S, 12.0; Al, 0.4 |
| | Intermediate | | | | |
| | Particle | 13.3 | 21.0 | 7.8 | Ti, 1.5; V, 0.8; Al, 10.8 |
| | Overall, av | 16.1 | 20.5 | 15.5 | Ti, 4.2; V, 1.7; Al, 0.5 |
| | Surface | | | | |
| | Fines | 5.7 | 34.3 | 7.5 | Ti, 0.4; S, 0.4; V, 0.4 |
| | Fines | 8.7 | 30.1 | 9.4 | Ti, 0.7; S, 0.3; V, 0.6 |
| | Particle (3 μm) | 17.5 | 19.4 | 17.5 | Ti, 1.3; S, 1.8; V, 0.8 |
| | Plate | 9.6 | 31.1 | 9.3 | Ti, 1.3; S, 0.6; V, 0.8 |
| 30 | Interior | | | | |
| | Agglomerate | 28.1 | 23.6 | 2.4 | S, 1.0 |
| | Agglomerate | 27.5 | 26.8 | 0.3 | Ti, 0.7 |
| | Fines | 35.5 | 11.1 | 2.5 | Al, 1.2; S, 1.9; Ti, 6.8 |
| | Surface | | | | |
| | Agglomerate | 24.0 | 23.9 | | S, 3.3; Ti, 1.3 |
| | Fines | 27.4 | 19.8 | | S, 6.0; Ti, 1.3 |
| 24 | Interior | | | | |
| | Agglomerate | 17.4 | 27.4 | 0.1 | S, 3.4; Ti, 1.3; V, 0.5 |
| | Intermediate | | | | |
| | Particles | | | | |
| | (20 μm) | 14.7 | 12.7 | 0.2 | Ti, 17.5; V, 3.7; S, 5.8 |
| | (40 μm) | 4.0 | 3.0 | | Ti, 45; V, 10 |
| | Surface | | | | |
| | Fine | 6.7 | 21.3 | | Ti, 27.4 |
| | Coarse | 20.7 | 18.2 | | Ti, 19.4 |

[a]Analyzed over visually selected relatively homogeneous areas, most generally about 1 $\mu m^2$.

course, are artifacts of a variable composition. These results are in general agreement with the results of chemical analysis, but obviously were not expected to reflect those results exactly.

**Heat treatment studies**

A group of Stackpole 2020 graphite pieces from lot 2 were regraphitized by the manufacturer in an attempt to thermally remove particulate impurities found in the materials that had been received earlier. This regraphitization was supposedly performed at a temperature higher than 2600°C, although we have reason to suspect this temperature was not attained. These graphite pieces were cylinders 48.3 cm (19 in.) long and 27 cm (11 in.) in diameter. A sample was taken for radiographic examination and analysis. A 6.4-mm (1/4-in.) slice from the end of one cylinder was radiographed to observe whether the particulates of inorganic impurities present in the piece had been altered or removed by the reprocessing.

The sample was found to have numerous particulates. In order to assess the nature of these impurities, the slice was cut into 12 wedge-shaped pieces. Each piece was then thermally treated in a laboratory furnace in an argon atmosphere by heating rapidly to heat treatment temperatures between 2000 and 3000°C and holding at the test temperature for 15 min. The wedge-shaped specimens were examined radiographically.

All of the specimens were affected by the heat treatment. It is particularly worth noting that, for the specimens heated to above 2500°C, voids formed at locations of particulates in the original material. The radiographic data and the ash analyses showed that, at heat treatment temperatures as low as 2400°C, a distinct decrease in impurities occurred.

Calculations and reference melting point data of vapor pressures or metals in equilibrium with either the metal or the carbides were compiled as appropriate. (For oxide particulates in contact with graphite, conversion to the carbide is favored.) The results of these calculations were in accord with the heat treatment studies.

### 7.1.1.2 Conclusion

These and other tests run in cooperation with The Stackpole Corporation resulted in the recognition of the source of the particulates and their removal by more elaborate processing steps.

### 7.1.2 Inhibition of Oxidation by Silicon – C. R. Kennedy

The use of 2020 graphite has been specified by the American Society for Testing and Materials (ASTM) Committee C5 as a standard material for the comparison of various industrial oxidation test procedures. The choice of 2020 was made because of the fine grain size and uniformity of the graphite. A major concern, however, was that the impurities in 2020 may catalyze the oxidation process more in some of the test procedures than in others, giving a bias to the test results. Therefore, because we have eliminated the catalytic effect of impurities in steam oxidation by simply thermally purifying 2020 graphite by a heat treatment to 2800°C, we suggested this treatment for the graphite specimens to be oxidized in the ASTM round robin. We then prepared a group of standard specimens of 2020 graphite with a 3000°C heat treatment for the ASTM round robin.

The oxidation results from the round robin evaluations were found to be quite confusing in that the graphite oxidized at much faster rates than initially expected. The oxidation rates between laboratories were in general agreement but were all so rapid that valid comparisons could not be made. Chemical analysis of one of the specimens by Stackpole Corporation indicated a fairly low impurity level. The specimen still contained impurities such as calcium, titanium, and vanadium but at reasonable levels. These results are given in Table 7.2 in comparison with ORNL results obtained from an ICAPES analysis of the as-received material and a heat-treated specimen. In general, there was very good agreement between the ORNL and Stackpole results, showing a significant reduction in the aluminum, calcium, iron, nickel, and silicon contents. The titanium, vanadium, and barium contents remained surprisingly unchanged. Also, while the calcium content was reduced significantly, 80 to 90 ppm was retained. These elements as simple carbides should have evaporated, which suggests that complex carbides having lower vapor pressures exist or were formed in the 2020 graphite. It was suggested at the ASTM Committee C5 meeting that the higher air oxidation rate was catalyzed by one or all of the impurities retained in the graphite. This is in conflict with our past results on steam oxidation, which indicated that iron and calcium were strong catalysts.

Table 7.2. Chemical analysis of 2020 graphite for ASTM round robin

| | As received | Heat-treated[a] specimen | Heat-treated[a] specimen analyzed by Stackpole |
|---|---|---|---|
| Ash, % | 0.119 | 0.029 | |
| Impurities, ppm | | | |
| Aluminum | 8.9 | 0.78 | 0.1 |
| Barium | 11.7 | 8.7 | 3.0 |
| Calcium | 333 | 92.8 | 82.0 |
| Cobalt | 0.08 | 0.02 | |
| Chromium | 0.56 | 0.23 | 0.2 |
| Iron | 53.6 | 1.9 | 2.0 |
| Magnesium | <0.06 | <0.03 | 0.02 |
| Molybdenum | 0.51 | 0.67 | 0.2 |
| Nickel | 0.51 | 0.19 | 0.19 |
| Silicon | 166.6 | <0.08 | 0.08 |
| Strontium | 8.1 | 2.6 | 7.0 |
| Titanium | 58.3 | 60.9 | 56.0 |
| Vanadium | 14.3 | 11.3 | 19.0 |
| Zirconium | 1.8 | 2.6 | 0.05 |

[a]Heat treatment: 3000°C for one-half hour.

This phenomenon was further examined by oxidizing specimens of 2020 and H451 graphite in flowing air in a thermogravimetric apparatus (TGA) heated at 2°C/min. The specimens were oxidized in the as-received conditions, heat treated to 2800 and 3000°C, and impregnated with polycarbosilane diluted with toluene to add silicon to the graphite. The results of the test series are similar to those shown in Fig. 7.1. The results are given in Table 7.3, where the temperature for a 50% weight loss is used to compare the materials. While the 2020 results tend to support the contention that silicon is an oxidation inhibitor, the H451 results tend to suggest that the silicon is actually countering the catalytic effects of either cobalt, titanium, or vanadium. There is some improvement in the oxidation of H451 by the silicon doping, but it is minor compared with the oxidation of heat-treated 2020 graphite. There also appears to be a threshold effect of the silicon content. Further additions of silicon do not continue to improve the oxidation resistance.

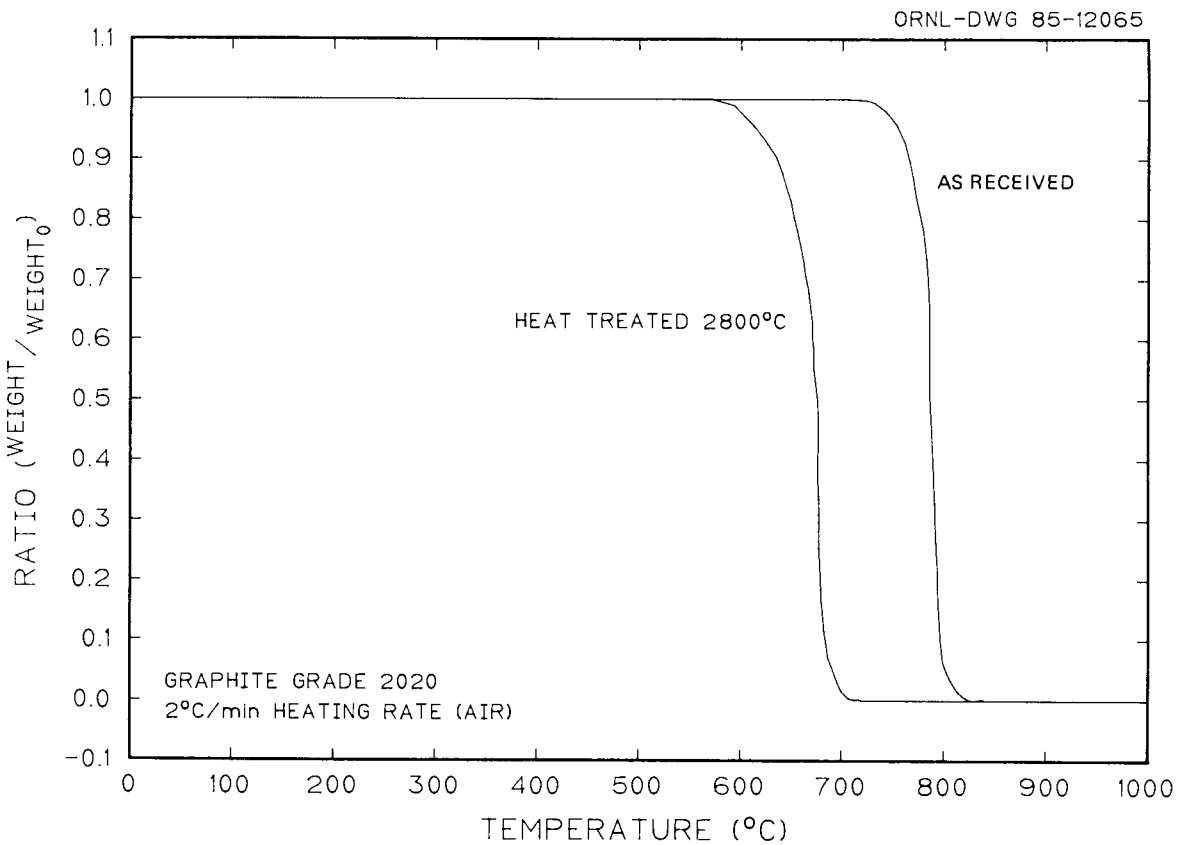


Fig. 7.1. Thermal gravimetric analysis results of air oxidation of graphite grade 2020.

Table 7.3. Temperature for 50% weight loss of graphite grades 2020 and H451

| Grade | Conditions | Number of polycarbosilane impregnations | Temperature (°C) |
|---|---|---|---|
| 2020 | As received | 0 | 780 |
| 2020 | As received | 1 | 770 |
| 2020 | As received | 1 | 770 |
| 2020 | As received | 2 | 780 |
| 2020 | 2800°C | 0 | 680 |
| 2020 | 3000°C | 0 | 680 |
| 2020 | 2800°C | 1 | 770 |
| H451 | As received | 0 | 780 |
| H451 | 3000°C | 0 | 775 |
| H451 | As received | 1 | 810 |
| H451 | As received | 1 | 805 |

Isothermal runs at 700°C (shown in Fig. 7.2) also demonstrated the significant difference in oxidation rates between the as-received and heat-treated material and the impregnated and as-received 2020 graphite. These results suggest that a small amount of silicon in the graphite would furnish some insurance against some forms of catalytic oxidation.

The question is, however, whether this effect will be similar in steam oxidation. This was examined by running isothermal tests on the H451 and 2020 graphite at 950°C in flowing argon saturated with water. The results, shown in Fig. 7.3, were similar in that there appeared to be no difference in the oxidation results. However, these oxidation rates and $H_2O/H_2$ ratios are considerably different from the HTGR environment and contrary to results obtained at GA Technologies, where silicon inhibition was observed. Therefore, the effect of silicon and its usefulness should be further evaluated under more realistic conditions before final conclusions can be made.

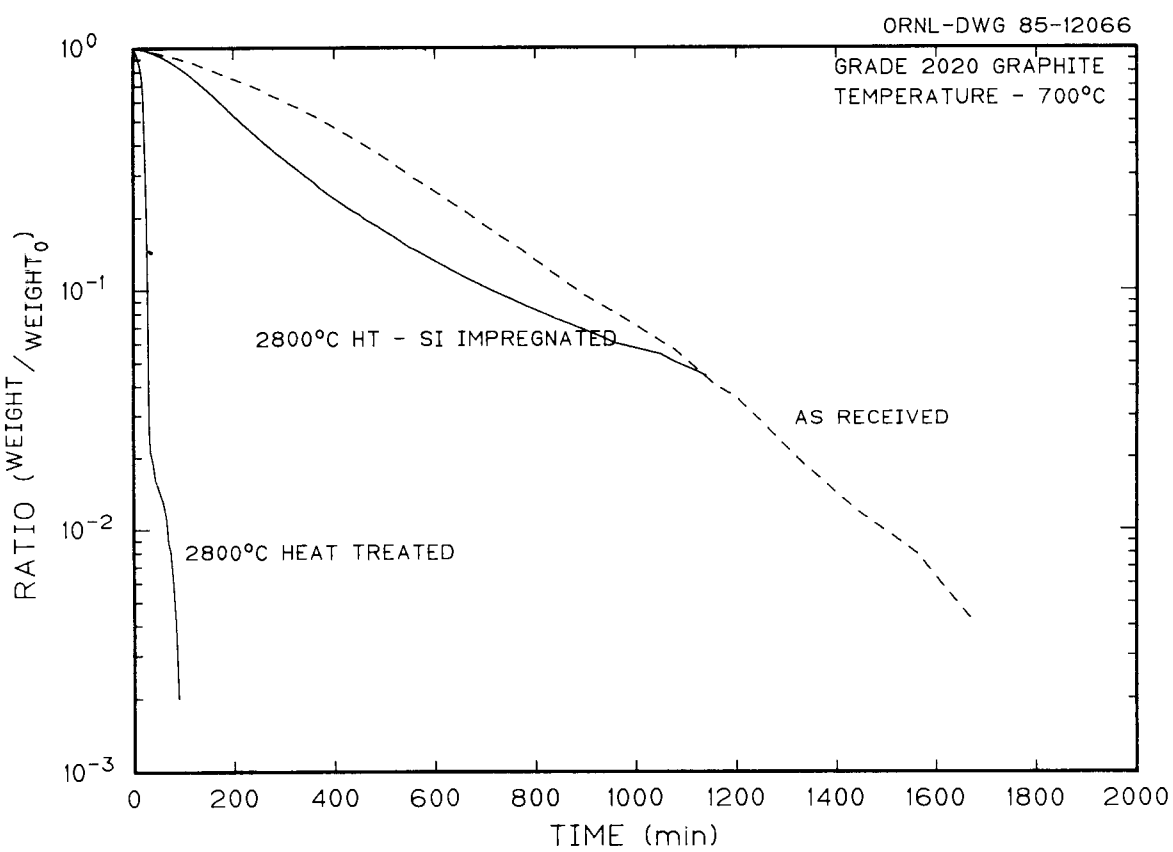


Fig. 7.2. Weight loss of grade 2020 graphite oxidized in flowing air at 700°C.

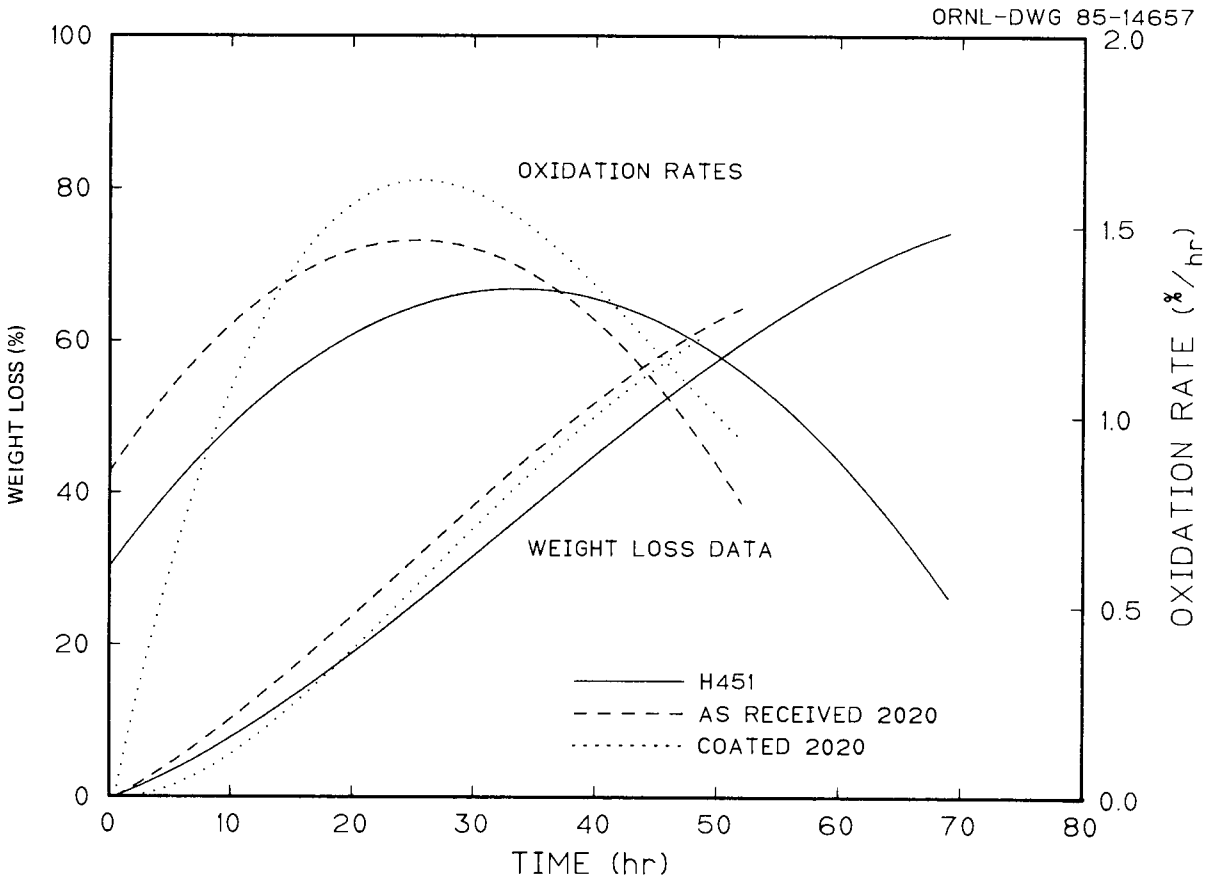


Fig. 7.3. Weight loss of graphite at 950°C in water-saturated argon.

## 7.2 GRAPHITE MATERIALS – CORE (WBS 1602.02)

### 7.2.1 Fracture Testing of Graphite – C. R. Kennedy

The brittle-ring test has been used successfully to measure the effect of stress volume on the fracture strength of graphite. The advantage of the brittle-ring specimen is that relatively small changes in the ring size yield large stress-volume size changes. The stress-volume effect is a direct result of the changes in the probability of fracture by changing the stress volume relative to the flaw distribution. Thus, it is possible to quickly determine if variables, such as oxidation, will alter the statistics of fracture by evaluating oxidized rings of different size determining the effect of stress volume. This has been done for both 2020 and H451 graphite, demonstrating that oxidation will not change the fracture statistics. The same procedure can be used to determine if the statistics are changed or altered under fatigue conditions.

Brittle rings of 29, 25.4, and 38.1 mm with the same wall thickness of 5 mm have stress volumes that vary over an order of magnitude. Each specimen size was fatigue tested with a ratio of R = 0 (R = ratio of maximum stress to minimum stress). The results were typical of fatigue data as shown in Fig. 7.4 for H451 graphite. Figure 7.5 shows the stress for $10^5$ cycles as a function of stress volume compared with standard brittle-ring results. The slope of the stress-volume plot is the reciprocal of the Weibull *m* value, and in Fig. 7.5 it is clear that the fatigue results have the same slope. Thus, it appears that the strength variability is the same under fatigue as under monotonic loading. This is further confirmed by the data in Table 7.4, giving results of all of the fatigue testing compared with monotonic strength values. While the ratio of fatigue strength to monotonic strength does vary with material, the ratios are constant and independent of specimen size. This is fairly conclusive evidence that the fracture characteristics derived by monotonic loading are applicable to fatigue behavior.

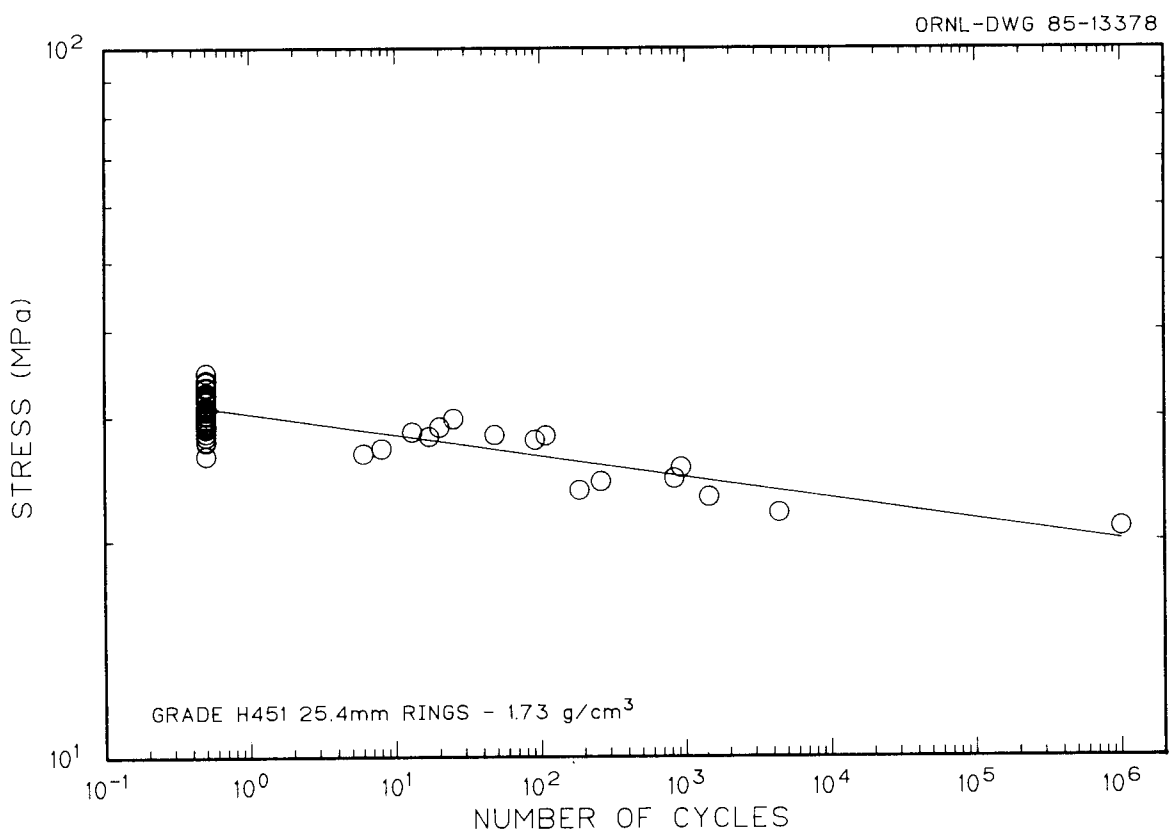


Fig. 7.4. Fatigue strength of 25.4-mm rings of H451 graphite.

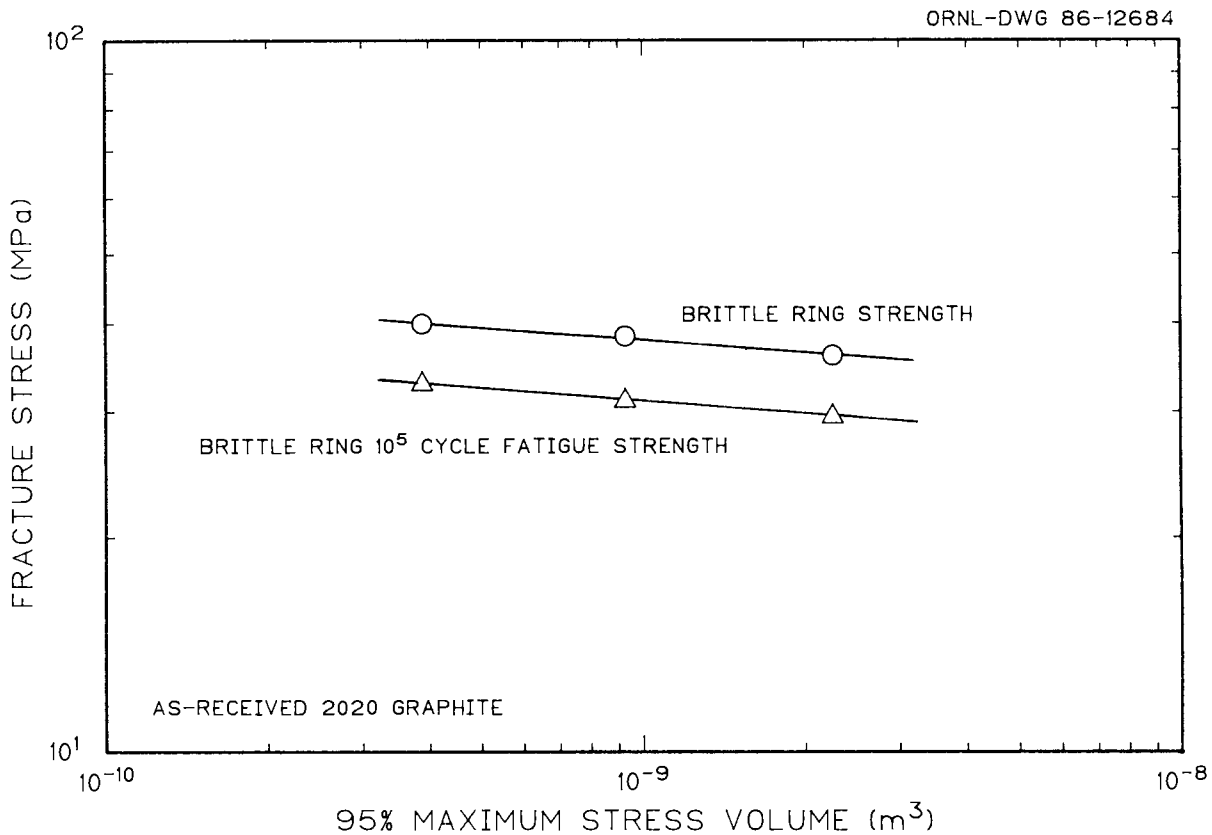


Fig. 7.5. Effect of stress volume on fatigue loading of 2020 graphite.

Table 7.4. Fatigue strength of H451 and 2020 graphite rings (R = −1)

| Grade | Condition | Ring diam (mm) | Strength ratio |
|---|---|---|---|
| 2020 | As received | 19 | 0.82 |
| 2020 | As received | 25.4 | 0.81 |
| 2020 | As received | 38 | 0.82 |
| 2020 | 2800°C | 19 | 0.84 |
| 2020 | 2800°C | 25.4 | 0.84 |
| H451 | As received | 19 | 0.69 |
| H451 | As received | 25.4 | 0.75 |
| H451 | As received | 38 | 0.74 |

## 7.3 GRAPHITE MATERIALS – TECHNOLOGY (WBS 1602.03)

### 7.3.1 Considerations in Selection of Multiaxial Failure Criterion for Use in Design of HTR Graphite Components – G. T. Yahr

The important considerations in the selection of failure criteria for use in the design of HTR graphite components were examined. The prior work on mechanistic theories including statistical theories and fracture mechanics were reviewed. Candidate phenomenological theories including the maximum stress theory and Tsai-Wu tensor theory were reviewed and compared with available data. The fracture criterion is only one important aspect of the design process. It is important to consider how it relates to the other aspects including the constitutive model and analysis methods. Existing data should be used to benchmark the design process including the most promising multiaxial failure criteria. Comparisons of the results of those benchmark problems should then be used to guide the selection of a recommended multiaxial failure criterion for use in the design of HTR graphite components.

#### 7.3.1.1 Introduction

The important considerations in the selection of failure criteria for use in the design of high-temperature reactor (HTR) graphite components were examined. An objective consideration of the pertinent factors and the available data makes an intelligent selection of failure criteria possible. The selection of a failure criterion must be based on an understanding of the failure of graphite. The enormous amount of research that has been done on fracture in graphite is summarized in ref. 1. Several papers[2-5] have been published that address the selection of failure criteria for use in the design of graphite structures, and a subsection on design requirements for graphite core support structures in nuclear reactors has been prepared for publication as part of the ASME Boiler and Pressure Vessel Code.[6]

First we should establish the need for a failure criterion. Graphite is required to serve as a structural member in an HTR. Stresses are induced by thermal expansion and irradiation-induced dimensional changes as well as by mechanical and pressure loads. The only feasible way to design such structures is "design by analysis." In this case "design by

analysis" means the calculation of stresses and strains in the graphite components by using elastic or inelastic finite-element computer codes. An allowable stress or strain value is required to establish whether or not the calculated stresses and strains are acceptable. Note that the designer must have some degree of confidence that the component will not fail in service. Therefore, the allowable stress or strain value that the calculated stresses and strains are compared with must be low enough that its use can be expected to preclude failure with the desired degree of confidence. The selection of allowable stress or strain values must start with the stress or strain value that would cause failure of the material. This value must be reduced to account for the inherent statistical variability, for all the factors that can reduce the strength, and for the uncertainties in the analysis that cause the calculated stress or strain to be less than the stress or strain that will actually occur in the component. Factors that can affect the strength include oxidation, irradiation, temperature, geometric size, and multiaxiality. Uncertainties in the calculated stresses or strain arise because of the variability in mechanical, thermal, and irradiation properties, inaccurate constitutive equations, dimensional tolerances, and uncertainties in the operational loads, temperatures, and irradiation history. Small allowances for strength reduction rapidly accumulate. An example from the literature will illustrate this point. Manjoine and Tome[7] discuss the derivation of the fatigue design curves for austenitic stainless steel of the ASME Boiler and Pressure Vessel Code.[8] As they point out, the measured fatigue strength data were reduced by a "safety factor" of 2 which accounts for a 15% reduction for each of five variables (surface finish, volume, material variability, corrosion, and residual stress). Several other variables including multiaxial loading effects are left for the designer to account for. Note that, in this example, the pessimistic assumption that all five factors would act simultaneously in the worst possible way was used (total correlation).

A more realistic approach is to assume all variables are independent (no correlation). Then, the way to compound the factors is to take the square root of the sum of the squares of the possible strength reduction from each source. When the measured stress or strain values are reduced

this way to arrive at an allowable value, then if the reduction due to one of the factors is already small with respect to any of the others, making that factor even smaller will have little effect on the overall reduction. Therefore, it is important not to concentrate on any one factor such as multiaxiality to the exclusion of all others. To illustrate this, the coefficient of variation of the tensile strength of H451 graphite has been reported[9] to be 11.8%. Assuming a normal distribution and a sample size of 50, the allowable strength value must be reduced by 2.863 standard deviations[10] to be 95% confident that the probability of failure would be 1%. This requires a strength reduction of 34% to account for material variability. The maximum strength reduction due to equibiaxial tensile stress is typically 15% (ref. 1). Because of the greater strength reduction required to account for the statistical material variability, one must be careful not to put undue effort into precise modeling of the multiaxial effects.

Multiaxial failure criteria are discussed in the following section. The available multiaxial failure data are then discussed in Section 7.3.1.3. Recommendation of the failure criterion that shows the most promise is given in the last section along with recommendations for research that must be done before it is ready for application.

#### 7.3.1.2 Multiaxial Failure Criteria

Material strength is usually characterized by measuring the uniaxial strength. In application, however, materials are usually subjected to multiaxial stress conditions. Therefore, a multiaxial failure criterion is necessary so that the uniaxial strength data can be applied to component design. There are two general approaches to multiaxial failure criteria. One is a mechanistic approach, wherein the failure criterion is developed on the basis of the fundamental mechanisms that cause fracture. An example of this approach is the Griffith-Irwin fracture mechanics approach. The other approach is phenomenological in which a surface is developed in stress-space that fits the available data and meets certain geometrical requirements as well. Examples of the phenomenological approach include the maximum stress theory, the maximum strain theory, and the Tsai-Wu tensor theory. The advantage of the phenomenological approach is that, with enough constants, the available data can always be accurately

described. However, care must be used to make sure it is not applied to conditions that have not been tested, as it is strictly a mathematical curve fitting procedure. Thus interpolation between known conditions is reasonable, but extrapolation is dangerous.

Mechanistic theories can be used to extrapolate beyond known conditions with more confidence and often account for other factors such as size, surface finish, flaws, irradiation effects, and temperature. However, they generally require a better understanding of the failure process and are more difficult to develop.

**Statistical failure theories**

Variability in strength is a characteristic feature of graphite. The nature of the observed scatter must, therefore, be analyzed by statistical techniques. Unfortunately, extremely large numbers of tests are necessary in order to discriminate between different candidate statistical distribution functions especially with regard to the lower tail of the distribution, which is where our interest lies.

An alternative approach is to establish mechanistically based statistical models, which can then be used for extrapolation beyond the range of observation, not on the basis that the distributions they produce can be fitted to existing test conditions (which is not a sufficient conditions) but that they are germane to the phenomenon. Statistical failure theories are briefly discussed below. The reader is encouraged to refer to the cited references for additional information.

The variability of the fracture strength of graphite and dependence of strength on specimen volume have led a number of investigators[1,11-19] to consider the use of Weibull's statistical theory of strength[20] to describe the behavior of graphite.

Weibull postulated that within every unit volume of material there are flaws, distributed at random both in severity and position, that cause the material to be weaker at some locations than at others; furthermore, if failure occurs at the weakest location, the entire structure fails. The natural consequence of this postulate is that the larger the volume or surface area of material subjected to stress, the higher the likelihood for failure. This is the size-effect postulate, or the weakest-link hypothesis. Expressed mathematically,

$$P(X < x) = 1 - \exp\left[ - \int_V \sigma_n \, dV \right] ; \tag{1}$$

that is, the probability $P$ that the strength $X$ is less than some number $x$ is given by 1 minus the exponential raised to minus the volume integral of some function $\sigma_n$. The bracketed quantity is sometimes called the risk of rupture; $\sigma_n$ is some, as yet unspecified, function that describes the state of stress in the volume and the parameters that govern failure of the material.

Weibull chose a three-parameter function,

$$\sigma_n = \left( \frac{x_V - x_u}{x_o} \right)^m , \tag{2}$$

where $x_u$ (the minimum strength), $x_o$ (the volumetric scale parameter), and $m$ (the shape parameter) are constants peculiar to a given material and $x_V - x_V(\vec{r})$ is the stress distribution as a function of position within the volume or surface area $V$ as the case may be.

When Eqs. (1) and (2) are combined, the result is Weibull's statistical theory of strength, as expressed by

$$p(X < x) = 1 - \exp\left[ - \int_V \left( \frac{x_V - x_u}{x_o} \right)^m dV \right] . \tag{3}$$

Two quantities are now introduced. One is defined as the critical volume $kV$ and is given by

$$kV = \int_V \left( \frac{x_V - x_u}{x_m - x_u} \right)^m dV \qquad x_V \geq x_u , \tag{4}$$

where $k$ is a stress distribution parameter, $k \geq 1$, and $x_m$ is the maximum stress in the body.* The second is the scale parameter $\theta$, which is given by

$$\theta = x_o \, (kV)^{-1/m} . \tag{5}$$

---

* Note that the critical volume $kV$ is undefined if the maximum stress $x$ is less than the minimum strength $x_u$, and consequently the integral should be evaluated only over the portion of the volume for which the stress $x_V(\vec{r})$ is greater than the minimum strength.

Through the use of these quantities the familiar form of Weibull's cumulative distribution function is obtained:

$$P(X < x) = 1 - \exp\left[-\left(\frac{x - x_u}{\theta}\right)^m\right] . \tag{6}$$

The probability density function is

$$\begin{aligned} f(x) &= \frac{m}{\theta}\left(\frac{x - x_u}{\theta}\right)^{m-1} \exp\left[-\left(\frac{x - x_u}{\theta}\right)^m\right] \text{ ; for } x_u \le x \le \infty \\ &= 0 \text{ elsewhere.} \end{aligned} \tag{7}$$

The mean is given by

$$\mu = x_u + \theta\Gamma\left(1 + \frac{1}{m}\right) , \tag{8}$$

and the variance is

$$\sigma^2 = \theta^2 \left[\Gamma\left(1 + \frac{2}{m}\right) - r^2\left(1 + \frac{1}{m}\right)\right] , \tag{9}$$

where $\Gamma$ is the complete gamma function, $x_u$ is the absolute minimum, and $m$ is the shape parameter.

In order for the theory to hold, two conditions must be satisfied. First, experimental data must be distributed according to Eq. (6); that is, failure stress for a sufficiently large number of specimens of equal volume must be distributed according to a Weibull probability density function given by Eq. (7). Second, if the first condition is met, the scale parameter $\theta$ must obey Eq. (5) for specimens with different volumes. Testing these two conditions is equivalent to testing the hypotheses of the theory. If the data fit a Weibull probability distribution function $f(x)$, the postulate concerning $\sigma_n$ is valid. If the data fit a Weibull distribution function *and* the scale parameter $\theta$ is assumed to be volume dependent according to Eq. (5), the weakest-link hypothesis is also valid. These two conditions form a necessary and sufficient set for testing the validity of the theory.

Several investigators have concluded that the parameter $x_u$ should be set equal to zero.[17,21,22] This has the effect of reducing the three-parameter Weibull distribution function to one of two parameters.

Both the three-parameter and the two-parameter Weibull distributions will adequately describe the statistical variation of strength values obtained from specimens of identical shape and size. However, the normal distribution will do so also when $m$ is in the range from 5 to 10. An extremely large number of specimens would be required to determine which statistical distribution gives the best representation of the strength distribution of a particular graphite.

Weibull's statistical theory of strength predicts an increase in mean strength as the specimen volume decreases. It also predicts a similar increase in variance. Experimental observations[19] showed a definite volume dependence on mean strength over the observed range of critical volumes from 0.025 to 15.9 $cm^3$ (0.0015 to 0.971 $in.^3$); the small specimens were 38% stronger than the large specimens. A definite effect of specimen volume on the variance was not observed. In general, the experimentally observed size effect on mean strength was somewhat less than predicted from Weibull's theory using parameters obtained by fitting the strength distribution of a group of similar specimens. On the basis of these studies, it was concluded that Weibull's theory does not provide an adequate description of graphite failure.[19] It might, however, be used along with strength data from small specimens as a conservative estimator for the strength of large specimens.

Let us now consider several explanations for the observed tendency for the size effect on strength to apparently be overpredicted by Weibull theory. Weibull based his theory on the natural variation of the strength of a brittle material. The variations in strengths that one records from a group of identical specimens include variations from other sources as well, however. Sources of variation above and beyond the inherent variation in strength due to the naturally occurring flaws that Weibull considered include, but are not limited to, such things as variations in dimensions of the specimens, nonuniform loading, specimen damage during handling, variations in load-recording instrumentation, and human error. Therefore the variation in strength that one obtains from a set of identical specimens is the combination of the variation in strength that results from the flaws in the material which Weibull considered plus variations from other sources. The relationship between mean strength and volume for two sets of specimens is given by

$$\frac{(\sigma_m - x_u)_1}{(\sigma_m - x_u)_2} = \left[ \frac{(kV)_2}{(kV)_1} \right]^{-1/m} , \tag{10}$$

where $\sigma_m$ is the mean strength and subscripts 1 and 2 refer to the two sets of specimens. Thus the Weibull volume effect is less for large than for small $m$ values given the same value of $x_u$. Since the value of $m$ is related to the scatter of the data, a larger value of $m$ is obtained if the data scatter decreases. Because it would seem that the recorded data are more widely distributed than they would be if only the variation of flaws in the material were causing strength variations, one would expect the true $m$ value for the material to be less than the one obtained by fitting the Weibull distribution to the strength data. This would tend to reduce the present discrepancy between measured and predicted volume effect. Unfortunately, it is often difficult to separate the strength variation due to flaws in the material from other sources of variation in recorded strength values. In a series of tests on brittle ring specimens, C-ring specimens, and flexure specimens, Kennedy[23] segregated his specimens into three groups based on the bulk density to eliminate one important extraneous source of variability and obtained good agreement between the actual volume size effect and the Weibull volume size effect.

Eatherly[24] has shown that there are two distinct types of flaws in H451 graphite, which can be classified as either background or disparate. These flaws give rise to a bimodal strength distribution. The background flaws generally cause fracture, but, when a less frequent disparate is present, the strength is greatly reduced. This has the effect of broadening the strength distribution, thus producing a relatively low Weibull $m$ value which causes an overprediction of the volume size effect.

Eatherly[25] has recently presented a new bimodal statistical model that accounts for the observed effect of disparate flaws on the strength of graphite. It is a weakest-link model based on a finite cell that employs binomial and order-statistics to describe the probability of failure as a function of stress volume and data-base specimen geometry.

On the other hand, Weibull's statistical theory of strength is based on the weakest-link concept, that is, when the initial failure occurs, the specimen breaks. This is not true for graphite; microscopic studies of graphite during loading[26-28] have shown that cracks are produced by loads

well below the fracture load, that they are stopped, and that fracture of the specimen finally occurs when a number of these small cracks coalesce. A statistical theory of fracture that would be appropriate for graphite should also take this into account. Such a statistical model has been formulated by Hasofer.[29] In Hasofer's model, fracture is assumed to occur by coalescence of a number of arrested cracks initiated at different points. The size effect in this model is less marked than in the case of weakest-link models. Further study of Hasofer's model should be considered.

An alternate explanation[1] for the inability of the Weibull model to properly account for size effects is a grain size effect. The Weibull theory assumes that rupture of any small element of volume is not influenced by its neighbors, but this is not true if the size of the element is not large relative to the size of the defect that initiates fracture. At very small specimen sizes, this effect would lead to larger specimens actually being stronger than smaller specimens. Experiments[1] do show such an effect with very small specimens. By introducing a "grain size correction factor," Ho[30] was able to use the Weibull model to obtain good correlation to a set of experimental data on notched graphite specimens.

The general relationships for treating biaxial tensile stress were given by Weibull.[20] He assumed that the normal tensile stress is the only stress that effects failure. By setting $x_u = 0$ and summing the normal tensile components of stress over a half sphere, the probability of survival is

$$P(X < x) = 1 - \exp\left[ - \int_V \int_o^{2\pi} \int_o^{2\pi} \left(\frac{x_n}{x_o}\right)^m \cos\phi \, d\psi \, d\phi \, dV \right] , \qquad (11)$$

where $\phi$ and $\psi$ are the angles of latitude and longitude and $x_n$ is the normal tensile component of stress. Price and Cobb[17] calculated the failure envelope in the biaxial tensile quadrant for values of $m$ between 2 and 20 that are shown in Fig. 7.6. In the tension-compression quadrant, the Weibull theory predicts that the maximum tensile stress at failure increases as the compressive stress component increases.

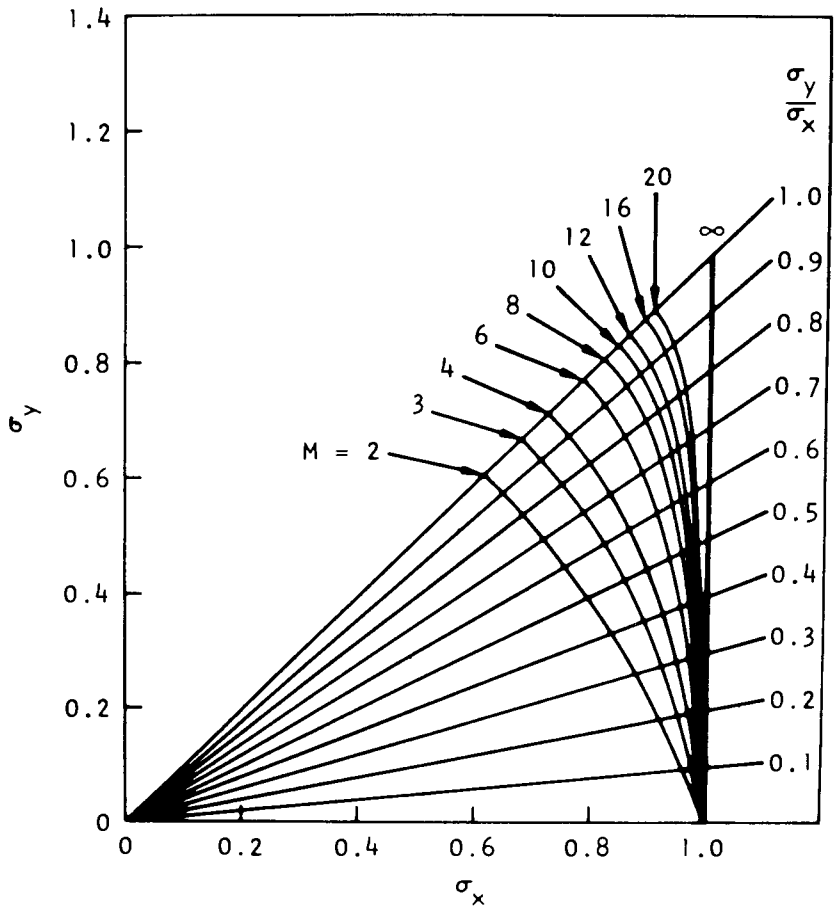


Fig. 7.6. Biaxial failure envelope in tension-tension quadrant predicted by Weibull theory for *m* values from 2 to 20. *Source*: R. J. Price and H. R. W. Cobb, "Application of Weibull Statistical Theory to the Strength of Reactor Graphite," pp. 547-67 in *Proceedings of the Conference on Continuum Aspects of Graphite Design*, CONF-701105, available from National Technical Information Service, Springfield, Va., February 1972.

Although, as mentioned above, Weibull used the assumption that the normal tensile stress is the only stress that effects failure, other assumptions can be used. Batdorf[31,32] has investigated the use of other fracture criteria in the Weibull formulation, but additional work in this area is still needed before it can be considered for application to design.

**Fracture mechanics**

Fracture mechanics has been developed to account for brittle failures that occurred in welded Liberty ships and high-strength welded steel structures such as rocket motor casings. The traditional design approach

using a factor of safety to limit the maximum calculated stress level to some percentage of either the yield or ultimate strength was not adequate for the design of structures that operated in the brittle regime and sometimes had pre-existing flaws or severe stress concentrations. Linear elastic fracture mechanics (LEFM) was, therefore, developed and used to understand such failures. It is now a well-established method for designing such structures.

Because of the limited ductility exhibited by graphite and the inherent cracks that are induced when it is cooled from being graphitized, it is quite natural to assume that fracture mechanics should be applicable to graphite. Fracture mechanics methods have been applied to graphite under uniaxial stress states by a number of investigators.[33-39] These studies as well as a study of the effect of grain size on strength[40,41] indicate that fracture mechanics is applicable to graphite.

The basic fracture mechanics parameter used in engineering analyses is the stress-intensity factor at onset of rapid crack propagation, $K_c$, which has the units MPa$\sqrt{\text{m}}$ or ksi$\sqrt{\text{in.}}$ Elastic stress analyses are used to establish the relationship among applied load, crack length, and stress-intensity factor for each specimen geometry. The value of $K_c$ is then determined from the crack length and load at fracture; the strain-energy release rate at the onset of rapid crack propagation, $G_c$, is an alternative fracture mechanics parameter related to $K_c$ by the equation

$$G_c = \left(\frac{1 - \nu^2}{E}\right) K_c^2 \tag{12}$$

for plane strain conditions or

$$G_c = \frac{K_c^2}{E} \tag{13}$$

for plane stress conditions, where $\nu$ is Poisson's ratio and $E$ is the modulus of elasticity. Because of the low Poisson's ratio exhibited by graphite, Eq. (13) can generally be used with sufficient accuracy for all loading conditions.

Fracture toughness is a minimum under plane-strain conditions. Furthermore, under plane-strain conditions the mode of fracture is a wedge opening of the crack, which is customarily referred to as mode I. The stress-intensity factor at onset of rapid crack propagation under plane-strain conditions is referred to as $K_{Ic}$. The controlling parameter for design to avoid brittle fracture is generally $K_{Ic}$.

Investigators[42] have shown that the $K_{Ic}$ value for crack initiation can be measured using notched beams and compact tension specimens. Another fracture toughness, which we shall call the crack-extension resistance, $K_R$, is a measure of the resistance to crack extension and can be measured using the double cantilever beam specimen or short-rod chevron specimen. $K_R$ is larger than $K_{Ic}$ for graphites. For example, $K_{Ic}$ for Poco AXM graphite is 1.30 MPa$\sqrt{m}$ (1.18 ksi$\sqrt{in.}$), and the $K_R$ value is 1.54 MPa$\sqrt{m}$ (1.40 ksi$\sqrt{in.}$) (ref. 19). For Stackpole 2020 graphite the $K_{Ic}$ and $K_R$ values are 0.74 MPa$\sqrt{m}$ (0.67 ksi$\sqrt{in.}$) and 0.91 MPa$\sqrt{m}$ (0.83 ksi$\sqrt{in.}$) (ref. 5). The $K_{Ic}$ values would be the primary property the designer would use to prevent fracture. The $K_R$ value would be used if the designer were required to go one step further and determine how far the crack would grow before it stopped.

Both AXM and 2020 are isotropic graphites. Most graphites are transversely isotropic and have a higher strength in the with-grain direction than in the across-grain direction. Kennedy[43] has reported that the $K_R$ value for anisotropic AGOT graphite is essentially independent of loading direction. He reported $K_R$ values of 1.37 MPa$\sqrt{m}$ (1.25 ksi$\sqrt{in.}$) for loading in the with-grain direction and 1.29 MPa$\sqrt{m}$ (1.17 ksi$\sqrt{in.}$) for loading in the across-grain direction. However, Corum[30] reported $K_{Ic}$ values of 0.92 MPa$\sqrt{m}$ (0.84 ksi$\sqrt{in.}$) and 0.59 MPa$\sqrt{m}$ (0.54 ksi$\sqrt{in.}$) for AGOT graphite for with-grain and across-grain loading, respectively.

Once it has been established that $K_{Ic}$ and $K_R$ values can be measured on specimens with machined notches, it must then be established that they are applicable to graphite components with the inherent small flaws that they may contain. Some of this work has been done. Beams similar to the notched beams used to measure $K_{Ic}$ were tested to failure, and a flaw size was calculated using the equation that had been used to calculate $K_{Ic}$ from the notched-beam tests. The calculated notch depths for the three graphites examined were about the same size as the microstructural features in

the respective material.[44] As further evidence that the fracture mechanics method is applicable to the naturally occurring flaws in graphite, fracture mechanics was used to calculate the strength of a 25.4-mm-diam (1-in.) across-grain ATJ tensile specimen that failed at a stress of only 12.9 MPa (1875 psi). An apparent flaw was observed in the fractured surface. Using a fracture mechanics analysis with the observed flaw size, the strength was calculated to be 13.5 MPa (1970 psi).

Three series of tests were done to examine the ability of LEFM to predict fracture of graphite under multiaxial stress states. One test series consisted of tests on splitting tensile specimens of AXM and ATJ graphites.[45] The splitting tensile specimens were cylindrical or elliptical disks that were loaded in compression along the major axis of the ellipse. Nearly uniform biaxial stress states exist in the central portions of circular or elliptical disks loaded by lateral compressive loads. The maximum tensile stress occurs normal to the loading direction at the center of the disk and is the maximum principal stress at that point. The minimum principal stress at the center is compressive. The ratio of the absolute values of the principal stresses is dependent on the shape of the disk; it ranged from 3.0 to 6.9 in the specimens tested. Slots in the central region that were aligned with the loading direction caused premature failures that were predicted very accurately using fracture-mechanics methods.

Since these tests demonstrated that fracture-mechanics methods can be used for predicting the fracture of graphite under biaxial stress conditions where one principal stress is tensile and the other is compressive, other combined stress states were considered. The second test series was an investigation of fracture under the complex stress conditions that exist in an internally pressurized thick-walled cylindrical vessel with a flat head.[46]

Two sets of specimens were used. The first set had complete circumferential notches machined diagonally into the head-cylinder juncture region, while the second set was unnotched. The methods of linear-elastic fracture mechanics and a finite-element analysis were used to predict pressures to cause fracture for both notched and unnotched specimens. In the latter case, it was necessary to postulate a "size" for a naturally occurring flaw. These predicted pressures were in good agreement with

measured results for the vessels with machined notches. The unnotched vessels, however, withstood a greater pressure than was predicted, but the agreement is considered good because the flaw sizes used were inferred from tests on other specimens and hence were very approximate. The results from this study indicate that fracture mechanics can be a valuable technique for predicting fracture of graphite under complex stress states, with the method being especially useful where regions of high stress concentration exist.

The third series of tests were on thin-walled tubes with axial and/or circumferential slits machined through the wall and tested under biaxial stresses with a ratio of circumferential to axial stress of either 2:1 or 1:-1 (ref. 47). The pressures and loads required to fracture the thin-walled tubes with slits machined through the walls to simulate cracks were estimated using linear elastic fracture mechanics. The estimates were in agreement with the experimental results in a gross sense, but the large scatter in the data precluded obtaining a definitive evaluation.

**Statistical models based on fracture mechanics**

Buch[48] had considerable success in predicting the uniaxial tensile strength of a wide range of commercially available graphites using a model that considered graphite to consist of discrete particles, each with an easy cleavage direction. Under appropriate loading these cracked particles were allowed to link up to form a crack of critical length according to LEFM. Rose and Tucker[49] extended Buch's model beyond the tensile test to the nonuniform stress states found in three- and four-point bend tests and compared the predictions of the model with experimental observations. They concluded:

1. The model correctly predicts the variation of failure probability with applied load in three- and four-point bend for both wide and narrow knife edge spacings.
2. The theoretical dependence of three- and four-point bend strength on knife edge spacing is in close agreement with that observed experimentally.
3. The calculated value of the tensile-to-bend strength ratio is some 21% greater than that observed.

4. The success of the model in predicting the fracture behavior under a variety of loading conditions indicates that it is applicable to other more general but not dissimilar states of stress.

5. Because the model is based on linear elastic fracture mechanics its extension to situations of stress intensification at sharp notches appears to be possible.

6. The simplicity of the model, though open to criticism on physical grounds, renders it suitable for incorporation in engineering stress analysis calculations.

**Phenomenological failure criteria**

Whereas the statistical and fracture mechanics failure criteria are developed on the basis of some theory about the physical process that causes failure, the phenomenological failure theories basically amount to fitting a surface in stress space to the available data. Although the concept is simple, it can be complex in detail since there are three normal stresses and three shearing stresses. This means that in the most general case one is talking about a surface in six-dimensional stress-space. If the material is isotropic any stress state can be resolved into the principal stress components so that one must only be concerned with the normal stresses. However, for a general anisotropic material, all six stress components must be considered except when the principal stress directions coincide with the symmetry directions of the material. Adding to the complexity is the transversely isotropic nature of most graphites and different strengths in tension and compression.

Failure theories discussed in the general literature[50] usually assume that the material is isotropic and has the same strength in tension and compression. Because graphite is about three times stronger in compression than in tension and is often transversely isotropic, even the standard theories of failure must be modified to take these considerations into account.

The simplest failure criterion is the maximum stress criterion, which considers the maximum or minimum principal stress as the criterion for strength. Failure is assumed to occur either when the maximum principal stress reaches the tensile strength of the material or the minimum

principal stress reaches the compressive strength. For a transversely isotropic material there are different tensile and compressive strengths in the plane of isotropy and perpendicular to it, so that even this simple theory requires four constants. It is also necessary to know how to treat the situation where the direction of the principal stresses do not correspond with the material axes, i.e., the shear strengths must be known. The maximum stress theory is used in the ASME Code Subsection CE (ref. 6).

The maximum strain theory has been used in the aerospace industry[51] as a failure criterion for graphite. It has an inherent advantage for the High Temperature Reactor Program since the highest stresses are irradiation induced and the strains can generally be predicted more accurately than the stresses. The maximum strain theory is analogous to the maximum stress theory, except in this case it is assumed that failure occurs either if the maximum principal strain equals the fracture strain in simple tension or the minimum principal strain equals the fracture strain in simple compression.

The Mohr theory is similar to the maximum shear theory that is often used for metals, except that it allows for a different tensile and compressive strength. Other failure theories that have been considered for graphite include the maximum strain energy theory[52] and Chamis' empirical fracture criterion.[53] Several authors[3,54-57] have concluded that the Tsai-Wu[58] theory is the recommended multiaxial fracture criterion for graphite. The Tsai-Wu theory is a general strength criterion for anisotropic materials that was developed from a scalar function of two strength tensors. A distinct advantage of this theory is that it satisfies the invariant requirements of coordination transformation, which simplifies its use in conjunction with general finite-element computer codes. The general form of the Tsai-Wu theory is

$$F_i\sigma_i + F_{ij}\sigma_{ij} = 1 \tag{14}$$

in contracted notation with $i,j = 1,2,\ldots 6$ where $\sigma$ is the stress tensor of rank two and $F_i$ and $F_{ij}$ are strength tensors of rank two and four, respectively. $F_{ij}$ is required to be positive definite in order to ensure that the surface is closed, which avoids the possibility that infinite strength might be predicted for some stress state. Taking advantage of the symmetry of a transversely isotropic material, the strength tensors are

$$F_i = \begin{bmatrix} F_1 \\ F_2 \\ F_3 \\ 0 \\ 0 \\ 0 \end{bmatrix} \tag{15}$$

and

$$F_{ij} = \begin{bmatrix} F_{11} & F_{12} & F_{13} & 0 & 0 & 0 \\ F_{12} & F_{11} & F_{13} & 0 & 0 & 0 \\ F_{13} & F_{13} & F_{33} & 0 & 0 & 0 \\ 0 & 0 & 0 & F_{44} & 0 & 0 \\ 0 & 0 & 0 & 0 & F_{44} & 0 \\ 0 & 0 & 0 & 0 & 0 & 2(F_{11} - F_{12}) \end{bmatrix} . \tag{16}$$

Substituting Eqs. (15) and (16) into Eq. (14) one obtains the fracture criterion for a transversely isotropic material

$$F_1(\sigma_1 + \sigma_2) + F_3\ \sigma_3 + F_{11}(\sigma_1^2 + \sigma_2^2 + s\sigma_6^2) + F_{33}\ \sigma_{33}^2 + F_{44}(\sigma_4^2 + \sigma_5^2)$$
$$+ 2F_{12}(\sigma_1\sigma_2 - \sigma_6^2) + 2F_{13}(\sigma_1\sigma_3 + \sigma_2\sigma_3) = 1 , \tag{17}$$

where $\sigma_1$, $\sigma_2$, and $\sigma_3$ are normal stresses, $\sigma_4$, $\sigma_5$, and $\sigma_6$ are shear stresses, and the $F$'s are seven constants. These constants must be obtained from strength tests on the graphite of interest. Tang[55] suggested that the seven constants be determined from four uniaxial tests (tension and compression in the with-grain and across-grain directions), a biaxial test on a thin-walled tubular specimen, a triaxial test where a rod is laterally confined by a hydrostatic pressure and subjected to axial tension (Bridgeman test), and a torsion test on a thin-walled tubular specimen. It is obvious that a large number of tests will be required just to establish these data points and their variability. Knowing the variability of these seven points on the failure surface does not establish the probability of failure at any other point. Therefore, it will be difficult to quantify failure probabilities for general multiaxial stress states.

#### 7.3.1.3 Multiaxial Failure Data for Graphites

The test of any multiaxial failure theory is how well it compares with multiaxial test data. Failure data from statically determinate tests are most useful for testing failure criteria because the stress at failure can be determined without using the constitutive equations. A

number of investigators have run failure tests on thin-walled tubes. Some investigators[59] have concentrated on the tension-tension quadrant. Many investigators[19,52,60-66] have run tests where the axial stress was compressive to obtain data in the tension-compression quadrant as well as in the tension-tension quadrant.

Data from thin-walled tube tests[47] on RAXM graphite* are compared with several of the multiaxial stress theories in Fig. 7.7. Difficulties are often encountered with buckling when high compressive loads are applied to the thin-wall tubes. Therefore, although several investigators[67-76] have tried to obtain failure data in the compressive-compressive quadrant,

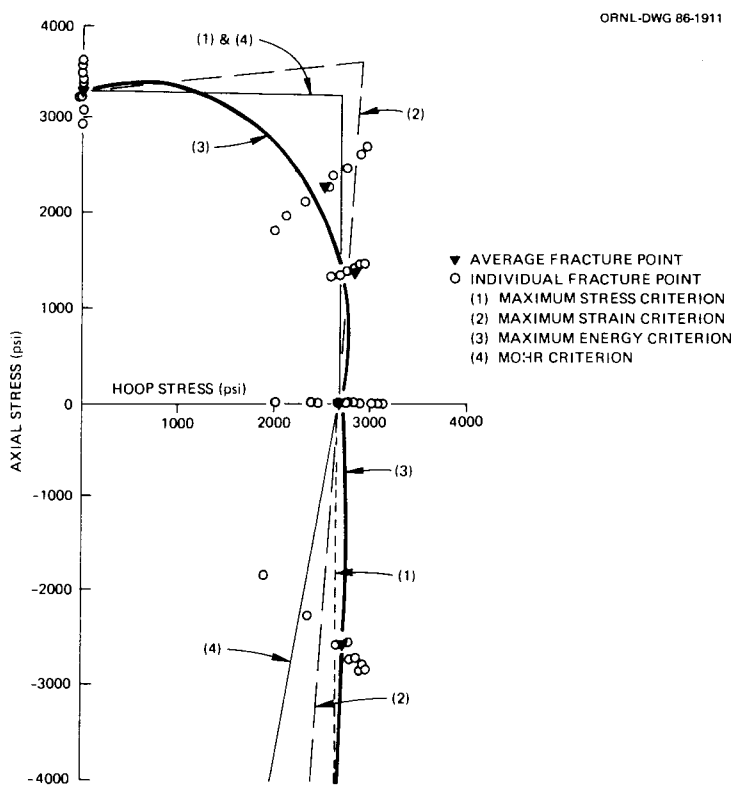


Fig. 7.7. Comparison of fracture data from RAXM thin-walled tubes with theories of failure.

*RAXM is a special extruded graphite that was made under the NERVA program.

premature failure due to buckling has usually been suspected. Recent tests by Hackerott[57] in the compression-compression quadrant appear to have minimized premature failure due to buckling.

Unfortunately buckling is not the only problem experienced with thin-walled tube tests. Although the stresses are very nearly statically determinate in a thin-walled tube, the ends of the specimens are usually thicker than the gage section, which results in discontinuing stresses. Although careful design can minimize this discontinuity, it can never be totally eliminated.

Although a large number of biaxial tests have been run, there have not been enough duplicate tests to establish the statistical behavior under multiaxial stress conditions. If one looks at "good" data in all four quadrants of biaxial stress space, the best fit to the "average" of all the data is produced by the Tsai-Wu theory as in Fig. 7.8. However,

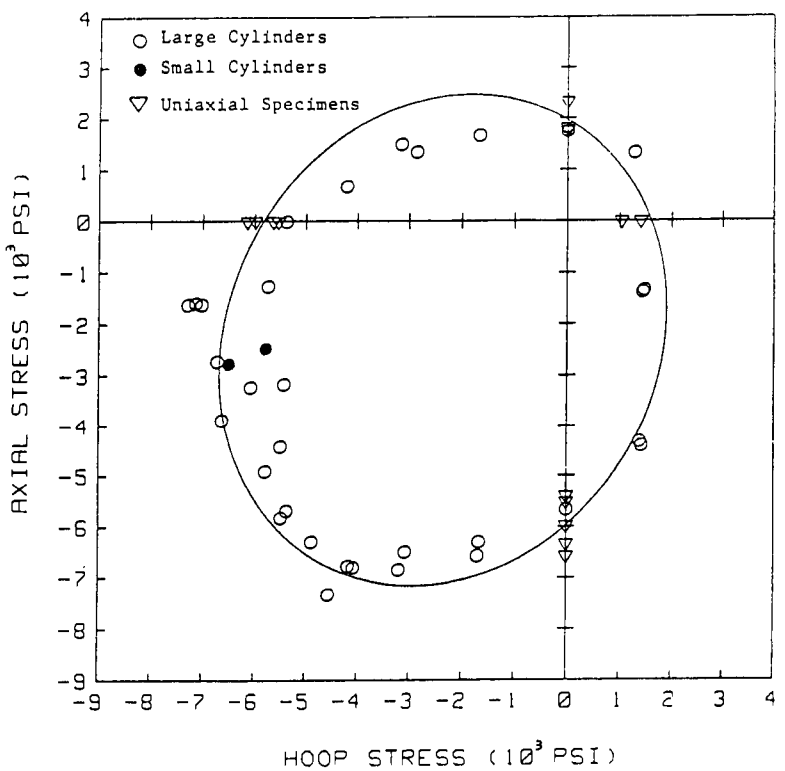


Fig. 7.8. Tsai-Wu failure criterion compared with biaxial failure data for AGOT graphite. *Source*: H. A. Hackerott, "Characterization of Multiaxial Fracture Strength of Transversely Isotropic AGOT Graphite," M.S. thesis, Kansas State University, Manhattan, 1982.

the compressive strength of graphite is 3 or 4 times the tensile strength. Failures in the core of an HTR would always occur under biaxial tension or under tension-compression where the compression is less than or equal to the tension because the high stresses are a result of either thermal stresses or irradiation-induced stresses. When one restricts his consideration to this area of the biaxial stress space, no one multiaxial theory exhibits a greatly superior fit to the available data in this region. For example, for equibiaxial tension the maximum stress theory overpredicts the strength, whereas the Tsai-Wu theory underpredicts the strength.

In the paragraph above we considered the relative fit of multiaxial failure theories to the average data from biaxial tests. However, for the design of HTR graphite core components we are interested in the precluding failure; therefore, we are most interested in the best fit to the lower bound of the failure data. Jortner[73] decided in 1971 that the lower bound of biaxial tube data on ATJ-S fitted the maximum principal stress criterion quite well.

Biaxial tests on thin-walled graphite tubes provide good data for comparing the relative merits of the phenomenological failure criteria. However, more prototypic test data are required to evaluate the relative merits of both the mechanistic and phenomenological theories. Analysis of the more prototypic tests requires the use of constitutive equations to determine the stresses and strains. More prototypic tests were run on splitting tensile specimens[45] and flat-headed thick-walled pressure vessels.[46] Good failure predictions were achieved for both tests using linear elastic fracture mechanics when machined flaws were introduced into the specimens. Promising results were achieved on the specimen without machined flaws, but there was an indication that the linear elastic fracture mechanics approach needed additional investigation.

A considerable amount of work was done under sponsorship of the Air Force Materials Laboratory (AFML) to develop design methods for application to graphite nosetips for re-entry vehicles. Just as with the HTGR core, thermal stresses play a key role in nosetips for re-entry vehicles. Therefore, instrumented thermal stress tests were developed at TRW[77-79] and Southern Research Institute[80] that could be used as a proof test for

design methods. Instrumented graphite nosecones were tested under realistic conditions[51] in the Air Force Flight Dynamic Laboratory 50-MW facility. Deformations were monitored in the AFML tests. Comparisons of elastic analyses and elastic-plastic analyses using different constitutive equations showed that similar strain predictions were obtained regardless of the constitutive equations used. Predicted deformations were in reasonable agreement with measured deformations. Stress predictions were found to vary considerably depending on the constitutive equations used. The maximum strain theory of failure was used and found to be in reasonable agreement with the data.[51] Plasticity analysis of a thermal shock test that was developed at ORNL[81] in 1965 and the maximum stress theory of failure gave reasonable agreement with the data also.[82]

#### 7.3.1.4 Recommendations

Although the Tsai-Wu theory gives the best correlation of the biaxial test data when data for the compression-compression quadrant are included along with data from the tension-tension and tension-compression regions, we do not recommend it for use as a multiaxial failure for HTR use. If a phenomenological multiaxial stress criterion is to be used, the maximum stress criterion does almost as good a job in the multiaxial stress regions of interest. Because of the inherent variability of graphite strength, the increased accuracy that can be achieved using the Tsai-Wu criterion will not appreciably increase the overall accuracy that can be achieved. The Tsai-Wu criterion would require development of new test methods and would require much more testing than the maximum stress criterion.

Experience to date indicates that the fracture mechanics approach has the best potential as the fracture criterion for use in HTR graphite design. It has been shown to give good failure predictions under diverse states of stress when machined flaws are present. Considerably more work is needed to establish it as the fracture criterion for HTR design, but it has many potential advantages.

For example, it is reasonable to suggest that it can account for the size effects that have been observed in graphite. Larger volumes should

be expected to have a greater chance of having a large initial flaw. Therefore, the larger volume would have a lower strength predicted by fracture mechanics.

Another advantage of fracture mechanics is that it would lead naturally to calculation of flaw growth under both monotonic and cyclic loading. Thus, in some cases, it might be possible to show that although a crack might initiate, it would not reduce the structural adequacy of that part. Fracture mechanics also provides a realistic way of computing fatigue damage in graphite.

It is recommended that the use of fracture mechanics be more fully investigated for use as the fracture criterion for HTGR graphite components. In particular the following investigations are needed:

1. Investigate techniques for using fracture mechanics in conjunction with existing analysis tools.
2. Investigate the flaw size that should be assumed to exist. Statistics should be used in this step so that this method fits naturally with the statistical approach selected for design of HTGR graphite components. This will also allow a natural introduction of a "size effect" into this approach.

The existing data from thermal stress tests and failure data from Fort St. Vrain should be used to benchmark the complete design process including constitutive equations and failure models.

### 7.3.2 Statistical Treatment of the H451 Tensile Strength Data Base – W. P. Eatherly

#### 7.3.2.1 Introduction

Flaws in bulk graphite determine the tensile or flexural strength and may be broadly classed as either background or disparate. The background flaws are inherent in the material and generally comparable to the grain size, whereas the disparate flaws are introduced during forming and heat treatment and can be quite large. In aerospace graphites with their small billet and grain size, sonic attenuation characterizes the omnipresent background flaws, while sonic reflection readily detects disparate flaws.[83]

For nuclear and, indeed, most structural graphites the large billet and grain size generally preclude sonic techniques for flaw identification and location. This study assumed that nuclear graphites would possess the same flaw characteristics as aerospace graphites, a bimodal distribution of strengths representing a normal distribution with a low-strength tail attributable to the disparate flaws. This is hardly an assumption, as even a superficial look at the microstructure will substantiate. The statistical problem then becomes the identification and characterization of these two components of the total distribution of strengths. The purpose of this work is not to develop acceptance/rejection criteria, although such are readily obtainable from the results given here.

Data[84] available for study consisted of three production runs of Great Lakes graphite grade H451, representing 14, 56, and 28 billets. From the center of each billet, sets of tensile samples were obtained in both the radial and axial directions with cylindrical stress volumes defined by diameters of 6.35 mm and lengths of 23 mm. The data we analyze here are for the axial strengths only and consist of a nominal sampling of eight specimens for each billet.

### 7.3.2.2 Mathematical Details

We assume in this section the reader's familiarity with the general statistical principles involved. For those not concerned, the results are summarized in the concluding section below.

The results of the provisional variance analysis for the three lots of graphite are given in the first part of Table 7.5. The two statistical parameters[85] characterizing the distributions are $s_W^2$ and $\hat{\theta}$:

$$E(s_W^2) = \sigma_W^2 , \qquad E(\hat{\theta}) = \theta = \sigma_b^2/\sigma_W^2 .$$

The degrees of freedom for the mean sum of squares for $\sigma_W^2$ is $\nu_1$ and for the remainder of the partitioned sum (Sheffé's $MS_A$) is $\nu_2$. Also given are the mean strengths $m$ for the lots.

Two tests for homogeneity were considered, the Bartlett test in its $\chi^2$ form and the Foster Q-test.[86] The latter test was rejected because of its lack of sensitivity to large values of $s_i^2$ unless these are far off

Table 7.5. One-way variance analyses and homogeneity tests before and after truncation

| | Full distributions | | | Truncated distributions | | |
|---|---|---|---|---|---|---|
| Lot: | 472 | 478 | 482 | 472 | 478 | 482 |
| $m$, MPa | 12.2 | 13.6 | 11.1 | 12.2 | 13.8 | 10.8 |
| psi | 1779 | 1979 | 1615 | 1771 | 2013 | 1570 |
| $s_W$, MPa | 1.42 | 1.70 | 1.57 | 1.07 | 1.46 | 1.43 |
| psi | 207 | 247 | 228 | 156 | 213 | 208 |
| $\hat{\theta}$ | 3.29 | 1.62 | 1.98 | 5.52 | 2.30 | 2.51 |
| $\nu_1$ | 13 | 55 | 27 | 12 | 51 | 26 |
| $\nu_2$ | 98 | 392 | 196 | 91 | 364 | 189 |
| $K$ | 37.5 | 108.7 | 37.6 | 15.0 | 68.0 | 28.9 |
| $\chi^2$ $(\nu_1)$ | 22.4 | 73.3 | 40.1 | 21.0 | 68.7 | 38.9 |
| $\Gamma$ | 0.127 | 0.027 | 0.049 | 0.099 | 0.025 | 0.050 |
| $\gamma(n_1,n_2)$ | 0.103 | 0.024 | 0.049 | 0.112 | 0.027 | 0.050 |

the expected $\chi^2$-distribution. This flaw appears inherent to the Q-test. The criterion for homogeneity in the Bartlett test is that the observed statistic $K$ be less than the upper $\alpha$th critical point for the $\chi^2$ distribution, and in the Foster test that the observed statistic $Q$ be less than the $\alpha$th critical point of the $q$-distribution. The reader is referred to ref. 86 for the forms of $K$ and $Q$. We elected to use $\alpha = 0.85$ for the critical point. Clearly, the complete data sets do not satisfy either criterion for graphite lots 472 and 478, and that for lot 482 does so only marginally.

Data "rejection" was accomplished on the basis of Nair and Studentized Range tests,[87] the one to test for low-lying outliers and the other for kurtosis. We also used the common restriction for small data sets: if the within-billet data subset required removal of more than one datum, the entire subset was rejected. The choice of risk ($\alpha$) for these criteria is somewhat arbitrary, since the underlying distribution of flaws must be continuous and the dichotomization into disparate and background flaws is itself arbitrary. The choices $\alpha = 0.05$ for the Nair and 0.10 for the Range test were sufficient to obtain variance homogeneity. The number of "rejected" data points and subsets are given in Table 7.6.

Table 7.6. Rejection of data to achieve homogeneity

| Lot | Single datum (outlier) | Entire billet (outliers) | 8 Data (range) |
|---|---|---|---|
| 472 | 3 | 0 | 1 |
| 478 | 7 | 3 | 1 |
| 482 | 3 | 0 | 1 |

The results of the variance analysis and the homogeneity tests are given in the second part of Table 7.5 for the truncated distributions. Partially filled cells (i.e., billets for which less than eight specimens were available) were treated as "filled" by leaving the mean and variance unchanged but increasing the degrees of freedom arbitrarily. By $t$-test on the means and $F$-test on $\hat{\theta}$, the three lots are different.

The rejected data, to the extent they contained low outliers whether isolated or from rejected subsets, were now taken to represent specimens with disparate flaws. For brevity, we consider only the collective results from all three lots. For the specimen volume employed, the probability of occurrence of a disparate flaw is 3.4% (26 flawed specimens from a total population of 774). Binomial analysis indicated a slight correlation effect, that is, a tendency to find multiple disparates within a billet.

The strengths of the 26 disparate specimens were normally distributed, a not entirely surprising result in that they were identified by their distance from the normally distributed billet means. The parameters are given in Table 7.7. The moment correlation coefficient $R$ is that for strength deficiency versus argument of the cumulative normal distribution function using the formula $\Phi = (8i - 3)/(8n + 5)$ for the sample cumulative. Here, $R$ has no statistical significance but is presented only to indicate the excellent linearity of the cumulative plot. In fact, this and all other distributions in the analysis were tested for goodness-of-fit by the Kolmogorov-Smirnov test at $\gamma = 0.95$. All truncated distributions satisfied this condition.

Table 7.7. Parameterization of disparates

| | |
|---|---|
| Distance, mean below billet mean | 5.3 MPa (768 psi) |
| Standard deviation | 0.92 MPa (133 psi) |
| Correlation coefficient | 0.9931 |

The distributions were slightly platykurtic to begin with, and, although truncation removed the skewness, it also increased the kurtosis. For purposes of establishing tolerance limits, however, this will lead to a conservative prediction.

#### 7.3.2.3 Conclusions

We may now summarize our results by stating that the distribution of strengths for a production lot may be characterized by three normal distributions. The numerical values for the parameters involved will, of course, be mildly affected by the specimen stress volume. The three distributions are those for (1) the billet mean strength with inherent variability given by the standard deviation (see the second part of Table 7.5)

$$s_b = \sqrt{\hat{\theta}}\, s_w \;;$$

(2) the variability within a billet given by the standard deviation $s_w$ (Table 7.5); and (3) an additional distribution due to disparate flaws with mean lying 5.3 MPa (768 psi) below the billet mean, standard deviation 0.92 MPa (133 psi), and occurring for 3.4% of the specimens (Table 7.7). One obviously does not reject high-strength billets because of disparates. Rather, the low-strength billets must be rejected at a higher tolerance level.

Unfortunately, the specimens used here were destroyed before this analysis was performed. It is now impossible to verify that the specimens identified here did indeed contain large flaws, but any other explanation would be forced. If our experience with aerospace graphites can be used as a guide, we would expect that about 70% or more of the fracture surfaces would contain an identifiable disparate flaw.[88]

### 7.3.3 Modeling the Statistics – W. P. Eatherly

It is relatively rare in statistics that a situation exists where the statistical distribution is known *ab initio* and nonconformance of the data to the statistic can be attributed to a faulty experiment. Obvious and somewhat trivial examples of known distributions arise in throwing dice or drawing cards. The overwhelming practical situation is that a data base comes into existence, an underlying distribution is hypothesized, and goodness-of-fit tests are employed to reach a decision as to whether the choice of underlying distribution is appropriate. Quite clearly, additional data or new types of experiments may prove the initial choice of underlying distribution to be inappropriate or incomplete. Only when massive numbers of data points exist and only when they are taken under a variety of conditions can we begin to say with confidence that the underlying distribution functions are known. We wish now to consider what inferences can be drawn from the above data set.

#### 7.3.3.1 The Background Flaw Field

We first appeal to another data set[89] beyond that treated by the variance analysis. In a carefully constructed experiment, Kennedy sought to establish the Weibull character of the H451 tensile strengths. For this purpose a density correction is required.

Over a number of commercial graphites spanning the range of fine-grained specialty materials to extremely coarse-grained electrode stock, there has been shown to exist a strong correlation between strength and density for specimens within a given billet. This is normally expressed in the form of a Knudsen equation, viz,

$$\sigma = \sigma_0 \exp \alpha(\rho - \rho_0) \ ,$$

where $\sigma_0$ is the ultimate strength at density $\rho_0$ and $\sigma$ is the strength at density $\rho$. If one is concerned with establishing the Weibull character of the strength, then the variability due to density must first be removed.

The establishment of Weibull statistics in their usual formulation requires the validation of two relations. The first is the relationship between variance $\sigma^2$ and mean $\mu$ at any volume, given by the coefficient of variation (COV)

$$\mathrm{COV} = \frac{\sigma}{\mu} = \frac{\Gamma(1 + \frac{2}{m}) - \Gamma^2(1 + \frac{1}{m})}{\Gamma(1 + \frac{1}{m})} ,$$

where $m$ is the Weibull exponent. The second relationship is

$$\frac{\mu(V_1)}{\mu(V_2)} = \left(\frac{V_2}{V_1}\right)^{1/m}$$

and defines the shift of mean value with volume $V$ the "weakest-link" effect. (We assume that the background flaws affect the specimen through stress volume rather than area.) It is the COV relationship which is clearly sensitive to the density correlation through the total variance $\sigma^2$ rather than the desired variance due to Weibull effects alone. Upon correction, Kennedy demonstrated that both these relations are satisfied with $m \cong 7$.

This result raises two questions: In the variance analysis and its bimodality, we assumed normal distributions; how can this be valid if even one of the modes is Weibull? If disparates truly exist, why do not they mask the Weibull? We answer the first question positively in that the density correlation, if not removed by correction to a reference density, will mask the Weibull. Unfortunately, this cannot be demonstrated conclusively for our large data set since specimen densities were not measured. We answer the second question positively in that over some three decades in which the volume effects were sought, the specimens were smaller or comparable to those used in the large data set. Hence, the chances of finding a disparate flaw were small or negligible.

We thus accept the conclusion that the underlying distribution for the background flaws is Weibull with exponent about 7 unless further data implies otherwise.

#### 7.3.3.2 The Disparate Flaws

To establish the distribution for the disparate flaws, we have no recourse except hypotheses – no specific relevant data exist. We shall construct a model based on two assumptions:

1. Defining a base cell volume $\tau$ as sufficient to contain either one disparate flaw or none. Then the number of disparate flaws contained in an arbitrary larger volume $V$ is binomially distributed over $\tau$.

2. If the arbitrary volume $V$ contains $N$ volumes $\tau$, then the largest flaw on the average will be the lowest (first) order statistic for an $N$-fold sampling of a normal distribution. (At this point we continue to assume that the normal distributions first on the variance analysis of the large data base are valid.)

We will not concern ourselves with the mathematics but will proceed directly to the conclusions, and these are almost totally dominated by assumption 1. As the stress volume of the specimen increases, the number of specimens containing no flaws rapidly decreases, and we increasingly sample only the disparate mode. The large data base represents specimens of stress volume 728 $mm^3$. If we increase the volume by a factor of 20 (say 17.2-mm diam by 68.4-mm length), then the fraction of specimens containing one or more disparate flaws increases from 3.4% to about 51%. Taking our large data base to have a mean tensile strength of 12.4 MPa (1800 psi), if no disparate flaw existed, the result of increasing the specimen size twentyfold with disparates reduces the mean strength to 9.6 MPa (1390 psi). Of this reduction, 96% is due to the increased number of specimens with disparate flaws, and only about 4% due to the fact that some of the specimens contained more than one flaw.

These results are, of course, easily generalized since they are a product distribution of the binomial and order statistics. We are led to the conclusion that the existence of a bimodal distribution with this type of model leads to extremely rapid strength reductions as the uniaxial stress volume increases. We do not as yet have the data base to test this model.

## 7.4 REFERENCES

1. J. E. Brocklehurst, "Fracture in Polycrystalline Graphite," *Chem. Phys. Carbon* **13**, 145-279 (1977).

2. V. Svalbonas, T. Stilwell, and Z. Zudans, *Evaluation of the Structural Integrity of High-Temperature Gas-Cooled Reactor (HTGR) Core and Support Elements*, FIRL Report F-C4230, Franklin Institute Research Laboratories, Philadelphia, April 1976.

3. V. Svalbonas, T. C. Stilwell, and Z. Zudans, "Rules for Design of Nuclear Graphite Core Components — Some Considerations and Approaches," *Nucl. Eng. Des.* **46**, 313–33 (1978).

4. G. J. DeSalvo and J. J. Lombardo, "NERVA Design Criteria and Application for Brittle Materials," pp. 619–40 in *Proceedings of the Conference on Continuum Aspects of Graphite Design, November 9–12, 1970, Gatlinburg, Tennessee*, ed. W. L. Greenstreet and G. C. Battle, Jr., CONF-701105, available from National Technical Information Service, Springfield, Va., February 1972.

5. G. T. Yahr and D. G. O'Connor, *Structural Design Criteria and Design Data for AVLIS Graphite Components*, ORNL/TM-9699, September 1985.

6. *ASME Boiler and Pressure Vessel Code, Section III, Nuclear Power Plant Components, Division 2, Subsection CE, Design Requirements for Graphite Core Supports*, to be published by the American Society of Mechanical Engineers, New York.

7. M. J. Manjoine and R. E. Tome, "Proposed Design Criteria for High Cycle Fatigue of Austenitic Stainless Steel," in *ASME International Conference on Advances in Life Prediction Methods, Albany, New York, April 18–20, 1983*, American Society of Mechanical Engineers, New York, 1983.

8. *ASME Boiler and Pressure Vessel Code, Section III, Rules for Construction of Nuclear Power Plant Components, Division 1 — Appendices*, American Society of Mechanical Engineers, New York, 1983.

9. W. R. Johnson and G. B. Engle, *Properties of Unirradiated Fuel Element Graphites H-451 and TS-1240*, GA-A13752, General Atomic Company, San Diego, Jan. 31, 1976.

10. M. G. Natrella, *Experimental Statistics*, National Bureau of Standards Handbook 9, U.S. Government Printing Office, Washington, D.C., 1963, p. T-15.

11. S. E. Moore, "Theoretical and Experimental Investigation of the Applicability of Weibull's Statistical Theory of Strength to EGCR-Type AGOT Graphite Fracture Data," pp. 216–25 in *Gas-Cooled Reactor Project Semiannual Progress Report for Period Ending September 30, 1965*, ORNL-3885, February 1966.

12. I. B. Mason, "The Strength of Commercial Graphite," pp. 597–610 in *Proceedings of the Fifth Carbon Conference, Volume II*, Pergamon, New York, 1963.

13. C. D. Pears and H. S. Starrett, *An Experimental Study of the Weibull Volume Theory*, AFML-TR-66-228, Air Force Materials Laboratory, Wright-Patterson Air Force Base, Ohio, March 1967.

14. R. Stevens and T. D. Clausen, *Strength Distribution and Fracture Behavior of Structural Ceramics of Low Neutron Absorption Cross Section*, AECL-3422, Atomic Energy of Canada Limited, Pinawa, Manitoba, October 1969.

15. Ernest Robinson, *Some Problems in the Estimation and Application of Weibull Statistics*, UCRL-70555, University of California Lawrence Radiation Laboratory, Livermore, Calif., Sept. 1, 1967.

16. H. L. Leichter and E. Robinson, "Fatigue Behavior of a High-Density Graphite and General Design Correlation," *J. Am. Ceram. Soc.* **53**(4), 197–204 (April 1970).

17. R. J. Price and H. R. W. Cobb, "Application of Weibull Statistical Theory to the Strength of Reactor Graphite," pp. 547–67 in *Proceedings of the Conference on Continuum Aspects of Graphite Design, November 9–12, 1970, Gatlinburg, Tennessee*, ed. W. L. Greenstreet and G. C. Battle, Jr., CONF-701105, available from National Technical Information Service, Springfield, Va., February 1972.

18. V. Lungagnani and R. Krefeld, "Statistical Considerations on the Strength of Nuclear Graphites: Characterization, Irradiation, and Design," pp. 663–75 in *Proceedings of the Conference on Continuum Aspects of Graphite Design, November 9–12, 1970, Gatlinburg, Tennessee*, ed. W. L. Greenstreet and G. C. Battle, Jr., CONF-701105, available from National Technical Information Service, Springfield, Va., February 1972.

19. W. L. Greenstreet, G. T. Yahr, and R. S. Valachovic, *Fracture of Graphite, Quarterly Progress Report No. 9, for Period Ending January 1, 1972*, ORNL-TM-3874, August 1972.

20. W. Weibull, "A Statistical Theory of the Strength of Materials," *Ingeniorvetenskapsakademiens*, Handlingar NR 153, Stockholm, 1939.

21. E. Y. Robinson, *The Statistical Nature of Fracture*, UCRL-50622, University of California Lawrence Radiation Laboratory, Livermore, Calif., Mar. 30, 1969.

22. A. M. Freudenthal, "Statistical Approach to Brittle Fracture," pp. 591–619 in *Fracture – An Advanced Treatise, Vol. II: Mathematical Fundamentals*, Academic, New York, 1968.

23. C. R. Kennedy, "Strength Loss and Other Related Physical Property Data," pp. 18–23 in *High-Temperature Gas-Cooled Reactor Base-Technology Program Annual Progress Report for Period Ending December 31, 1979*, ORNL-5643, July 1980.

24. W. P. Eatherly, "Statistical Identification of Disparate Flaws in H451 Graphite," pp. 532–33 in *15th Biennial Conference on Carbon, Extended Abstracts and Program, June 22-23, 1981*, The University of Pennsylvania, Philadelphia, June 1981.

25. W. P. Eatherly, *Failure Criteria for Graphites: A First Statistical Model for the Effects of Disparate Flaws* (to be published).

26. G. M. Jenkins, "Fracture in Reactor Graphite," *J. Nucl. Mater.* **5**, 280–86 (1961).

27. O. D. Slagle, "Deformation Mechanisms in Polycrystalline Graphite," *J. Am. Ceram. Soc.* **50**, 495–500 (1967).

28. R. Stevens, "Fracture Behavior and Electron Microscopy of a Fine Grained Graphite," *Carbon* **9**, 573–78 (1971).

29. A. M. Hasofer, "A Statistical Theory of the Brittle Fracture of Steel," *Int. J. Fracture Mech.* **4**, 439–51 (1968).

30. F. H. Ho, "Modified Weibull Theory and Stress Concentration Factors of Polycrystalline Graphite," pp. 524–25 in *15th Biennial Conference on Carbon, Extended Abstracts*, The University of Pennsylvania, Philadelphia, June 1981.

31. S. B. Batdorf, "Fracture Statistics of Polyaxial Stress States," pp. 579–91 in *Fracture Mechanics*, ed. N. Perrone, H. Liebowitz, D. Mulville, and W. Pilkey, University Press of Virginia, Charlottesville, 1978.

32. S. B. Batdorf and H. L. Heinisch, Jr., "Weakest Link Theory Reformulated for Arbitrary Fracture Criterion," *J. Am. Ceram. Soc* **61**(7–8), 355–58 (1978).

33. J. M. Corum, "A Determination of the Fracture Toughness of EGCR-Type AGOT Graphite," *J. Nucl. Mater.* **22**, 41 (1967).

34. L. O. Slind, R. G. Hoagland, and R. G. Rowe, *The Fracture Toughness of Graphite Double Cantilevered Beam Specimens*, Battelle-Northwest Report BNWL-CC-774, Battelle-Northwest Laboratory, Richland, Wash., 1966.

35. K. G. Nolte, *An Introductory Analysis of Graphite Fracture* (unpublished report), Los Alamos Scientific Laboratory, Los Alamos, New Mex., 1966.

36. R. W. Davidge and G. Tappin, "The Effective Surface Energy of Brittle Materials," *J. Mater. Sci.* **3**, 165 (1968).

37. I. D. Peggs, *Carbon, Graphite, and Some Carbides for Superheat Service: Literature Survey*, Report AECL-3069, Atomic Energy of Canada Limited, Pinawa, Manitoba, 1968.

38. R. E. Johnson, "The Influence of the System Geometry on Fracture Toughness," Ph.D. thesis, Carnegie Institute of Technology, Pittsburgh, 1965.

39. G. T. Yahr, R. S. Valachovic, and W. L. Greenstreet, "Application of Fracture Mechanics to Graphite," p. 223 in *Summary of Papers, 10th Biennial Conference on Carbon*, Defense Ceramic Information Center, Battelle Memorial Institute, Columbus, Ohio, 1971.

40. R. H. Knibbs, "Fracture in Polycrystalline Graphite," *J. Nucl. Mater.* **24**, 174 (1967).

41. E. P. Kennedy and C. R. Kennedy, "Dependence of Strength on Particle Size in Graphite," pp. 303–315 in *Fracture Mechanics: Thirteenth Conference*, ASTM STP 743, ed. Richard Roberts, American Society for Testing and Materials, Philadelphia, 1981.

42. G. T. Yahr and R. S. Valachovic, "Geometrical Parameters Affecting the Fracture Toughness of Graphite," pp. 533–46 in *Proceedings of the Conference on Continuum Aspects of Graphite Design, November 9–12, 1970, Gatlinburg, Tennessee*, ed. W. L. Greenstreet and G. C. Battle, Jr., CONF-701105, available from National Technical Information Service, Springfield, Va., February 1972.

43. C. R. Kennedy and M. T. Kehne, "Fracture Toughness of Anisotropic Graphite," pp. 289–90 in *17th Biennial Conference on Carbon, Extended Abstracts and Program*, University of Kentucky, Lexington, Ky., 1985.

44. W. L. Greenstreet, unpublished data, Jan. 1, 1971.

45. G. T. Yahr, R. S. Valachovic, and W. L. Greenstreet, "An Examination of Fracture Behavior of Graphite Through the Use of Splitting Tensile Tests," pp. 29–46 in *Graphite Structures for Nuclear Reactors, Proceedings of International Conference, London, England, March 1972*, Institute of Mechanical Engineers, London, 1972.

46. G. T. Yahr and R. S. Valachovic, "Application of Fracture Mechanics to Graphite Under Complex Stress Conditions," in *Fracture Mechanics of Ceramics, Vol. 2*, ed. R. C. Bradt, D. P. H. Hasselman, and F. F. Lange, Plenum Publishing Corporation, New York, 1973.

47. W. L. Greenstreet, G. T. Yahr, and R. S. Valachovic, *Fracture of Graphite, Quarterly Progress Report No. 10 for Period Ending April 1, 1972*, ORNL/TM-3936, October 1972.

48. J. D. Buch, *Mechanical Behaviour Model for Graphites, Properties Related to Fracture Toughness*, ASTM STP 605, American Society for Testing and Materials, Philadelphia, 1976.

49. A. P. G. Rose and M. O. Tucker, "A Fracture Criterion for Nuclear Graphite," *J. Nucl. Mater.* **110**, 186–95 (1982).

50. S. Timoshenko, *Strength of Materials, Part II, Advanced Theory and Problems*, 3rd Edition, Van Nostand, Princeton, N.J., 1956, pp. 444–62.

51. D. L. Baker, H. S. Starrett, and C. L. Budde, *Thermostructural Testing of Instrumented ATJ-S Graphite Shell Nosetips in the AFFDL 50 MW Facility*, AFML-TR-76-26, Air Force Materials Laboratory, Wright-Patterson Air Force Base, Ohio, April 1976.

52. R. E. Ely, "Strength of Magnesium Silicate and Graphite Under Biaxial Stresses," *Ceram. Bull.* **47**(5), 489–92 (1968).

53. T. Weng, "Biaxial Fracture Strength and Mechanical Properties of Graphite-Base Refractory Composites," *AIAA J.* **7**(5), 851–58 (May 1969).

54. T. Y. Chang and T. Weng, "A Strength Criterion for Graphite Under Combined Stresses," ASME PVP Meeting, American Society of Mechanical Engineers, New York, June 1975.

55. P. Y. Tang, *A Recommendation of a Triaxial Failure Theory for Graphite*, GA-A15333, General Atomic Company, San Diego, Calif., May 1979.

56. G. J. DeSalvo, "Strength Theories and Effective Stress-Strain Laws Applicable to Graphite and Composites," Data Release Memorandum No. 54448, Westinghouse Astronuclear Laboratory, Large, Pa., Oct. 20, 1971.

57. H. A. Hackerott, "Characterization of Multiaxial Fracture Strength of Transversely Isotropic AGOT Graphite," M.S. thesis, Kansas State University, Manhattan, 1982.

58. S. W. Tsai and F. M. Wu, "A General Theory of Strength for Anisotropic Materials," *J. Compos. Mater.* **5**, 58-80 (January 1971).

59. J. G. Merkle, J. E. Smith, and F. J. Witt, "Failure Characteristics of EGCR-Type AGOT Graphite at Room Temperature," Abstract No. 137 of Papers Presented at the Seventh Conference on Carbon, *Carbon* **3**, 365 (1965); also see *Gas-Cooled Reactor Project Semiannual Progress Report for Period Ending September 30, 1965*, ORNL-3885, February 1966, pp. 231–35.

60. R. E. Ely, *Biaxial Fracture Stresses for Graphite, Ceramic and Filled and Reinforced Epoxy Tube Specimens*, RR-TR-65-10, U.S. Army Missiles Command, Redstone Arsenal, Ala., June 1965.

61. R. E. Ely, "Strength of Graphite Tube Specimens Under Combined Stresses," *J. Am. Ceram. Soc.* **48**(10), 505–08 (1965).

62. R. E. Ely, *Strength for Graphite and Two Types of Plastic Tubing Under Biaxial Stresses*, RR-TR-63-18, U.S. Army Missile Command, Redstone Arsenal, Ala., 1963.

63. J. Jortner, "Biaxial Mechanical Properties of AXF-5Q Graphite to 4000°F," *Proceedings of the Conference on Continuum Aspects of Graphite Design, November 9–12, 1970, Gatlinburg, Tennessee*, ed. W. L. Greenstreet and G. C. Battle, Jr., CONF-701105, available from National Technical Information Service, Springfield, Va., February 1972.

64. L. J. Broutman, S. M. Krishnakumar, and P. K. Mallick, "Effects of Combined Stresses on Fracture of Alumina and Graphite," *J. Am. Ceram. Soc.* **53**, 649 (1970).

65. J. Jortner, *Multiaxial Behavior of ATJ-S Graphite*, Technical Report AFML-TR-71-160, Air Force Materials Laboratory, Wright-Patterson Air Force Base, Ohio, July 1971.

66. G. T. Yahr, R. S. Valachovic, and W. L. Greenstreet, "Deformation and Fracture of Thin-Walled Graphite Tubes Under Biaxial States of Stress," *Eleventh Biennial Conference on Carbon, Extended Abstracts and Program, June 4–8, 1973, Gatlinburg, Tennessee*, USAEC Report CONF-730601, Oak Ridge National Laboratory, Oak Ridge, Tenn., 1973.

67. R. E. Ely, *Strength Results for Ceramic Materials Under Multiaxial Stresses*, RR-TR-68-1, U.S. Army Missile Command, Redstone Arsenal, Ala., April 1968.

68. R. E. Ely, *Strength Results for Two Brittle Materials Under Biaxial Stresses*, RR-TR-72-11, U.S. Army Missile Command, Redstone Arsenal, Ala., 1972.

69. T. Weng, "Biaxial Fracture Strength and Mechanical Properties of Graphite-Base Refractory Composites," *AIAA J.* 7(5), 851–58 (May 1969).

70. T. Weng, "Room Temperature Fracture Behavior of Polycrystalline Graphites Under Torsional and Biaxial Stresses," paper No. MI 60 presented at Eighth Biennial Conference on Carbon, Buffalo, June 19–23, 1967, State University of New York at Buffalo, June 1967.

71. T. Weng, "Stress-Strain Properties of Grade ATJ Graphite Under Combined Stresses," pp. 222–35 in *Proceedings of the Conference on Continuum Aspects of Graphite Design, November 9–12, 1970, Gatlinburg, Tennessee*, ed. W. L. Greenstreet and G. C. Battle Jr., CONF-701105, available from National Technical Information Service, U. S. Department of Commerce, Springfield, Va., February 1972.

72. S. G. Babcock, S. J. Green, P. A. Hochstein, and J. A. Gum, "Dynamic Biaxial and Elevated-Temperature Properties of ATJ-Graphite," p. 59 in *Proceedings of the Conference on Continuum Aspects of Graphite Design, November 9–12, 1970, Gatlinburg, Tennessee*, ed. W. L. Greenstreet and G. C. Battle, Jr., CONF-701105, available from National Technical Information Service, U.S. Department of Commerce, Springfield, Va., February 1972.

73. J. Jortner, *Multiaxial Response of ATJ-Graphite*, Technical Report AFML-TR-71-253, Air Force Materials Laboratory, Wright-Patterson Air Force Base, Ohio, December 1971.

74. J. Jortner, *Multiaxial Response of ATJ-S Graphite*, Technical Report AFML-TR-73-170, Air Force Materials Laboratory, Wright-Patterson Air Force Base, Ohio, October 1973.

75. R. D. Perkins et al., *Multiaxial Loading Behavior of Four Materials Including ATJ-S Graphite and RAD-6300 Carbon Phenolic*, SAMSO-TR-69-393, Vol. 1, Material Response Studies (MARS II), General Motors Corporation, Warren, Mich., August 1970.

76. F. H. Ho et al., "Biaxial Failure Surfaces of 2020 and PGX Graphites," p. 127 in *Transactions of the 7th International Conference on Structural Mechanics in Reactor Technology*, Vol. L, North Holland, Amsterdam, August 1983.

77. K. R. King, J. O. Bird, and J. R. Bohn, *Thermal Stress Behavior of Polycrystalline Graphite, Part I*, AFML-TR-71-152, Air Force Materials Laboratory, Wright-Patterson Air Force Base, Ohio, July 1971.

78. K. R. King, J. O. Bird, and J. R. Bohn, *Thermal Stress Behavior of Polycrystalline Graphite, Part II. Biaxial Fracture of ATJ-S*, AFML-TR-71-152, Part II, Air Force Materials Laboratory, Wright-Patterson Air Force Base, Ohio, December 1971.

79. K. R. King, J. O. Bird, and J. R. Bohn, *Thermal Stress Behavior of Polycrystalline Graphite, Part III. Special Purpose Tests*, AFML-TR-71-152, Part III, Air Force Materials Laboratory, Wright-Patterson Air Force Base, Ohio, December 1972.

80. C. D. Pears and H. S. Starrett, *Polygraphites Subjected to Temperature Stress Loadings*, Air Force Materials Laboratory, Wright-Patterson Air Force Base, Ohio, March 1973.

81. G. T. Yahr, *Determination of the Relative Thermal Rupture Resistance of Graphites*, ORNL-4467, January 1970.

82. R. W. Derby, "Thermal Shock of Graphite Disks," Ph.D. thesis, Colorado School of Mines, Golden, 1968.

83. H. S. Starrett and R. J. Edwards, "The Detection of Threshold Size Flaws in GraphNOL N3M Graphite by Ultrasonic Pulse Echo," p. 512 in *15th Biennial Conference on Carbon, Extended Abstracts and Program,* June 22–23, 1981, Philadelphia, co-sponsored by The American Carbon Society and The University of Pennsylvania, The University of Pennsylvania, Philadelphia, June 1981.

84. G. B. Engle and R. J. Price, *The Strength Testing of Production Grade H451 Graphite*, GA-A14269, General Atomic Company, San Diego, 1977.

85. H. Sheffé, *Analysis of Variance*, Wiley, New York, 1964.

86. Irving W. Burr, *Applied Statistical Methods*, Academic Press, New York, 1974.

87. M. G. Natrella, *Experimental Statistics*, NBS Handbook 91 Corrected, National Bureau of Standards, Washington, D.C., 1966.

88. H. S. Starrett and R. J. Edwards, "Effect of Flaw Size on the Tensile Strain-to-Failure of GraphNOL N3M Graphite," p. 510 in *15th Biennial Conference on Carbon, Extended Abstracts and Program*, June 22–23, 1981, Philadelphia, co-sponsored by the American Carbon Society and the University of Pennsylvania, The University of Pennsylvania, Philadelphia, June 1981.

89. C. R. Kennedy, Oak Ridge National Laboratory, unpublished data.

# 8. MATERIALS ENGINEERING (WBS 1603)

P. L. Rittenhouse

## 8.1 INTRODUCTION

This activity is directed toward the generation of the metallic materials data base required for the design and licensing of high-temperature gas-cooled reactor (HTGR) primary system components. Work in progress emphasizes reference alloys for critical items such as heat exchangers and reactor internals. Testing includes creep and creep-rupture, low-cycle fatigue, high-cycle fatigue, creep-fatigue interactions, fracture mechanics, and thermal stability.

## 8.2 MATERIALS TECHNOLOGY PLANNING (WBS 1603.01) – P. L. Rittenhouse and J. P. Strizak

Oak Ridge National Laboratory (ORNL) is cooperating with GA Technologies in the preparation of a Metals Technology Development Program Plan. The Plan is to address all the requirements and assumptions related to metallic component designs in the 350-MWt Modular HTGR and the base technology programs needed to satisfy the design data needs that arise from the requirements-assumptions analyses. Designers at GA Technologies are responsible for the requirements-assumptions-data needs process, while ORNL is to develop the specifics of the experimental program including costs and schedules. The "requirements" section of the Plan and associated "design data needs" are scheduled to be available from GA Technologies by the end of January 1986; the first draft of the "base technology" section is to be completed in April 1986.

## 8.3 REACTOR SYSTEM MATERIALS (WBS 1603.02)

### 8.3.1 Creep and Aging Behavior of Hastelloy X and Alternate Alloys – H. E. McCoy

Hastelloy X (Ni–22% Cr–9% Mo–18% Fe–0.10% C) has been the primary material evaluated for high-temperature thermal barrier cover plates.

Five heats of base metal and one heat of weld wire are being evaluated. Hastelloy S is also being evaluated as a filler material. Creep test times exceed 57,000 h, and samples have been aged in HTGR-He* for about 60,000 h. Inconel 617 (Ni–20% Cr–12% Co–9% Mo–0.06% C) is another material considered for this application, and three heats of base metal and one heat of filler metal have been under study. Several creep tests were discontinued after reaching 30,000 to 40,000 h. Some samples are being aged and have reached 60,000 h. Inconel 618 (Ni–22% Cr–15% Fe–6% W–0.04% C) was also evaluated in creep up to 20,000 h. Some base metal and weldment samples of this material are being aged in HTGR-He and have reached about 30,000 h. Inconel 718 (Ni–18% Cr–19% Fe–5% Nb+Ta–3% Mo–0.05% C) base metal was evaluated in the previous year, but some aging samples continue to be exposed after about 30,000 h. Incoloy 802 (Fe–20% Cr–32% Ni–0.5% C) and HD 556 (Fe–22% Cr–20% Ni–20% Co–3% Mo–2.5% W–0.1% C) were evaluated briefly, and summary reports were written on both materials.

Many of the testing details were reported previously.[1] The creep and aging environments are high purity helium with additions of impurities to the following partial pressures (Pa): 34.0 $H_2$, 3.2 $CH_4$, 1.9 CO, 0.2 $H_2O$, and less than 0.05 $N_2$. The test programs for each material included the preparation of weldments for test samples; machining creep and, usually, impact samples of base metal, weld metal, and transverse weld samples; aging samples in HTGR-He; short-term tensile and impact testing of samples in the as-received and aged conditions; and creep testing of as-received and aged samples in air and HTGR-He environments.

The findings for Hastelloy X have been summarized.[2–4] The weldability of the alloy is good although there is a tendency under creep conditions for fracture to occur in the weld metal rather than in the base metal. The alloy is carburized at high temperatures in HTGR-He, but the creep properties are equivalent in air and HTGR-He. Aging affects the short-term tensile properties significantly, with the property change of most concern being the fracture strain at ambient temperature. Fracture strains of only a few percent were noted after some aging treatments, and

*A gas mixture that simulates the impure helium in an operating HTGR.

the impact samples aged at corresponding conditions failed with energies as low as 6 J. Aging for a new thousand hours had no influence on the creep properties, but aging for 53,000 h reduced the creep strength.

The experimental results for Inconel 617 and 618 are summarized in a topical report,[5] and the results of some tests on Inconel 617 aged 53,000 h are given in another report.[4] Inconel 617 was studied more extensively than Inconel 618. Even though Inconel 617 carburized during testing in HTGR-He, the creep properties were equivalent in air and HTGR-He. The creep characteristic of concern for Inconel 617 was that at test temperatures of 600 to 700°C the fracture strain was only 1 to 2%. Higher strains were noted at higher temperatures. The weldability of Inconel 617 was good, and the creep strength of the weld metal was only slightly less than that of the base metal. Aging caused some changes in the tensile properties, but the property of most concern was the reduction in fracture strain at ambient temperature. Elongation at fracture was reduced to about 10%, and impact values were as low as 10 J. Aging for long periods of time (e.g., 53,000 h) caused a small reduction in the creep strength. Inconel 617 has much higher creep strength than Hastelloy X.

Inconel 618 is the most stable alloy evaluated. Even after 20,000 h of aging, the impact energy was about 100 J. Inconel 618 is carburized by HTGR-He, but this does not alter the creep properties from those noted in air. The creep strength of Inconel 618 is about equivalent to that of Hastelloy X.

Inconel 718 is usually placed in service in the age-hardened condition. The aim of the present study was to determine whether prolonged service at 600 to 650°C in HTGR-He would alter the properties. Aging for 10,000 h did not have a detectable effect on the short-term tensile or creep properties, but the impact energy was reduced from 50 J to 10 J. Aging for 20,000 h did bring about some softening when aging at 650°C, but no changes were obvious when aging at 600°C. Aging 20,000 h brought about a further reduction in impact energy to a level of 8 J.

Incoloy 802 and HD 556 were evaluated in a brief program, and the results were presented in a topical report.[6] The heat of Incoloy 802 that we studied contained 0.3% carbon, but it carburized even further during exposure to HTGR-He. The alloy fractured in creep after straining only 1

to 2%. The weldability was quite poor, and Inconel 617 was used as a filler metal to obtain sound welds. Incoloy 802 has excellent creep strength, but it is questionable whether the complications of low ductility and poor weldability are tolerable.

Alloy HD 556 has excellent weldability, and its creep strength is about equivalent to that of Inconel 617. This alloy contains a small amount of lanthanum and has better resistance to carburization than the other alloys studied. However, the very severe embrittlement due to aging may make the alloy very difficult to use. Aging for 1000 h at 870°C reduced the ambient temperature elongation in short-term tensile tests to a few percent and the impact energy to 10 J.

### 8.3.2 Fatigue Behavior of Hastelloy X – J. P. Strizak

Elevated temperature fatigue testing of Hastelloy X in air and HTGR-He continued through September 1985. Fully reversed, strain-controlled fatigue tests were conducted at 650 and 750°C employing a triangular waveform with a strain rate of $4 \times 10^{-3}$/s. Creep-fatigue tests were conducted with hold periods of 0.1 to 1.0 h; thus, creep damage occurred during each cycle via stress relaxation. The typical waveforms employed for strain-controlled fatigue testing are shown in Fig. 8.1.

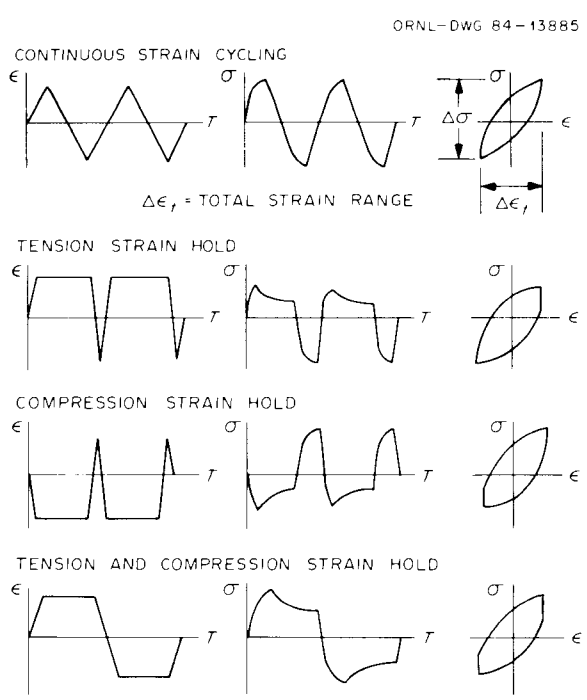


Fig. 8.1. Typical waveforms for strain-controlled fatigue.

Fatigue testing was performed in air and in a typical service environment for gas-cooled reactors (i.e., impure helium). The impure helium included 30.39 Pa $H_2$, 3.04 Pa $CH_4$, 2.02 Pa CO, and 0.20 Pa $H_2O$; the pressure in the environmental chamber was 83 kPa. Additional details concerning equipment, experimental techniques, and the recent fatigue data generated at 650 and 750°C can be found elsewhere.[7]

Continuous cycle fatigue data for solution annealed Hastelloy X at 760°C are shown in Fig. 8.2, where total strain range and related elastic and plastic strain range components are plotted against cycles to failure.

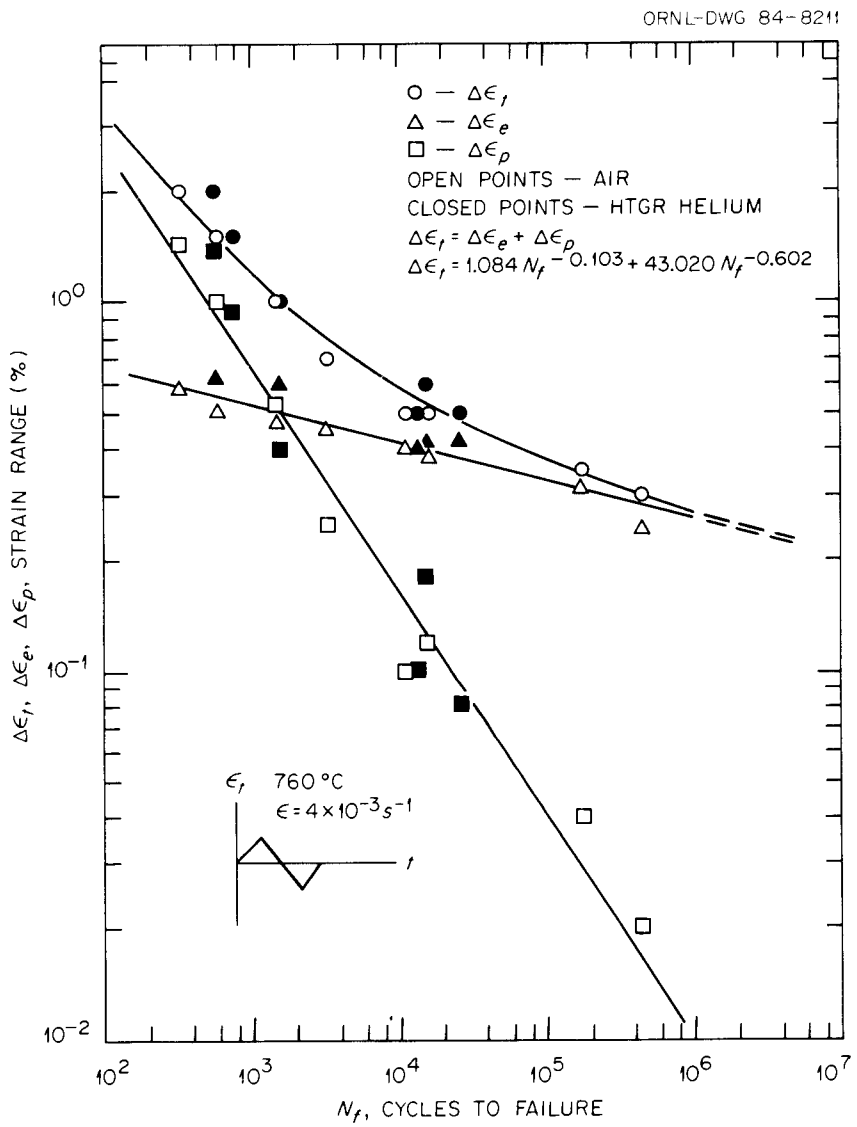


Fig. 8.2. Strain range versus cycles to failure for Hastelloy X at 760°C.

Comparing the data generated in HTGR-He with those obtained in air shows that the helium environment was not detrimental to fatigue life. Previously reported data[8] at 538 and 871°C support this observation. The data in Fig. 8.2 were fit as the sum of simple power law functions for the elastic and plastic strain components.

High-cycle fatigue data for solution annealed Hastelloy X obtained in air at 650 and 760°C are plotted in Fig. 8.3. Results of tests carried out by GA Technologies, Inc. (GA) and General Electric Company (GE) are included. There is considerable scatter in the data, but there are consistent differences in the results obtained at each of the laboratories. The GA data generally show shorter fatigue lives than the data obtained at ORNL or GE, and similarly the GE data show somewhat higher fatigue lives than the ORNL data. As expected, cyclic lifetimes measured at 650°C tend to be somewhat higher than for 760°C. The scatter in the data at 750°C and 760°C could be due to heat-to-heat variations (i.e., small differences in chemical composition and grain size). An understanding of the differences that lead to the scatter in the data will be necessary in order to extrapolate the behavior of Hastelloy X out to higher fatigue lives applicable to component design.

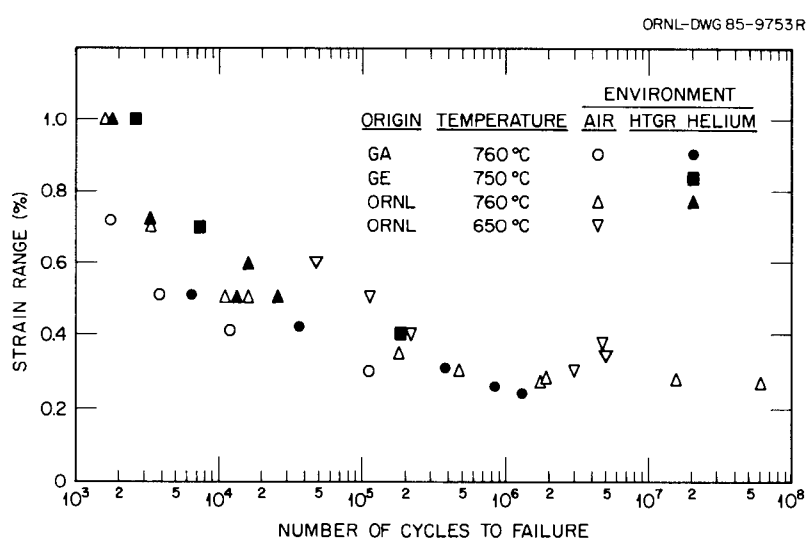


Fig. 8.3. Strain-cycling fatigue data on Hastelloy X at 650 to 760°C.

The introduction of a hold period at the peak tensile or compressive strain amplitude of the strain cycling waveform (see Fig. 8.1) significantly reduced the low-cycle fatigue life of Hastelloy X at 760°C. As shown in Fig. 8.4, life reduction was most pronounced at low strain ranges. Resultant cyclic lives for hold period tests conducted at strain ranges less than 0.6% were about an order of magnitude lower than for tests with no hold period. Figure 8.4 indicates that compressive hold periods were generally somewhat more damaging to the fatigue life of Hastelloy X than tensile hold periods. The most damaging effect occurred when a hold period was introduced at both the tensile and compressive strain amplitudes of the cyclic waveform.

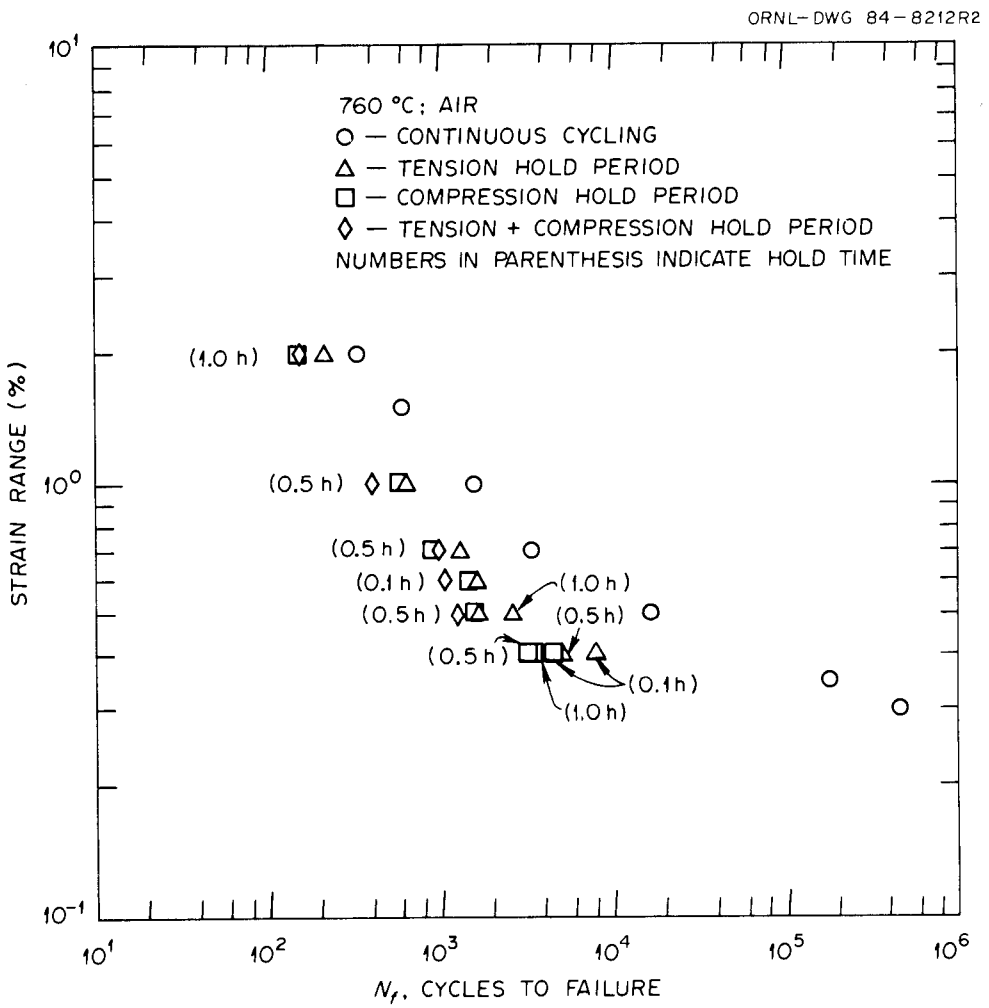


Fig. 8.4. Both tension and compression hold periods are deleterious to the fatigue life of Hastelloy X at 760°C.

Resultant cyclic lives for hold period tests conducted in air and HTGR-He environments at a strain range of 0.5% were about an order of magnitude lower than for tests with no hold period. At this particular strain range the compressive hold period was no more damaging to fatigue life than the tensile hold period. Fatigue lives for tests conducted in air at 0.4% strain range are shown in Fig. 8.5. The "no hold" fatigue life of Hastelloy X was decreased by 88% when a 0.1-h tension hold period was introduced and by 93% for a 0.1-h compression hold period. Increasing the hold time to 0.5 decreased the "no hold" fatigue life somewhat more.

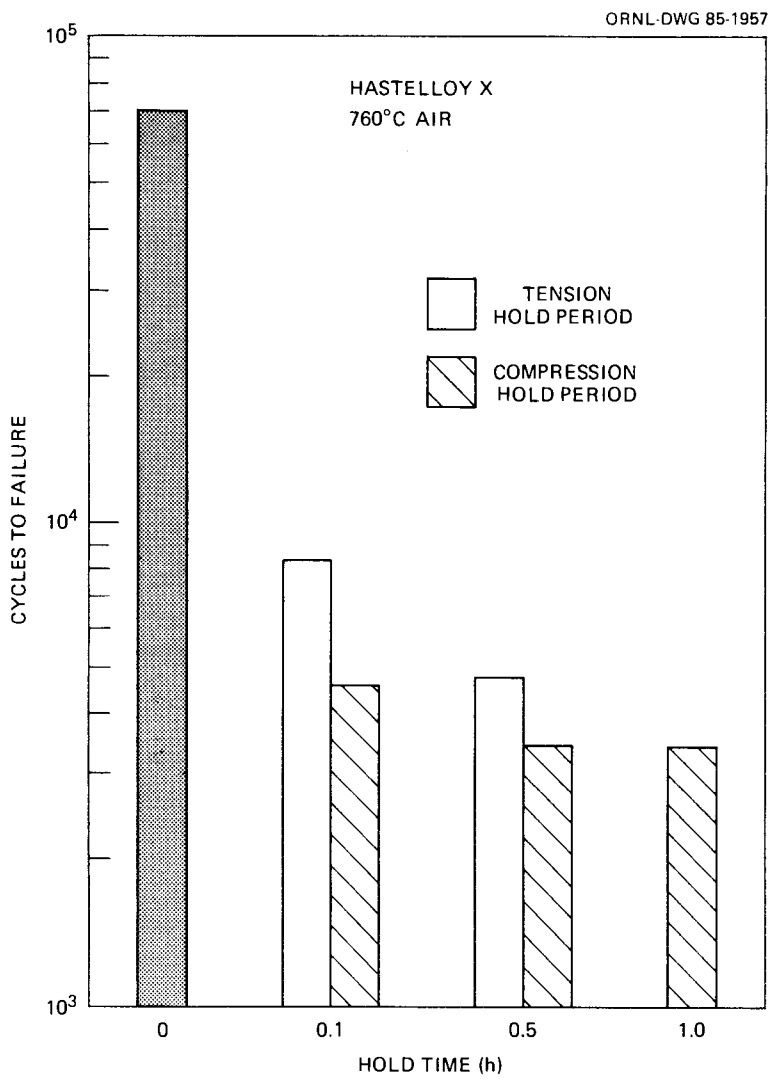


Fig. 8.5. Compressive hold periods were more deleterious to fatigue life than were tensile hold periods.

The fatigue lives for tests with 0.5- and 1.0-h compressive hold periods were essentially the same. Comparing the data generated in HTGR-He with that obtained in air (see Fig. 8.6) indicates that the helium environment was slightly beneficial.

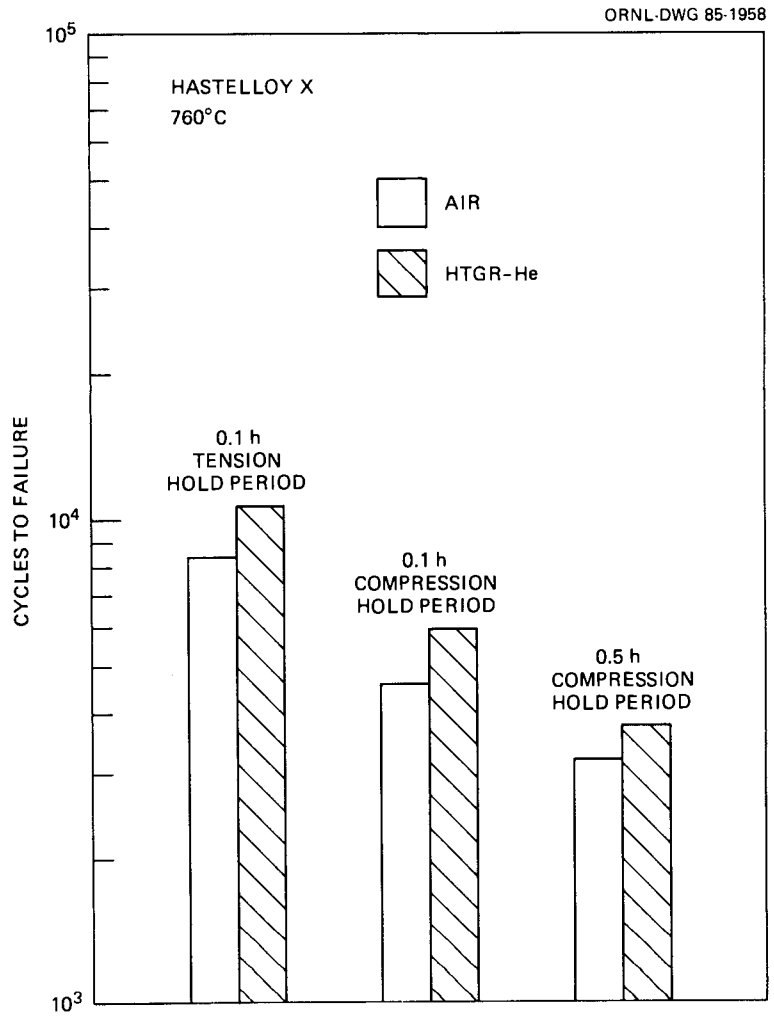


Fig. 8.6. HTGR-helium was somewhat beneficial to creep-fagitue cycle life.

Figure 8.7 is a plot of the tensile versus compressive stress amplitudes from the creep-fatigue tests conducted at 760°C. As stress amplitudes decreased, corresponding to lower strain ranges more applicable to design conditions, mean tensile stresses were developed in tests with compressive hold periods and compressive mean stresses were developed in tests with tensile hold periods. Investigations[9] of mean stress influence

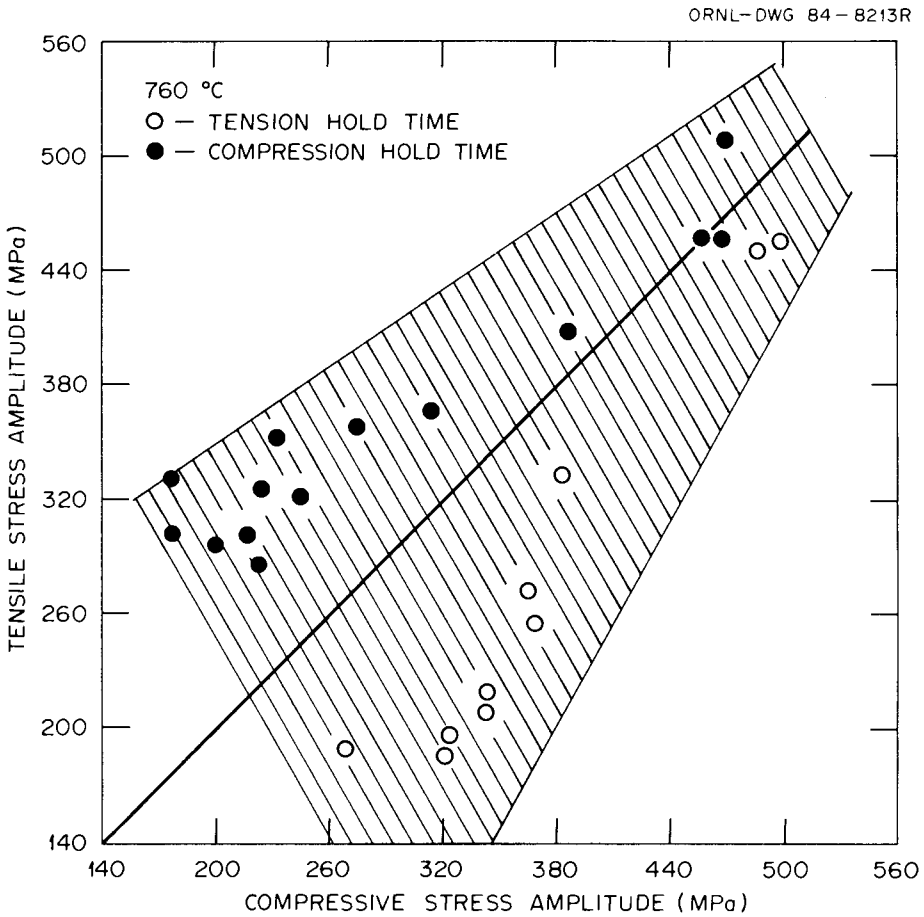


Fig. 8.7. Significant mean stresses developed in creep-fatigue tests at low strain ranges.

on fatigue strength have generally shown that tensile mean stresses are detrimental to fatigue life compared with fully reversed, cyclic loading. The development of tensile mean stresses when compressive hold times are imposed is perhaps an explanation of why compressive hold periods are more damaging to fatigue life than are corresponding tensile hold periods in either air or HTGR-He environments.

Of the many methods that have been employed to extrapolate available creep-fatigue data or to estimate time dependent fatigue life of materials, linear damage summation is perhaps the most widely known and simplest. Generally, it is stated[10] as

$$Dc + Df = 1 \text{ (at failure)} , \qquad (1)$$

where $Dc$ and $Df$ are the creep and fatigue damage values respectively. This method, which is recognized by the American Society for Mechanical Engineers, Code Case N-47 (ref. 11), uses time and cycle ratios as follows:

$$d\ t/tr + d\ n/Nf = D\ , \tag{2}$$

where

$D$ = total creep-fatigue damage,

$t$ = time duration at a particular load condition,

$tr$ = time-to-rupture from isothermal stress-rupture curves for a given loading condition,

$n$ = number of applied cycles at a particular loading condition,

$Nf$ = number of cycles to failure at a particular strain range.

The damage values determined for the creep-fatigue tests of solution annealed Hastelloy X are plotted in Fig. 8.8.

It is apparent in Fig. 8.8 that a unique damage sum value $D$ does not occur and that a linear damage summation (i.e., $D$ = 1) is not appropriate.

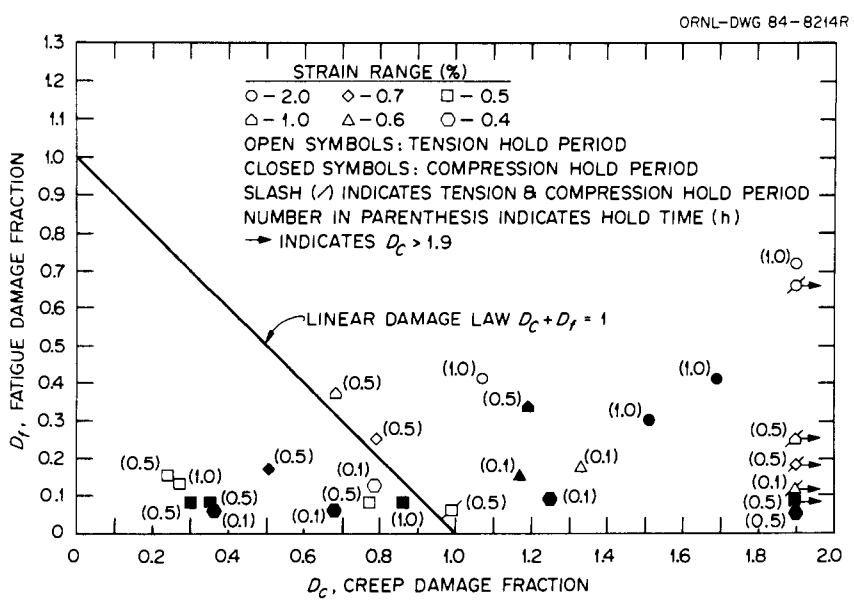


Fig. 8.8. Fatigue damage fractions versus creep damage fractions for Hastelloy X tested in strain control at 760°C with various hold times.

Similar conclusions have been made for other structural materials including 2.25Cr-1Mo steel,[12] type 304 stainless steel,[13] and alloy 800H.[14]

A limited number of creep-fatigue tests were conducted at 760°C in air on thermally aged Hastelloy X. Prior to specimen machining, small blocks (12-mm-square × 140-mm-long) of solution annealed material (heat 4936) were aged in an argon environment for 20,000 h at temperatures of 704 and 871°C. Figure 8.9 gives the fatigue lives for continuous cycling and tension and compression hold period tests conducted at a strain range of 2% on solution annealed and thermally aged material. For each of the three cyclic loading conditions, resultant fatigue lives for the thermally aged material were

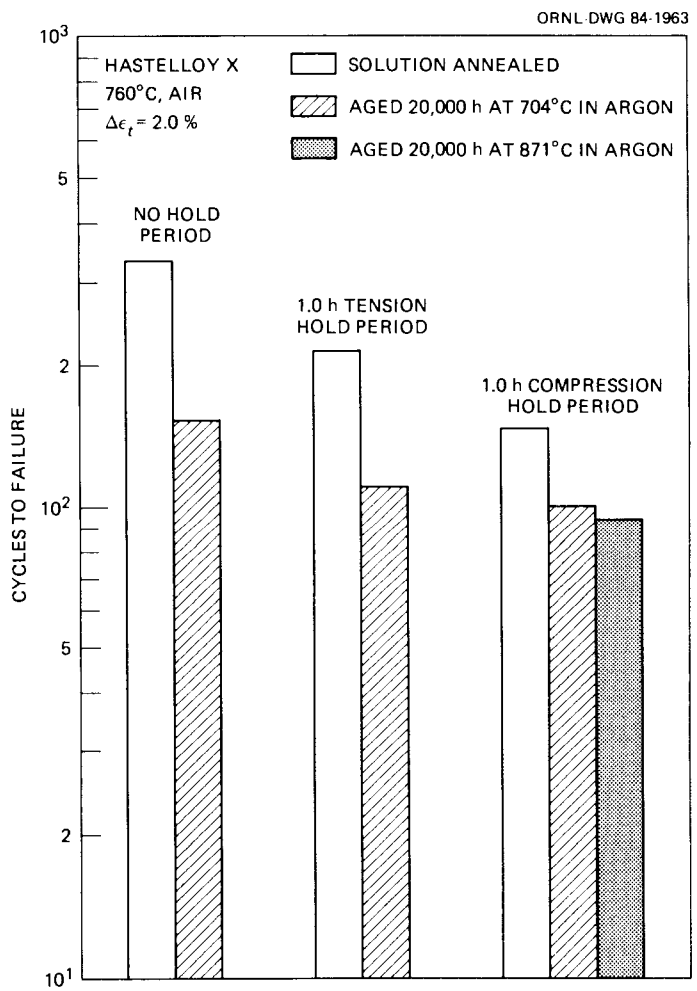


Fig. 8.9. Resultant fatigue lifetimes for tests on solution annealed and thermally aged Hastelloy X employing various fully reversed strain-controlled cyclic waveforms.

lower than those for solution annealed material. Results of similar tests at 0.5% strain range with 0.5-h compression hold periods showed a lower fatigue life for aged material. Reduced fatigue strength due to thermal aging of Hastelloy X has been previously observed.[8]

## 8.4 HEAT TRANSPORT MATERIALS (WBS 1603.04)

### 8.4.1 Creep, Aging, and Decarburization of 2.25Cr-1 Mo Steel - H. E. McCoy

Creep and aging tests are being performed on four heats of 2.25Cr-1Mo steel. Three of the heats have been studied rather extensively, and test times have reached 75,000 h. The fourth heat is from a vacuum-arc-remelted ingot made by Cameron Iron Works. It has been aged in sodium to remove most of the carbon, and the effects of decarburization are being evaluated. Several of the heats are being aged in HTGR-He at 593 and 649°C and have reached times slightly in excess of 20,000 h. Many of the details of creep testing were reported previously.[15]

The initial heat treatment used for all four heats consisted of heating 30 minutes at 927 ± 14°C, cooling to 704 ± 14°C at a maximum rate of 83°C per hour, holding at 704 ± 14°C for 2 h, and cooling to room temperature at a maximum rate of 6°C per minute. Klueh found that this heat treatment results in a microstructure consisting mostly of proeutectoid ferrite and some bainite.[16] In the same study, Klueh noted that aging in the 500 to 700°C range resulted in coarsening of the bainite structure, so that the microstructure approached that of ferrite and spheroidized carbides. Some hardening was associated with the process, depending on the aging temperature and time.

The gas/metal equilibrium in our test environment is such that 2.25Cr-1Mo is carburized at 480°C, decarburized at 595 and 650°C, and unchanged in carbon content at 540°C. The kinetics of carburization at the lowest temperature are very slow, and the creep properties do not seem to be affected. At 650°C the kinetics of decarburization are rather rapid, and samples tested in HTGR-He creep slightly faster than those tested in air. The fracture strain of this alloy is quite high under all conditions, and fracture strain does not appear to be a problem. All four heats react to the test environment in the same way, and the properties are about the same.

The decarburization studies thus far have been restricted to one heat, and the available results were summarized.[17] Samples were decarburized in sodium at 671°C for 522 and 4000 h, and controls were run in argon for equivalent times and temperatures. The initial carbon content of the alloy was about 750 ppm; annealing in sodium for 522 h at 671°C reduced the carbon level to 500 ppm, and annealing in sodium for 4000 h reduced the carbon level to about 170 ppm. Metallographic examination showed that aging at 671°C caused carbide coarsening but did not cause grain growth. Aging in argon caused a reduction in the short-term tensile and creep properties, and aging in sodium caused even greater property changes. The property changes also increased with increasing aging or decarburization time.

### 8.4.2 Fracture Mechanics – R. K Nanstad and R. W. Swindeman

#### 8.4.2.1 Introduction

The current design for the GA Technologies HTGR incorporates a steam generator with 2.25Cr-1Mo tubing in the economizer-evaporator-superheater section. The specific material selected for the tubing is annealed 2.25Cr-1Mo, ASME specification SA-213 grade T22. The design incorporates tubing[18] of 22.2-mm (0.875-in.) outside diameter with 3.3-mm (0.13-in.) wall thickness. The design operating temperature is in the range 454 to 538°C (850–1000°F). Thus, the material will operate in the temper embrittlement range for this material, and degradation of toughness must be considered. The requirements that have been identified are fatigue crack growth rate (FCGR), creep crack growth rate (CCGR), and fracture toughness.

The program devised for the past year has focused on defining material for preliminary tests, additional development of elevated-temperature test techniques and instrumentation, characterization of material, and performance of initial testing. The following sections describe the test material and provide results from characterization tests (i.e., tensile, creep, and Charpy impact) and crack growth testing (i.e., FCGR, CCGR, and fracture toughness).

#### 8.4.2.2 Material

The material used for this preliminary study is a 19-mm-thick plate of 2.25Cr-1Mo steel (heat 80522-53, slab 68615) manufactured by the Phoenix

Steel Corporation and heat treated to satisfy ASME Specification SA-387 grade 22 class 1. The plate was annealed at 913°C (1675°F) for 1 h and furnace cooled to 482°C (900°F) at a rate of 56°K/h (100°R/h), then air cooled. The chemical composition is compared with the specification in Table 8.1 to show that the plate composition meets the SA-387 specification. The microstructure of the plate, shown in Fig. 8.10(*a*), reveals a banded structure with about 20% pearlite in a predominantly ferrite microstructure. The hardness was determined to be HRB 76.5. A section of tubing from the Delmarva HTGR (supplied by GA Technologies) was examined and is shown in Fig. 8.10(*b*). Except for the banding of the plate, the microstructures are similar.

Table 8.1. Chemical compositon of annealed 2.25Cr-1Mo steel plate

| Identification | Composition (wt %)[a] | | | | | | |
|---|---|---|---|---|---|---|---|
| | C | Mn | P | S | Si | Cr | Mo |
| Heat 80522-53 | 0.11 | 0.36 | 0.010 | 0.018 | 0.26 | 2.19 | 0.96 |
| SA-387 grade 22 class 1 | 0.15 | 0.25/0.66 | 0.035 | 0.035 | 0.50 | 1.88/2.62 | 0.85/1.15 |

[a]Single values are maximum contents allowable.

### 8.4.2.3 Tensile Testing

Tensile tests were performed with threaded, round specimens 6.4 mm (0.252 in.) in diameter and 25.4 mm (1 in.) in gage length. The tests were conducted at 25, 510, 538, and 566°C (77, 950, 1000, and 1050°F). The results are shown in Table 8.2, which includes the requirements of SA-387. The specification requirements are met by the material. The yield strength shows only a slight decrease from 510 to 566°C, but the ultimate strength decreases from 404 to 336 MPa (58.6 to 48.8 ksi) over that temperature range. These observations are consistent with the information shown in the ASME Code, Section III Appendices. The fracture strength decreases substantially, as expected, and the measures of ductility are typical results.

Y-203755

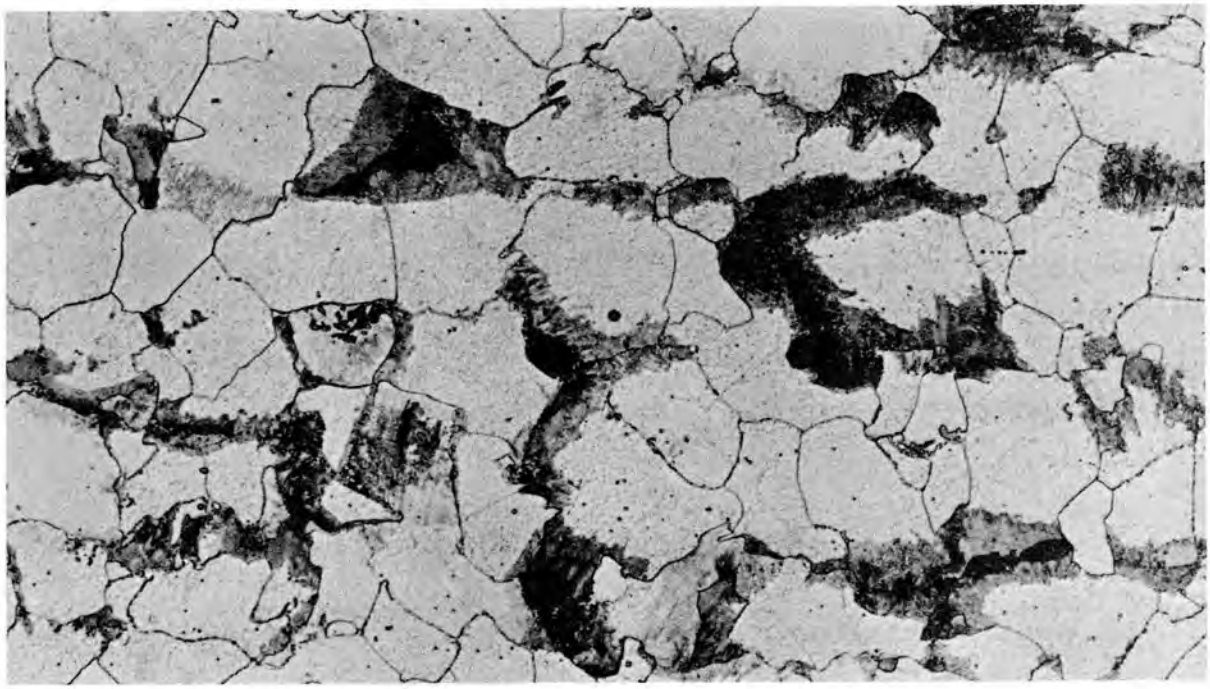

(*a*)

Y-204538

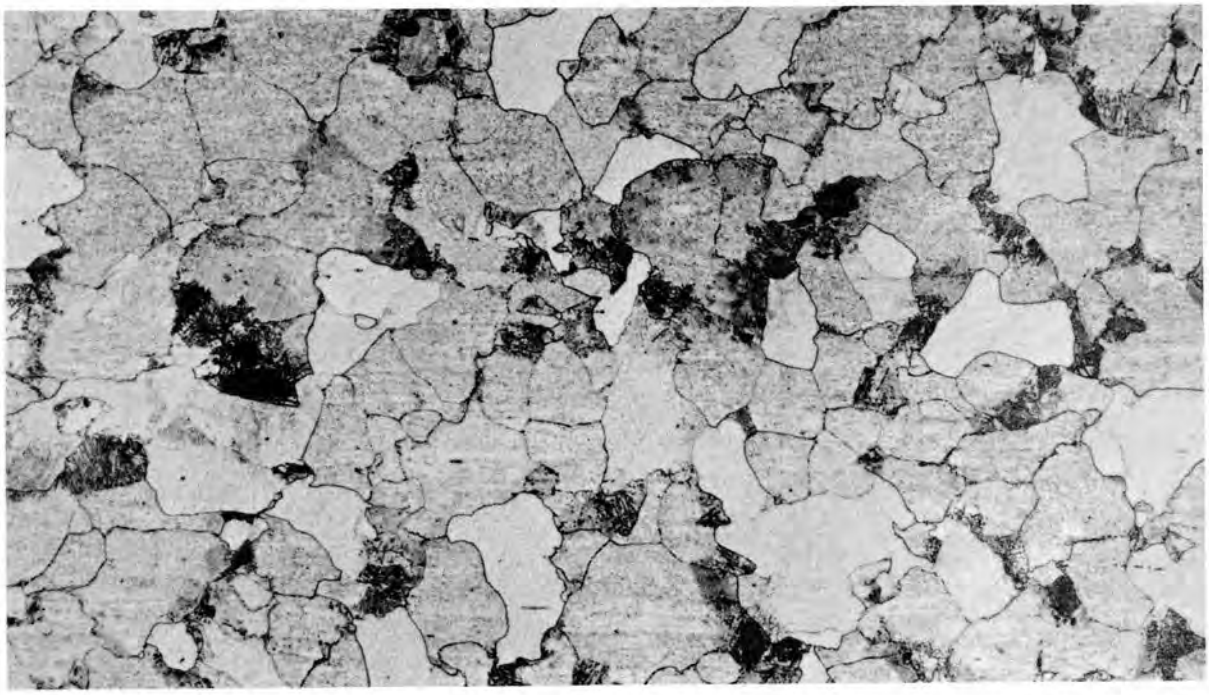

(*b*)

40 μm

Fig. 8.10. Microstructure of (*a*) annealed 2.25Cr-1Mo steel plate and (*b*) annealed 2.25Cr-1Mo steel tubing. Microstructure is predominantly ferrite with about 20% pearlite.

Table 8.2. Tensile properties of annealed 2.25Cr-1Mo steel plate

| Identification | Test temperature °C (°F) | Strength, MPa (ksi) | | | Uniform strain (%) | Elongation (%) | Reduction of area (%) |
|---|---|---|---|---|---|---|---|
| | | Yield | Ultimate | Fracture | | | |
| Specimen GA-1 | 25 (77) | 279 (40.4) | 491 (71.2) | 339 (49.2) | 17.0 | 34.9 | 68.0 |
| Specimen GA-2 | 510 (950) | 198 (28.6) | 404 (58.6) | 210 (30.5) | 13.6 | 38.3 | 76.8 |
| Specimen GA-3 | 538 (1000) | 198 (28.7) | 377 (54.7) | 176 (25.6) | 13.4 | 43.1 | 75.7 |
| Specimen GA-4 | 566 (1050) | 193 (28.0) | 336 (48.8) | 140 (20.3) | 14.3 | 47.7 | 81.4 |
| SA-387[a] | Room | | 415–585 (60–85) | 207 (30.0) | | 18.0 | 45.0 |

[a]Single values are minimum values allowable.

### 8.4.2.4 Charpy Impact Testing

Charpy V-notch impact tests were conducted over a wide temperature range. In addition to absorbed energy, the lateral expansion was measured with a dial gage device, and the fracture appearance (percent shear) was estimated.

Curve fitting was performed by using a nonlinear regression technique with the hyperbolic tangent (tanh) function. The results of absorbed energy versus temperature are shown graphically in Fig. 8.11. The material has a 41-J (30-ft-lb) transition temperature of about 22°C (72°F) and an upper-shelf energy level of 147 J (108 ft-lb). The ductile-brittle transition (50% cleavage, 50% shear fracture) occurs at about 42°C (108°F). The transition region for this steel is relatively high, but typical of annealed 2.25Cr-1Mo steel.

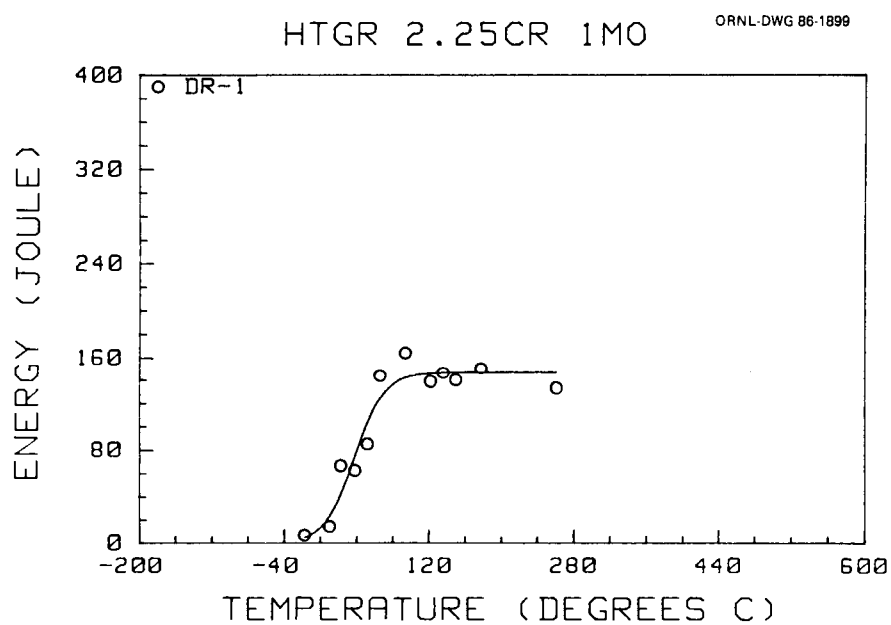


Fig. 8.11. Charpy V-notch impact energy versus temperature for annealed 2.25Cr-1Mo steel plate.

### 8.4.2.5 Creep and Creep Crack Growth Testing

In order to form a data base on which to interpret creep crack growth experiments on 2.25Cr-1Mo steel, creep rupture testing is under way at 510, 538, and 566°C (950, 1000, and 1050°F). Two such tests have been

completed, and six others are under way with the longest test now in excess of 5000 h. These data were combined with results of tensile tests to construct isochronous stress versus strain curves to compare with those in ASME Code Case N-47. Typical data for 538°C are shown in Fig. 8.12. The tensile curve for the material being tested in creep crack growth is about 25 MPa (3 ksi) below the tensile curve for representing average behavior in Code Case N-47. The creep strength of our material is much higher, however, and is almost double that reported in Code Case N-47 for 1000 h. Testing will continue until 10,000 h.

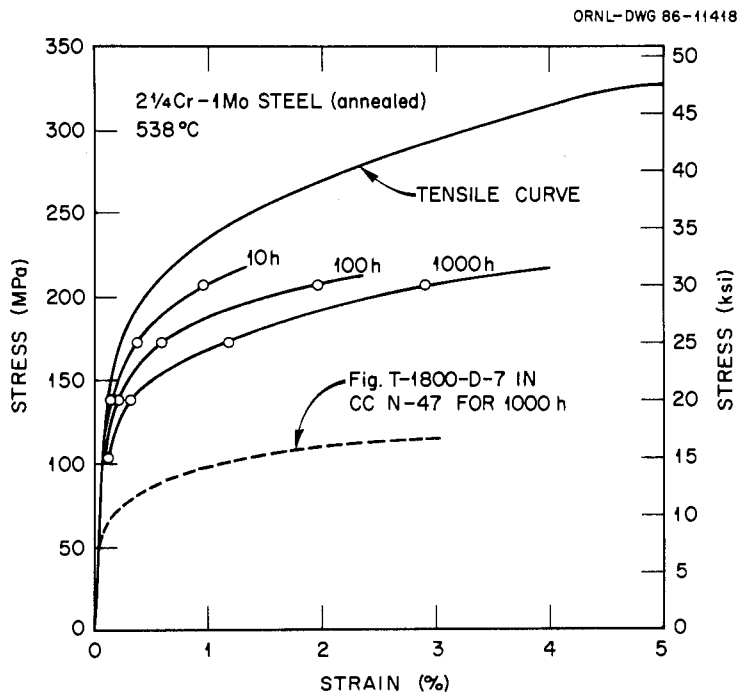


Fig. 8.12. Isochronous creep curves for 2.25Cr-1Mo steel at 538°C.

Exploratory testing is under way to develop test procedures and analytical methods for CCGR evaluations. Two specimen sizes are being examined, both of which are of the modified compact specimen design. The larger specimen is the nominal 1TCS [25.4-mm-thick (1-in.) compact specimen] design in the plane section with a thickness of 12.3 mm (0.5 in.). The smaller specimen is the nominal 1/2T design. All work to date has been performed on the larger specimens.

Prior to CCGR testing, the samples were precracked at room temperature by using a 10-Hz sinusoidal wave with a minimum-to-maximum load ratio of 0.1. After precracking, the ratio of crack length to width (a/W) was approximately 0.45. Potential drop (PD) leads were attached to the specimens at locations identified by McGowan and Nanstad,[19] and their calibration curve for relating crack length to PD is being examined as part of the experimental methods development. Tests were performed in a 12/1 lever arm creep machine capable of 24-kN (6000-lb) loads.

In the first test, a specimen without side grooves was examined. Here the net section stress of 40 MPa (5650 psi) was imposed at 538°C (1000°F) for 140 h. After discontinuing the test, the sample was broken open for examination. A thumbnail creep crack front was observed that measured approximately 1.5 mm (0.057 in.) at the center and near zero at the surfaces. The crack growth estimated by the PD method was about 0.94 mm (0.037 in.), which appeared to represent an "average" crack growth measurement. The displacement at the load line position was near 0.71 mm (0.028 in.). This was close to the 0.74 mm (0.03 in.) estimated from the dial gage measurements on the load train.

A second creep crack growth test was performed on a 10% side-grooved specimen at 538°C (1000°F). The net section stress was increased to 56 MPa (8180 ksi) to produce more rapid creep crack growth. The specimen failed in 17.7 h. The creep crack grew more uniformly and reached a size estimated to be near 1.8 mm (0.073 in.) before rapid failure. This measurement was consistent with the extrapolation of PD calculations. A third test at 538°C (1000°F) and a lower net section stress is in progress.

Many parameters have been proposed to correlate CCGR data. Some of these are stress intensity factor (K), J-integral, J*-integral, net section stress, and reference stress. For preliminary calculations, stress intensity, K, has been used here. For the smooth-sided specimen, a K of about 30 MPa$\sqrt{m}$ resulted in a CCGR of about $6.7 \times 10^{-3}$ mm/h. For the side-grooved specimen, a K of about 40 MPa$\sqrt{m}$ resulted in a CCGR of about $1.0 \times 10^{-1}$ mm/h. For comparison, these values have been plotted (see Fig. 8.13) on a graph of CCGR versus K for Cr-Mo-V steel tested at 565°C (ref. 20). The results

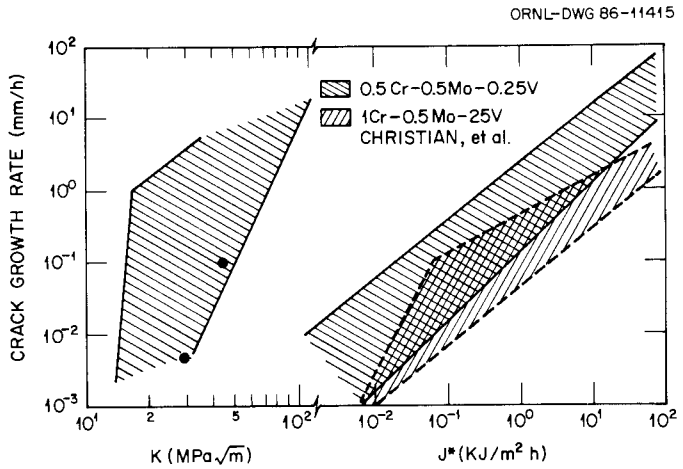


Fig. 8.13. Creep crack growth rate of annealed 2.25Cr-1Mo steel plate at 538°C compared with that for Cr-Mo-V steel at 565°C.

from these tests compare favorably with the scatter band shown in the figure. Further analyses will be performed using other characterizing parameters such as $J^*$.

### 8.4.2.6 Fatigue Crack Growth Testing

Fatigue crack growth rate tests were conducted at 24 and 260°C (75 and 500°F). The specimen design was a 1TCS planar specimen 12.5 mm (0.5 in.) thick. The crack extension was measured visually and by use of a compliance technique. The dc-potential drop technique, demonstrated previously with alloy 718 (ref. 19), will be utilized following final assembly of an improved computer interface.

The results of FCGR tests are shown in Fig. 8.14. The results are not affected significantly by temperature from 24 to 260°C, but that is not surprising for this alloy. There are not enough data to examine threshold behavior; thus, linear curve fits were drawn only in the stable FCGR region. Although data smoothing has not yet been performed as outlined in ASTM E647, the data compare reasonably well with previous data obtained with annealed 2.25Cr-1Mo at room temperature. Further testing is under way at 538°C (1000°F), and testing plans will incorporate different frequencies and R ratios using the dc-potential drop technique.

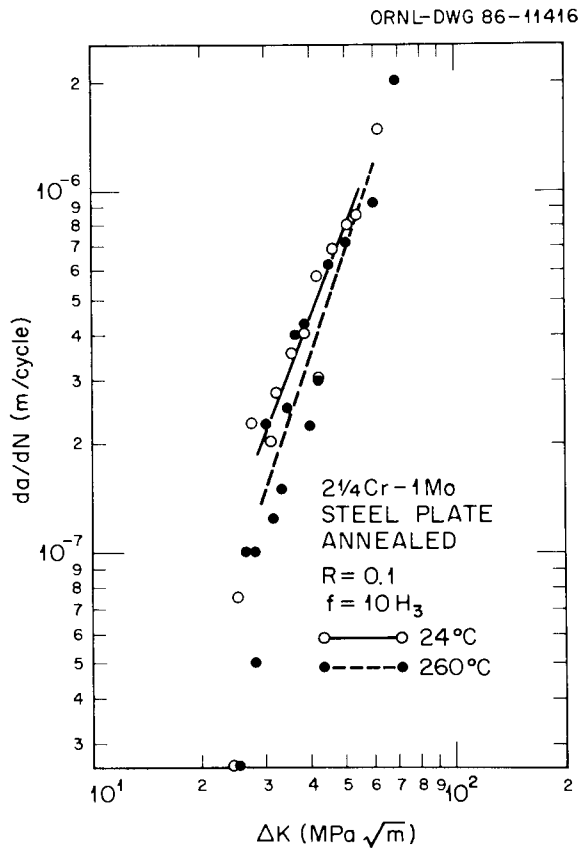


Fig. 8.14. Fatigue crack growth rate (da/dn) versus ΔK for annealed 2.25Cr-1Mo steel plate at 24 and 260°C. A sinusoidal wave form at 10 Hz and an R ratio of 0.1 were used.

### 8.4.2.7 Fracture Toughness Testing

Fracture toughness testing was performed with a computer-interactive servohydraulic system. The specimens are 1TCS planar dimensions of 19-mm thickness and side grooved 10% on each face (20% total). Razor blades are mounted on the specimen for load-line displacement measurements, and holes are located on the front face for placement of dc-potential drop current leads. Prior to side grooving, the specimens were precracked in fatigue to an a/W ratio of about 0.62. The single specimen unloading compliance technique was used.

The $J_{Ic}$ value is determined by using two techniques: (1) the linear regression method of E813, and (2) the intersection of a power law curve fit with the first exclusion line as described by Loss et al.[21] The modified-Ernst J expression[22] was used for J calculations.

Tests have been performed at 24 and 260°C. The test at 24°C experienced some ductile tearing followed by mode conversion to cleavage. The cleavage instability occurred prior to limit load. The test at 260°C experienced substantial ductile tearing with no instabilities. The actual J-R plots are shown in Figs. 8.15 and 8.16. The test at 24°C shows a very steep J-R curve compared with that for the test at 260°C. Of course, the comparison is somewhat tenuous because the room temperature test was interrupted by a cleavage failure and only a few data points were taken between the offset lines. However, the load-displacement traces show that the lower-temperature test failed prior to limit load and at a displacement of about 1.8 mm, a displacement value that occurred beyond limit load for the higher-temperature test. The 260°C test likely experienced some strain hardening because the strain hardening exponent at

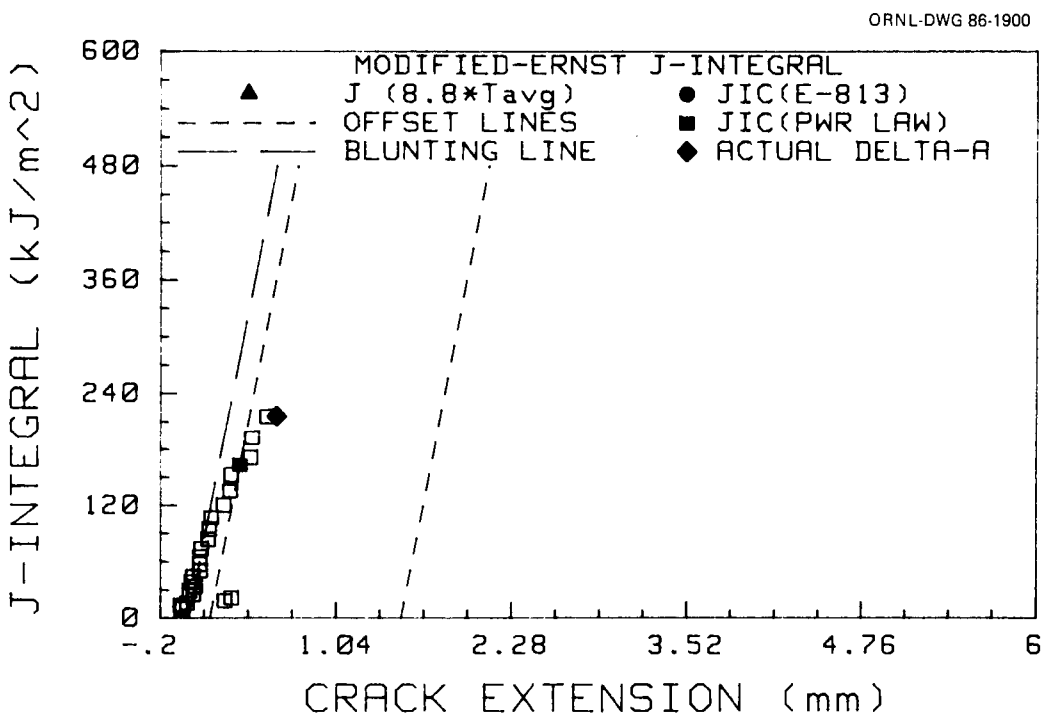


Fig. 8.15. The J versus Δa plot for unloading compliance test of annealed 2.25Cr-1Mo steel plate at 24°C.

ORNL-DWG 86-1901

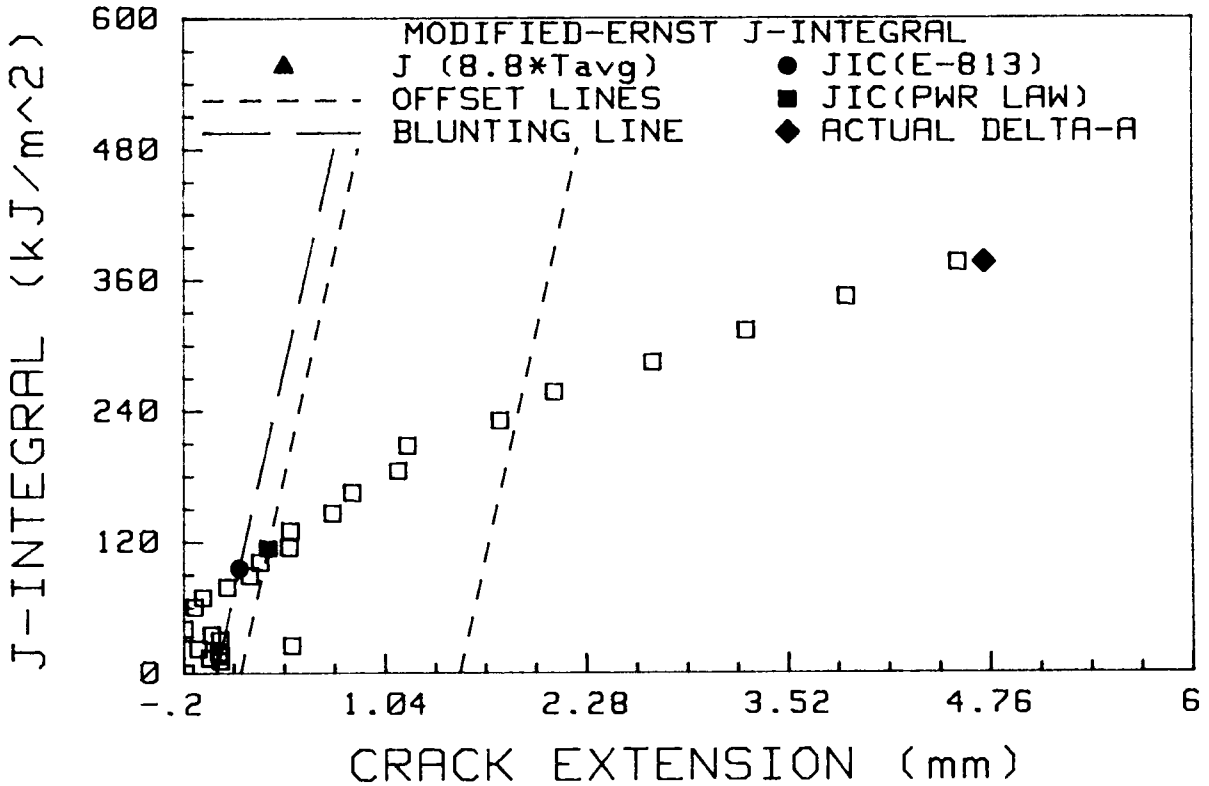


Fig. 8.16. The J versus Δa plot for unloading compliance test of annealed 2.25Cr-1Mo steel plate at 260°C.

260°C is somewhat higher than that at 24°C. If power law $J_{Ic}$ determinations are compared, the test at 24°C resulted in a higher $K_J$ (where $K_J^2 = EJ_{Ic}$), 163.6 MPa $\sqrt{m}$, than that for the test at 260°C, 143.3 MPa $\sqrt{m}$. That is not an expected result; the $K_J$ value of the test at 260°C is surprisingly low. To examine the accuracy of the test, the final computer-predicted and actual measured crack extension values are compared, and both tests show agreement within about 2%, an excellent result. Thus, the tests were good tests, but the results amplify the problems with the use of the J-R procedure in the transition region and with materials that exhibit steep J-R curves. Even so, the results are in the range of those reported by other investigators.

Further testing is under way at temperatures up to 538°C. For the high-temperature tests, the dc-potential drop technique will be used with a new high-speed, five-channel computer interface.

## 8.5 REFERENCES


1. H. E. McCoy, *Creep Behavior of Hastelloy X, 2 1/4 Cr-1 Mo Steel, and Other Alloys in Simulated HTGR Helium,* ORNL/TM-6822, June 1979.

2. H. E. McCoy and J. F. King, *Evaluation of Hastelloy X for Gas-Cooled Reactor Applications*, ORNL/TM-8499, November 1982.

3. H. E. McCoy, J. P. Strizak, and J. F. King, "Hastelloy X for High-Temperature Gas-Cooled Reactor Applications," *Nucl. Technol.* **66**, 161–74 (July 1984).

4. H. E. McCoy, *Mechanical Properties of Hastelloy X and Inconel 617 After Aging 53,000 Hours in HTGR-He,* ORNL/TM-9604, September 1985.

5. H. E. McCoy and J. F. King, *Mechanical Properties of Inconel 618 and 618,* ORNL/TM-9337, February 1985.

6. H. E. McCoy and J. F. King, *Evaluation of HD556 and Incoloy 802 for High-Temperature Gas-Cooled Reactor Application,* ORNL/TM-9382, January 1985.

7. J. P. Strizak, *Interim Results of High-Cycle and Creep-Fatigue Testing of Hastelloy X,* ORNL/GCR-85/14, September 1985.

8. J. P. Strizak et al., *The Influence of Temperature, Environment and Thermal Aging on the Continuous Cycle Fatigue Behavior of Hastelloy X and Inconel 617,* ORNL/TM-8130, April 1982.

9. H. O. Fuchs and R. I. Stephens, *Metal Fatigue in Engineering*, John Wiley & Sons, New York, 1980.

10. C. F. Coffin, *Methods for Predicting Material Life in Fatigue,* The American Society of Mechanical Engineers, New York, 1979, pp. 1–24.

11. *Interpretations of the ASME Boiler and Pressure Vessel Code Case N-47,* The American Society of Mechanical Engineers, New York, 1974.

12. M. K. Booker, *Analysis of the Long-Term Creep-Fatigue Behavior of 2 1/4 Cr-1 Mo Steel*, ORNL/TM-7068, December 1979.

13. C. E. Jaske, H. Mindlin, and J. S. Perrin, *Fatigue at Elevated Temperatures*, STP-520, ed. A. E. Carden, A. J. McEvily, and C. H. Wells, American Society for Testing and Materials, Philadelphia, 1973, pp. 365–76.

14. J. M. Hyzak and D. A. Hughes, *An Evaluation of Creep-Fatigue Life Prediction Models for the Solar Central Receiver*, Technical Report SAND 81-220, Sandia Laboratories, 1981.

15. H. E. McCoy, *Creep Behavior of Hastelloy X, 2 1/4 Cr-1 Mo Steel, and Other Alloys in Simulated HTGR Helium,* ORNL/TM-6822, June 1979.

16. R. L. Klueh, *Thermal Aging Effects on the Mechanical Properties of Annealed 2 1/4 Cr-1 Mo Steel,* ORNL-5324, November 1977.

17. H. E. McCoy, *Influence of Decarburization on the Tensile and Creep Properties of 2 1/4 Cr-1 Mo Steel,* ORNL/TM-9887, November 1985.

18. Private communication, M. Kozina, GA Technologies, to R. K. Nanstad, Oak Ridge National Laboratory, January 23, 1985.

19. J. J. McGowan and R. K. Nanstad, "A Direct Comparison of Unloading Compliance and Potential Drop Techniques in J-Integral Testing," pp. 136–40 in *Computer-Aided Testing and Modal Analysis*, proceedings of the 1984 SEM Fall Conference, Milwaukee, Nov. 4–7, 1984.

20. K. Sadananda and P. Shahinian, "Review of the Fracture Mechanics Approach to Creep Crack Growth in Structural Alloys," *Engineering Fracture Mechanics* **15**(3–4), 327–42 (1981).

21. F. J. Loss, ed., *Structural Integrity of Water Reactor Pressure Boundary Components, Annual Report, Fiscal Year 1979*, NUREG/CR-1128, NRL Memorandum Report 4122, Naval Research Laboratory, Washington, D.C., 1979.

22. H. A. Ernst, "Material Resistance and Instability Beyond J-Controlled Crack Growth," pp. 191–213 in *Elastic-Plastic Fracture, Inelastic Crack Analysis*, STP 803, vol. 1, ed. C. F. Shih and J. P. Gudas, American Society for Testing and Materials, Philadelpia, 1983.

# 9. REACTOR VESSEL DESIGN SUPPORT (WBS 1700.11)

R. K. Nanstad, P. L. Rittenhouse, G. C. Robinson, and
G. D. Whitman

## 9.1 ASSESSMENT OF STEEL PRESSURE VESSELS FOR MODULAR HTGR SYSTEMS

### 9.1.1 Background and Scope

The selection of the modular HTGR (MHTGR) with its steel reactor pressure vessel as the U.S. reference concept led to the need for a critical evaluation of a number of factors relative to the pressure vessel design being developed by Combustion Engineering. Although the vessel was only in the stage of preconceptual design, it was deemed prudent to examine in some detail the material selection, preliminary stress evaluations and seismic analysis, manufacturing and transportation capabilities, neutron embrittlement, and materials behavior during emergency conditions. The conclusions of the study conducted at Oak Ridge National Laboratory (ORNL) were generally supportive of the MHTGR steel vessel and the material selected. This was documented in a letter report issued on July 9, 1985.

### 9.1.2 Vessel Material

The largest single effort in the ORNL assessment was a detailed review of the metallurgical and irradiation behavior of the MHTGR vessel material (ASME SA-533 grade B class 1 steel). Special attention was given to strain aging, temper and stress-relief embrittlement, creep, irradiation effects, fracture mechanics applications and correlations, and the status of the steel in the ASME Code. It was concluded that the choice of this steel, also the normal material of construction for light-water reactor pressure vessels, appears reasonable based on metallurgical factors. At the vessel

operating temperature [260°C (500°F)] quoted for the preconceptual design, it was estimated that the transition temperature shift resulting from irradiation could be limited to less than 56°C (100°F) by careful selection of material chemistry and fabrication practices.*

---

*The pressure vessel operating temperature is now expected to be about 204°C (400°F), and this change results in a much greater uncertainty relative to irradiation effects.

# 10. PLANT OPERATION AND MAINTENANCE (WBS 5104.01.06)

H. I. Bowers

## 10.1 INTRODUCTION

To assure that operation and maintenance (O&M) are considered early in the design of the modular HTGR concept, the U.S. Department of Energy (DOE) formally established the O&M Task Force, which is made up of representatives from Bechtel, GA Technologies, Inc., General Electric Company, Stone & Webster, Gas-Cooled Reactor Associates, and Oak Ridge National Laboratory (ORNL). The responsibilities of the Task Force are to provide ongoing guidance to the plant design as to the identification of requirements affecting O&M, to review and comment on plant design as it progresses and matures from the standpoint of O&M, and to audit O&M plans, procedures, and methods that evolve from the design. It is the specific responsibility of the Task Force to establish integrated staffing requirements for the plant and the projected O&M costs. The specific responsiblity of ORNL is to estimate the O&M costs through the use of staffing information supplied by the participating organizations along with cost estimating procedures developed earlier by ORNL for light-water reactor (LWR) plants.[1]

## 10.2 O&M COST ESTIMATE

The plant concept under consideration was the 4 × 250-MW(t) side-by-side steel vessel concept, utilizing pebble bed fuel, with two turbine-generator configurations: twin turbine generators and a single turbine generator.

The cost accounting breakdowns and cost estmates for the two configurations are given in Table 10.1. The direct costs encompass those expenses defined in nuclear power generation accounts 517 to 532 of the Federal Energy Regulatory Commission (FERC) code of accounts (18CFR101).

Table 10.1. Estimated total annual nonfuel operation and maintenance costs for the 4 × 250-MW(t) HTGR plant side-by-side steel vessel concept with pebble bed fuel

(January 1985 dollars)

| | Twin turbines | Single turbine |
|---|---|---|
| Plant capacity, MW(e) | 400 | 400 |
| Capacity factor, % | 80 | 80 |
| Annual generation, $10^6$ MWh | 2.8032 | 2.8032 |
| Onsite staff | 307 | 265 |
| Direct costs ($10^6$ \$/year) | | |
| Onsite staff | 13.5 | 11.7 |
| Maintenance materials | | |
| Fixed | 4.1 | 2.9 |
| Variable | 1.6 | 1.1 |
| Subtotal | 5.7 | 4.0 |
| Supplies and expenses | | |
| Fixed | 3.6 | 3.6 |
| Variable | 0.3 | 0.3 |
| Subtotal | 3.9 | 3.9 |
| NRC fees | 1.0 | 1.0 |
| Offsite support services | 2.5 | 2.5 |
| Subtotal direct costs | | |
| Fixed | 24.7 | 21.7 |
| Variable | 1.9 | 1.4 |
| Subtotal direct costs | 26.2 | 23.1 |
| Indirect costs ($10^6$ \$/year) | | |
| Administrative and general | 2.6 | 2.3 |
| Insurance | 4.5 | 4.5 |
| Subtotal indirect costs | 7.1 | 6.8 |
| Total direct and indirect costs ($10^6$ \$/year) | | |
| Fixed | 31.8 | 28.5 |
| Variable | 1.9 | 1.4 |
| Total | 33.7 | 29.9 |

The indirect costs encompass administrative and general accounts 928 to 932 as allocated to generation. Variable costs were allocated in two subaccounts: variable maintenance materials and variable supplies and expenses. All other accounts were considered fixed expenses.

The staffing estimates are those developed by the Task Force. A weighted average of all personnel – crafts, technical, engineering, and administrative and supervisory – was used in estimating the annual salary expense for nuclear power plant personnel. The annual cost of maintenance materials was estimated to be 90% of the annual cost of the total maintenance labor including supervision, crafts, and instrumentation and control (at 80% plant capacity factor). The estimates for supplies and expenses were based on judgment and comparison with LWRs. The NRC fees include estimated annual expenses for routine inspections, nonroutine inspections, and amendments (such as those for safety, environmental, and health physics inspections). Costs of offsite support services were based on the full-time services of a 25-person engineering staff. Estimates were included for the premiums associated with third-party liability insurance and plant property damage insurance. Administrative and general expenses were estimated to be 10% of the total direct O&M costs.

The total direct and indirect costs were estimated at $33.7 million/year for the twin-turbine plant and $29.9 million/year for the single-turbine plant, and the estimated unit costs were 12.0 mills/kWh and 10.7 mills/kWh, respectively, at 80% capacity factor. The higher costs for the twin-turbine plant were primarily due to higher personnel requirements for maintenance.

## 10.3 REFERENCE

1. M. L. Myers, L. C. Fuller, and H. I. Bowers, *Nonfuel Operation and Maintenance Costs for Large Steam-Electric Power Plants – 1982*, ORNL/TM-8324, September 1982.

# 11. REACTOR PHYSICS AND REACTOR SHIELDING (WBS 5210.04)

D. R. Vondy and D. T. Ingersoll

## 11.1 INTRODUCTION

There are two sections to this chapter; one summarizes the reactor physics work during CY 1985, and the other summarizes the reactor shielding efforts. The reactor physics section concerns the reactivity effects of water ingress into the core of a modular high-temperature gas-cooled reactor (HTGR), comparisons of reactivity calculations, and development of a core depletion-perturbation theory for simplifying reactor physics calculations. The reactor shielding section summarizes neutron fluences and radiation dose rates calculated for the pebble-bed-fueled HTGR and recent shielding calculations for the annular, prismatic-fueled HTGR. The shielding analyses are performed to provide design support to GA Technologies (GA) and to assist in specifying the reactor internals design so that component fluences and radiation dose rates do not exceed acceptable values.

## 11.2 REACTOR PHYSICS – D. R. Vondy

### 11.2.1 Reactivity Effects of Water Ingress Into the Reactor Core – D. R. Vondy

A study was made of the amount of reactivity addition to be expected from water ingress and the temperature rise required for compensation in a modular 250-MW(t) pebble-bed power reactor core.[1] Sample results are shown below for 800 K low-enriched uranium fuel with thorium:

| Water ingress | | | Compensating kernel |
|---|---|---|---|
| Fraction | kg | Δk/k | temperature (K) |
| 0.0002 | 49 | 0.0025 | 900 |
| 0.0004 | 98 | 0.0052 | 1030 |
| 0.0006 | 146 | 0.0075 | 1150 |
| 0.0008 | 195 | 0.0095 | 1290 |
| 0.01 | 244 | 0.0113 | 1420 |
| 0.0125 | 305 | 0.0135 | 1620 |
| 0.025 | 601 | 0.0195 | 2540 |
| 0.0375 | 915 | 0.0205 | 3100 |
| 0.05 | 1220 | 0.0185 | 3000 |

"Water fraction" is the fraction liquid equivalent in the coolant space, which is 0.39 fraction of the core. The compensation temperature rise is that of the kernels containing the fuel, considering no heating of the graphite moderator. These results are for a rapid water insertion. Further compensation comes from elevation of the graphite temperature, but delay is associated with the transport of heat. The amount of water that can enter the core must be established by assessment of the design, instrumentation, and operation details.

The temperature coefficient of reactivity decreases in magnitude with an increase in the amount of water present. Values of $T\partial k/k\partial T$ are shown here for a rise from 800 to 2000 K for the fueled kernel and, separately, for the moderator:

| Water fraction | Kernel | Moderator | Total |
|---|---|---|---|
| 0 | -0.0173 | -0.0545 | -0.0718 |
| 0 | -0.0090 | -0.0298 | -0.0388 |

A direct consequence of this decrease is a higher compensating temperature rise than would be predicted if the effect were ignored.

A number of reactor physics parameters were also studied. The presence of voids between the fuel pebbles causes neutron streaming. This increases the core leakage, and this effect is decreased by the presence of water in the coolant. Flattening of the radial power density distribution was found to reduce the reactivity addition associated with water ingress. Findings in the Federal Republic of Germany (FRG) that the reactivity effect of water ingress increases significantly with an increase in the fuel heavy-metal loading, and with a decrease in the carbon-to-heavy-metal ratio (C/HM), were confirmed.

The reactivity additions as a function of water ingress are predicted for the fuels of possible interest in Fig. 11.1.

There is concern about a loss in the worth of reflector control rods as a function of water ingress. The above relation was calculated, and the following results were obtained:

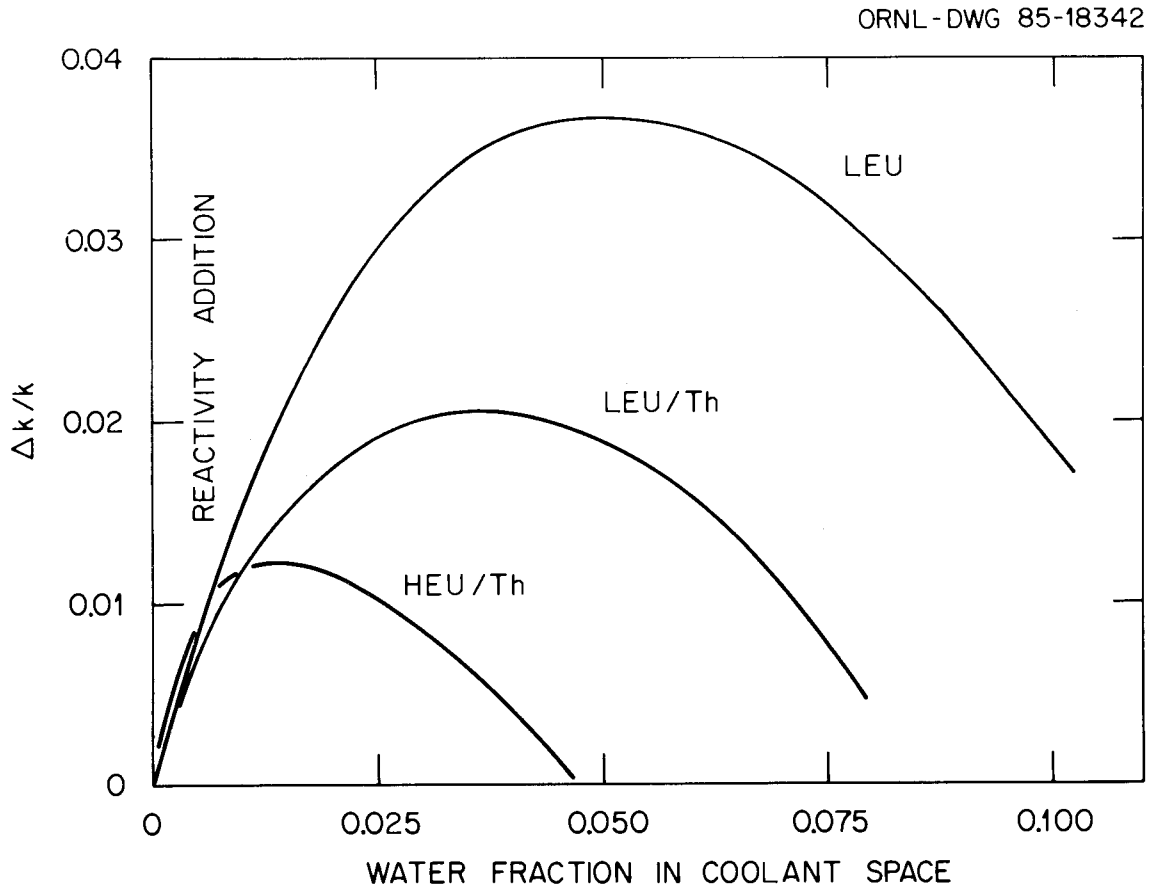


Fig. 11.1. Reactivity additions from water ingress to a modular pebble-bed core.

| Water ingress fraction | Relative control rod reactivity worth |
|---|---|
| 0 | 1.0 |
| 0.025 | 0.792 |
| 0.05 | 0.659 |
| 0.075 | 0.563 |
| (00) | 0.31 |

### 11.2.2 Comparisons of Reactivity Calculations – D. L. Moses

Calculations were done with ENDF/B-V cross sections to compare fuel cell results with those reported by others. Reasonable agreement was found with GA's results for highly enriched uranium with thorium fuel in the High Temperature Lattice Test Reactor (HTLTR) measurements.[2] The use of integral neutron transport methods in the resonance energy range also

produced results similar to those obtained by GA and the British (Winfrith) for low-enriched fuels, although the temperature defect for 300 to 1100 K was calculated to be 10 to 15% lower. Uncertainty remains about the effect of the presence of generated plutonium isotopes on the temperature coefficient of reactivity. Overall, there is a need for additional critical experiments involving temperature effects against which physics calculations can be benchmarked.

### 11.2.3 Depletion-Perturbation Theory Application – J. R. White

Application of depletion-perturbation theory continued in support of the HTGR. The equations to account for cross-section changes with depletion in the shielding factor form were formulated. Capability to apply the technique with the one-dimensional (1-D) GA code FEVER has been implemented and transmitted to GA.

## 11.3 REACTOR SHIELDING

### 11.3.1 Summary of 1985 Shielding Studies – D. T. Ingersoll

Three separate shielding studies were performed during 1985. The first two studies provided successive refinements to estimates of neutron fluences and radiation dose rates for the side-by-side steel-vessel pebble-bed-core HTGR design. Particular attention was given in the second study to the lower plenum and cross duct regions since fluence levels appeared to be excessive in these important areas. The third study, which was initiated only in the last month of the year, provided the first scoping-level analysis of fluence levels in the newly selected side-by-side steel-vessel annular prismatic-core HTGR design. In addition to the design-supporting analyses, a smaller effort was performed to couple gamma-ray cross sections to a 44-neutron-group cross-section set used in previous HTGR experiment analyses. The work conducted under each of the tasks is summarized in the sections that follow.

#### 11.3.1.1 Revised Radiation Levels for the Side-by-Side Steel-Vessel Pebble-Bed-Core HTGR – C. O. Slater

Preliminary estimates of radiation levels within and around the steel-vessel HTGR designs (vertical in-line and side-by-side) were made

and reported in December 1984 (ref. 3). The estimates were based on 1-D transport calculations using models that did not contain any boronation or other poison in the reflector surrounding the core. The lack of boronation together with several approximations imposed by the simplistic 1-D method led to relatively high radiation levels in the lower regions of the reactor and correspondingly high activation rates for the steam generator. These concerns prompted a more detailed analysis to refine the estimates of those radiation levels. The side-by-side concept, having been selected as the lead design, was the only design considered in the new study.

Calculations for this study were improved by using two-dimensional (2-D) transport methods, specifically, the DOT-IV (ref. 4) discrete ordinates computer code. However, because of time and budget constraints, several simplifications were required. These included compromises on the computational parameters (number of energy groups, angular quadrature, etc.) and compromises on the geometric model. The more severe model simplifications were in the lower plenum and cross duct regions, which have distinct three-dimensional aspects. Also, the four off-center fuel discharge chutes were necessarily represented as an annular ring containing the appropriate volume of fuel.

Design criteria for the reactor materials have not been firmly established; however, the assumed fluence limits were $10^{17}$ n/cm$^2$ for the thermal neutron fluence on the spring packs and $10^{19}$ n/cm$^2$ for the total neutron fluence on the vessel. The metal core support plate was assumed to withstand higher fluence limits (on the order of $10^{22}$ n/cm$^2$). Areas requiring maintenance or inspection by personnel should have dose rates less than 100 mrem/h one day after shutdown, although much lower rates are desirable. The lifetime dose limit for organic components is about $5 \times 10^8$ rad, and the temperature limit for the concrete is about 68°C (a radiation heating limit of 1.0 W/cm$^3$ was used). Most of these criteria were adopted from the 2240-MW(t) HTGR.

Several features of the design were studied, including the contribution of the fuel discharge chutes to the total fission neutron source and the effect of different amounts of boronation in the bottom reflector on the fluence levels in the lower regions. Despite obvious model differences, the 2-D results generally substantiated the 1-D results both at the

side and at the bottom of the vessel. The maximum total neutron fluence at the reactor vessel was determined to be approximately $5 \times 10^{18}$ n/cm$^2$, which is a factor of 2 below the design limit. However, uncertainties in the calculations were judged to be of at least that order; thus, additional shielding would likely be required. Shutdown dose rates were generally acceptably low, except in the cross duct region. More-detailed results are found in ref. 5.

### 11.3.1.2 Updated Radiation Levels at the Cross Duct and Lower Vessel Regions of the Pebble-Bed-Core HTGR - C. O. Slater

A more substantial shielding analysis was later performed to incorporate design changes that had occured and to better define radiation levels at the cross duct and in the lower vessel regions. Detailed results of the analysis are presented in ref. 6. As with the preceding analysis, 2-D discrete ordinates calculations were performed with the DOT-IV computer code using a 15-neutron-group/18-gamma-ray-group cross-section set. A higher order angular quadrature and cross-section Legendre expansion were used relative to the previous analysis. Calculations were performed for 2-D geometry models that either included or excluded a 360° opening in the side reflector and vessel at the hot-gas plenum level in order to simulate the main cross duct. The model with the opening is shown in Fig. 11.2. The case without the opening underestimates radiation transmission through the cross duct, while the case with the opening overestimates radiation transmission and gives a conservative upper limit for that transmission. The effects of radiation streaming through the bottom reflectors and the hot gas plenum were still not included, however.

Sources for the prompt neutron and gamma-ray calculations were obtained from core fission distributions modified to reflect the axial power profile supplied by GA. The decay gamma-ray source was obtained by using the ORIGEN-2 code (ref. 7) and equilibrium fission-product nuclide inventories provided by GA to produce gamma-ray spectra during operation (equilibrium) and for one day after shutdown. The decay gamma-ray source was normalized based on the average core power density and was assumed to be uniform within the core and the fuel discharge chutes. This results in a conservative source in the chutes since fuel balls in the chutes are actually in varying stages of decay.

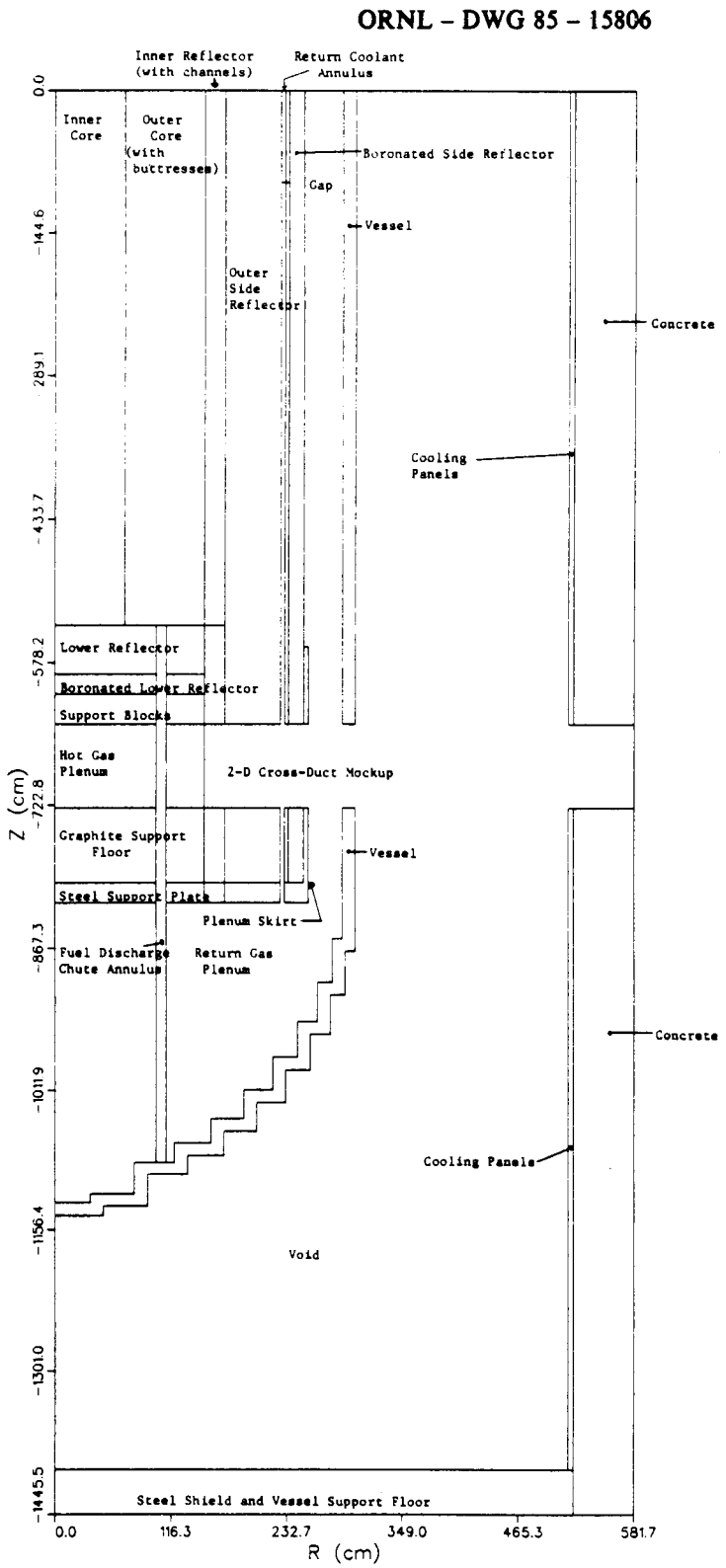


Fig. 11.2. Two-dimensional geometry model for calculations of radioactive levels in the lower regions of the side-by-side steel-vessel pebble-bed HTGR.

Table 11.1 shows radiation levels during operation, at shutdown, and for one day after shutdown at various locations throughout the reactor enclosure system. Figure 11.3 shows total-neutron fluence contours superimposed on the geometry model. Neutron fluences were generally higher than previous results due to streaming from the cross duct mockup. The streaming is evident in Fig. 11.3. Reactor vessel and spring pack fluence limits were exceeded in some instances due to streaming through the cross duct mockup and through the void annulus inside and outside the vessel side wall. The thermal-neutron fluence increased relative to the previous results because of the inclusion of the surrounding concrete wall.

Table 11.1. Maximum radiation levels at various locations in the lower regions of the side-by-side steel-vessel small HTGR

| Radiation type | Units | Radiation level | | Present/previous |
|---|---|---|---|---|
| | | Present | Previous | |
| **Neutron fluences at spring pack at core level** | | | | |
| Total neutron | $n/cm^2$ | 5.4 + 18[a] | 4.4 + 18 | 1.2 |
| E > 0.9 MeV | $n/cm^2$ | 3.2 + 17 | 2.0 + 17 | 1.6 |
| 0.1 < E < 0.9 MeV | $n/cm^2$ | 1.1 + 18 | 5.1 + 17 | 2.2 |
| 3.05 eV < E < 0.1 MeV | $n/cm^2$ | 4.0 + 18 | 2.5 + 18 | 1.6 |
| Thermal | $n/cm^2$ | 1.3 + 18[b] | 7.0 + 15 | 186.0 |
| **Neutron fluences at vessel side wall at core level** | | | | |
| Total neutron | $n/cm^2$ | 4.9 + 18 | 3.9 + 18 | 1.3 |
| E > 0.9 MeV | $n/cm^2$ | 2.7 + 17 | 1.0 + 17 | 2.7 |
| 0.1 < E < 0.9 MeV | $n/cm^2$ | 9.8 + 17 | 4.0 + 17 | 2.5 |
| 3.05 eV < E < 0.1 MeV | $n/cm^2$ | 3.7 + 18 | 2.0 + 18 | 1.9 |
| Thermal | $n/cm^2$ | 1.7 + 18[b] | 1.4 + 16 | 120.0 |
| **Neutron fluences at vessel side wall at cross duct level** | | | | |
| Total neutron | $n/cm^2$ | 5.6 + 19 | 2.0 + 17 | 280.0 |
| E > 0.9 MeV | $n/cm^2$ | 3.0 + 17 | 5.1 + 15 | 58.8 |
| 0.1 < E < 0.9 MeV | $n/cm^2$ | 7.9 + 17 | 5.1 + 16 | 15.5 |
| 3.05 eV < E < 0.1 MeV | $n/cm^2$ | 3.1 + 18 | 2.0 + 17 | 15.5 |
| Thermal | $n/cm^2$ | 5.2 + 19 | 1.0 + 15 | 5.2 + 4 |
| **Neutron fluences at vessel bottom** | | | | |
| Total neutron | $n/cm^2$ | 3.4 + 17 | 1.1 + 17 | 3.1 |
| E > 0.9 MeV | $n/cm^2$ | 9.1 + 15 | 1.0 + 15 | 9.1 |
| 0.1 < E < 0.9 MeV | $n/cm^2$ | 7.1 + 16 | 4.0 + 16 | 1.8 |
| 3.05 eV < E < 0.1 MeV | $n/cm^2$ | 1.9 + 17 | 7.0 + 16 | 2.7 |
| Thermal | $n/cm^2$ | 3.2 + 17[b] | 5.0 + 15 | 64.0 |

Table 11.1. (continued).

| Radiation type | Units | Radiation level | | Present/previous |
|---|---|---|---|---|
| | | Present | Previous | |
| **Neutron fluences at the steel support plate** | | | | |
| Total neutron | $n/cm^2$ | 2.3 + 19 | 5.0 + 19 | 0.46 |
| E > 0.9 MeV | $n/cm^2$ | 6.6 + 17 | 1.0 + 18 | 0.66 |
| 0.1 < E < 0.9 MeV | $n/cm^2$ | 1.3 + 18 | 2.0 + 18 | 0.65 |
| 3.05 eV < E < 0.1 MeV | $n/cm^2$ | 3.1 + 18 | 5.1 + 18 | 0.61 |
| Thermal | $n/cm^2$ | 1.8 + 19 | 5.0 + 19 | 0.36 |
| **Radiation heating in concrete at core level** | | | | |
| Operation | $mW/cm^3$ | 3.2 − 2<br>(3.2 − 2)[c] | | |
| At shutdown | $mW/cm^3$ | 1.0 − 3 | | |
| At one-day decay | $mW/cm^3$ | 1.0 − 4 | | |
| **Radiation heating in concrete at cross duct level** | | | | |
| Operation | $mW/cm^3$ | 0.4 (0.1)[c] | | |
| At shutdown | $mW/cm^3$ | 0.3 | | |
| At one-day decay | $mW/cm^3$ | 3.2 − 2 | | |
| **Radiation heating in steel support plate** | | | | |
| Operation | $mW/cm^3$ | 1.0 + 2<br>(0.32)[c] | | |
| At shutdown | $mW/cm^3$ | 1.0 + 2 | | |
| At one-day decay | $mW/cm^3$ | 3.2 + 1 | | |
| **Dose rate at cross duct junction with vessel** | | | | |
| Operation | rad/h | 1.3 + 5<br>(3.2 + 4)[c] | 1.5 + 3<br>(1.5 + 3)[c] | 86.7 (21.3)[c] |
| At shutdown | rad/h | 1.0 + 5 | 1.4 + 1 | 7.1 + 3 |
| At one-day decay | rad/h | 3.2 + 4 | 1.2 | 2.7 + 4 |
| **Dose rate below steel shield below vessel** | | | | |
| Operation | rad/h | 1.1 + 1<br>(1.0 + 1)[c] | 5.8 − 1<br>(5.8 − 1)[c] | 19.0 (17.2)[c] |
| At shutdown | rad/h | 1.0 | 8.4 − 8 | 1.2 + 7 |
| At one-day decay | rad/h | 1.0 − 2 | 7.0 −9 | 1.4 + 6 |

[a]Read as $5.4 \times 10^{18}$.

[b]The peak thermal neutron fluences do not occur at the same location as the peaks for the other fluences.

[c]Value in parentheses is that due to prompt neutrons and gamma rays.

ORNL – DWG 85 – 15808

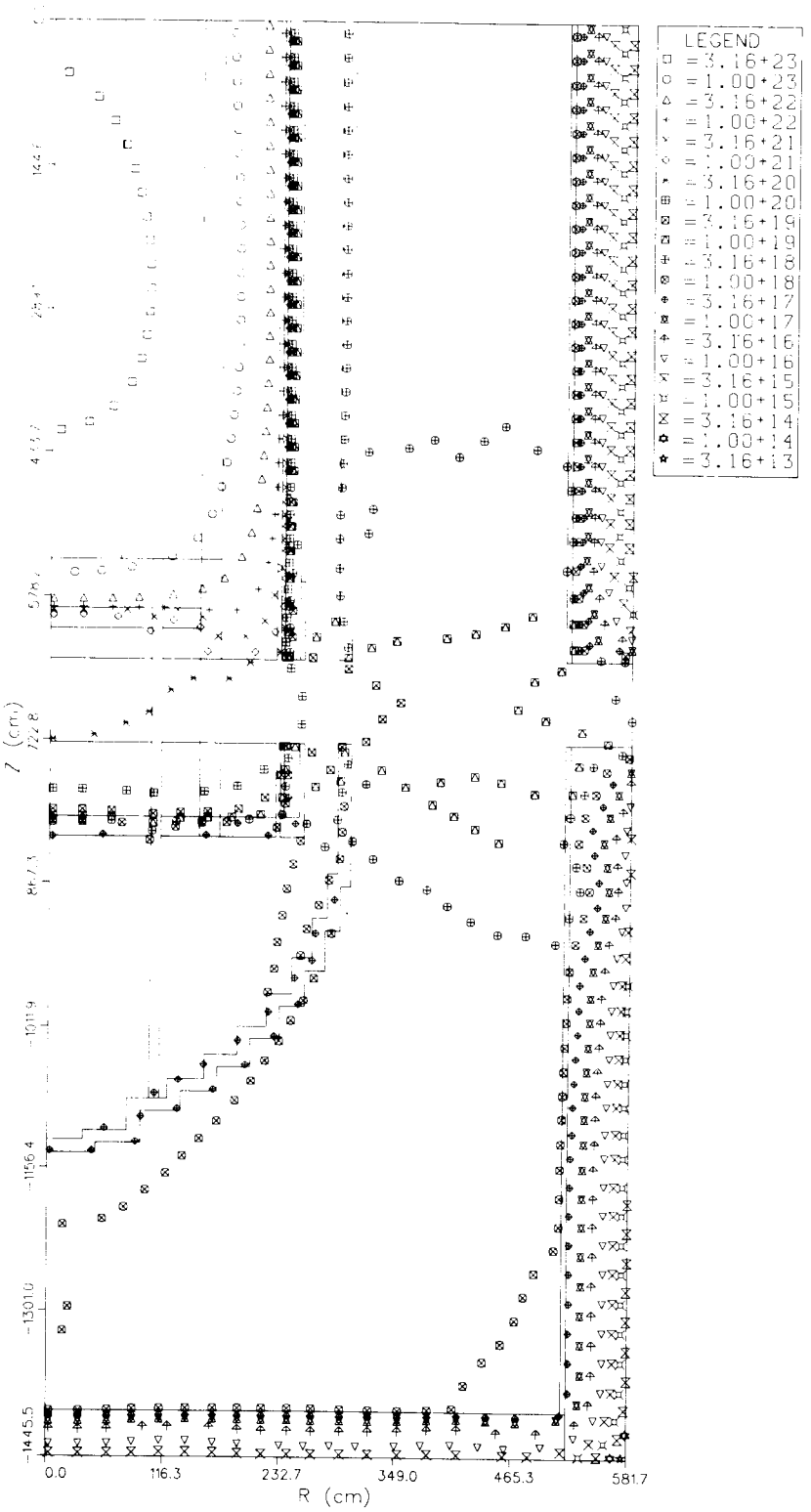


Fig. 11.3. Total neutron fluence (32 full-power years) contours for a two-dimensional mockup of the lower regions of the side-by-side steel-vessel pebble-bed HTGR.

The decay gamma-ray dose rates near the cross duct are also much higher because of the more conservative source in the fuel discharge chute mockup. The dose rate at the cross duct one day after shutdown is seen to be very high, decreasing only about a factor of 30 when the cross duct was not modeled. Decay gamma-ray sources in the portions of the fuel discharge chutes in the return-gas plenum are responsible for these increases. The addition of shielding material along the vessel wall and around the chutes as well as a more representative decay gamma-ray source definition for the chutes were suggested as possible means for reducing the dose rates. Time did not permit sufficient study of the shielding and source options.

#### 11.3.1.3 Initial Analysis for the Side-By-Side Steel-Vessel Annular Prismatic-Core HTGR - J. A. Bucholz

A series of 1-D shielding calculations were performed to support the design of reactor internals for the side-by-side steel-vessel annular prismatic-core HTGR. Detailed results of initial neutron fluence calculations are described in a letter report[8] and are summarized below.

Primary points of interest in the 1-D shielding analyses included the core barrel, the reactor vessel, the cross duct, the core support plate, and the decay heat exchanger. One-dimensional transport calculations were supplemented by experimental correlations to obtain streaming correction factors for the coolant holes in the lower reflector, and semianalytical techniques were used to estimate the effect of streaming from the core barrel, reactor vessel, and concrete shield down to the cross duct. The primary objective of these studies was to determine the effectiveness of various shielding design options, such as varying the number of rows of borated steel pins in the outer side reflector and providing additional boronation in the lower portion of the post blocks and in the graphite floor of the plenum. Use of borated steel pins in lieu of boronated graphite pins in the lower reflector and plenum floor was also examined. Later 2-D results are expected to differ somewhat from the preliminary results obtained here, especially in the lower plenum region and at the cross duct.

Prompt gamma sources and capture gamma sources were accurately accounted for in the coupled neutron/gamma shielding analysis. Decay

gamma source terms under steady state conditions were not available but were accounted for in an approximate fashion by doubling the prompt and capture gamma source terms. Decay gamma source terms one day and ten days after shutdown were based on the Borst-Wheeler equation. Revised estimates of the gamma heating and dose rates will be provided when the decay gamma source term data become available.

Results for the nominal case (near top section of the core, with six rows of borated steel pins in side reflector) are as follows:

1. Total fluence on inner surface of core barrel is $5.5 \times 10^{17}$ n/cm$^2$, with a thermal fluence of $1.8 \times 10^{16}$ n/cm$^2$. These results assume full power operation for 32 years, that is, $T = 1.01 \times 10^9$ s. Corresponding total and thermal fluences on the outer surface are $3.2 \times 10^{17}$ and $3.4 \times 10^{15}$ n/cm$^2$. Without borated steel pins in the outer reflector, the thermal fluence here and on the inner surface of the reactor vessel would be four orders of magnitude greater. The first two rows of borated steel pins are responsible for the bulk of the attenuation. While additional rows of pins will attenuate the flux only an additional 10 to 50%, four or more rows should be used to prevent excessive neutron streaming between the staggered rows of individual pins.
2. On the inner surface of the reactor vessel, the total and thermal fluences are $3.2 \times 10^{17}$ and $3.4 \times 10^{15}$ n/cm$^2$; on the outer surface of the reactor vessel, the corresponding values are $8.2 \times 10^{16}$ and $2.2 \times 10^{16}$ n/cm$^2$. Most of the thermal fluence on the outside of the reactor vessel is due to fast and epithermal neutrons that leak from the reactor, pass through the vessel, thermalize in the concrete wall of the surrounding vault, and scatter back toward the vessel. Thus, at this location, the thermal fluence is almost independent of any boronation that might be present in the outer side reflector.
3. Total and thermal fluences on the upper surface of the core support plate are $6.1 \times 10^{15}$ and $5.8 \times 10^{14}$ n/cm$^2$. These estimates are based on a fully boronated design and assume a streaming correction factor of 20 for all energy groups.
4. The cross duct fluence depends on four primary components:
   (a) neutrons streaming down between the reactor vessel and the

concrete vault, (b) neutrons streaming down between the core barrel and the reactor vessel, (c) neutrons entering the hot duct from the hot-gas plenum, and (d) neutrons reaching the cross duct via diffusion through the side reflector. (This last component was considered minimal and may be significantly reduced by boronation; accurate estimates of this component would also require a more complex 2-D analysis.) The total cross duct centerline fluence was estimated as $1.5 \times 10^{17}$ n/cm$^2$, with a thermal fluence of $1.8 \times 10^{15}$ n/cm$^2$. Approximately 80% of the neutrons reaching this point come from the hot-gas plenum, while only about 20% come from outside the vessel. Additional attenuation of the fast and epithermal neutrons will be required if the total fluence in this area is to be reduced further.

5. A total peak fluence of $7.9 \times 10^{17}$ n/cm$^2$ was estimated for the top portion of the decay heat exchanger. The corresponding thermal fluence here is $4.1 \times 10^{17}$ n/cm$^2$. Results in this region, along the sides of the decay heat exchanger, and in the bottom portion of the reactor vessel are expected to be extremely sensitive to a number of multidimensional streaming effects and will require a detailed 2-D analysis.
6. Estimates of the fluence in the top of the reactor vessel are given in ref. 8 but are still subject to a number of uncertainties: (a) the upper core internals were not included in the model due to lack of available design data, (b) no design efforts had been taken to shield the top reactor head, and (c) streaming corrections were not estimated for the control assembly penetrations and poison ball holes.

Clearly, more refined analyses will be required to reduce the uncertainties resulting from the simplistic methods used in this scoping analysis. Additional work will also be needed as input for design revisions and refinements.

#### 11.3.1.4 Coupled Neutron and Gamma-Ray Cross Sections – C. O. Slater

The shielding analysis of the steel-vessel HTGR was performed with a 15-neutron-group/18-gamma-ray-group library used with the SCALE system.[9] The 13 thermal-neutron groups were collapsed to 1 group to eliminate the

need for multiple outer iterations required to converge upscatter in fixed-source shielding calculations. The library had previously been prepared for the analysis of the 2240-MW(t) HTGR[10] and was thus readily available; however, the neutron portion of the library was found to be somewhat inferior when used to analyze an HTGR shielding experiment.[11] A neutron cross-section library with a finer group structure (44 groups with upscattering among the bottom 4 thermal groups) was developed specifically for the analysis of the experiment and gave better results than did the 15-neutron-group set. Unfortunately, it did not have coupled gamma-ray cross sections required for the HTGR design analyses. Hence, a separate task was defined to couple gamma-ray cross sections with the 44-neutron-group set.

The task was performed by using various modules of the AMPX cross-section processing system[12] to collapse data from a 227-neutron-group ENDF/B-V master library[13] and also to couple the neutron groups to the existing 18-gamma-ray-group library. The task was completed with some difficulty owing primarily to the lack of gamma-ray production and interaction data in the main data files for some of the nuclides. The resulting library contains cross sections for 47 materials, and each cross-section set has Legendre expansion coefficients to third order. The ANISN-formatted 44-neutron-group/18-gamma-ray-group library is suitable for general application to HTGR-related shielding problems and is available for distribution to any of the program participants.

## 11.4 REFERENCES

1. D. R. Vondy and R. D. Timmerman, *Estimated Reactivity Effects from Water Ingress and Temperature Changes for a Modular Pebble Bed HTR Core*, ORNL-9716 (in publication).

2. K. R. Shultz and D. R. Mathews, *General Atomic Participation in the High Temperature Lattice Test Reactor Program*, GA-A12710, GA Technologies, San Diego, Calif., 1976.

3. C. O. Slater, *Preliminary Studies of Shielding Aspects of the Steel Vessel Modular Reactor Systems Concepts*, December 21, 1984, unpublished data.

4. W. A. Rhoades et al., *The DOT-IV Two-Dimensional Discrete Ordinates Transport Code with Space-Dependent Mesh and Quadrature*, ORNL/TM-6529, 1979.

5. C. O. Slater, *Preliminary Shielding Analyses for the Side-by-Side Steel Vessel HTGR*, HTGR-85-050, July 1985.

6. C. O. Slater, *Updated Analysis of the Core Support Plate, Cross Duct, and Lower Vessel Regions of the Modular Pebble-Bed Reactor*, HTGR-85-161 (ORNL/TM-9848), Nov. 1985.

7. O. W. Hermann and R. M. Westfall, "ORIGEN-S: SCALE System Module to Calculate Fuel Depletion, Actinide Transmutation, Fission Product Buildup and Decay, and Associated Radiation Source Terms," Section F7 in *SCALE: A Modular Code System for Performing Standardized Computer Analyses for Licensing Evaluation*, ed. C. V. Parks, NUREG/CR-0200 (ORNL/NUREG/CSD-2/V3/R2), 1984.

8. J. A. Bucholz to P. R. Kasten, "Results of Initial 1-D Shielding Analysis for the 350-MW(th) Annular Prismatic HTGR Core," internal correspondence, Jan. 17, 1986.

9. R. M. Westfall, "Neutron Cross Section Libraries," Section M4 in *SCALE: A Modular Code System for Performing Standardized Computer Analyses for Licensing Evaluation*, ed. C. V. Parks, NUREG/CR-0200 (ORNL/NUREG/CSD-2/V3/R2), 1984.

10. C. O. Slater and S. N. Cramer, *Survey Analysis of Radiation Levels in the HTGR Lower Regions*, ORNL/TM-8141, 1982.

11. C. O. Slater, *Analysis of Phase I of the HTGR Bottom Reflector and Core Support Block Neutron-Streaming Experiment*, ORNL/TM-9252, 1984.

12. *AMPX-II, Modular Code System for Generating Coupled Multi-group Neutron-Gamma-Ray Cross Section Libraries from Data in ENDF Format*, RSIC Computer Code Collection, Peripheral Shielding Routines, PSR-63, 1978.

13. W. E. Ford, III, B. R. Diggs, L. M. Petrie, C. C. Webster, and R. M. Westfall, *CSRL-V: Processed ENDF/B-V 227-Neutron-Group and Pointwise Cross-Section Libraries for Criticality Safety, Reactor and Shielding Studies*, NUREG/CR-2306 (ORNL/CSD/TM-160), 1982.

# 12. ADVANCED SYSTEM DESIGN SUPPORT (WBS 6600)

P. L. Rittenhouse

## 12.1 INTRODUCTION

Work in this area involves assessment of high-temperature metallic materials and development of materials design methods for use at the very high temperatures characteristic of the high-temperature gas-cooled reactor (HTGR) reformer system. The first activity is needed to assist in selection of alloys for construction of components exposed to the high-temperature (950°C) core exit helium; the latter is required because such high temperatures are not currently covered in accepted American Society of Mechanical Engineers (ASME) design codes.

## 12.2 ADVANCED METALLIC MATERIALS (WBS 6600.03)

### 12.2.1 Advanced Materials Technology Assessment – M. K. Booker and P. L. Rittenhouse

The HTGR reformer system as currently envisioned is based on studies completed by General Electric Company for the U.S. Department of Energy (DOE) in 1982. These studies involved both the economics of the system/process and the plant design. It was determined that a reformer system with reformer tube life of 100,000 h at 950°C should be economically viable. Inconel 617 was chosen as the reference material for the reformer tubes.

Near the end of 1985, Oak Ridge National Laboratory (ORNL) began a multitask study to assess and evaluate HTGR materials technology as applied to the reformer system. The elements of the study are

1. review and evaluation of existing materials property requirements,
2. review and evaluation of foreign advanced materials technology,
3. development of selection criteria for HTGR advanced materials,

4. development of a logic for selection and qualification of advanced materials, and
5. preparation of a strategy for development of new materials.

The results of the ORNL study will be presented to a Peer Review Panel whose prime responsibility will be to judge the suitability of Inconel 617 for the HTGR reformer tube application. The study is scheduled to be completed in August 1986.

### 12.2.2 Creep and Thermal Stability of Advanced Alloys – H. E. McCoy

Studies initiated prior to 1985 on several advanced alloys were completed, and the results were summarized in a topical report.[1] Small quantities of bar stock of GASM alloy GA 911 (Ni–8% Cr–10% Mo–2% Al–2% Ti) and GA 912 (Ni–8% Cr–10% W–2% Al–2% Ti) were provided by GA Technologies for testing. These alloys were quite strong at the lower test temperature of 850°C, but they were weaker than Inconel 617 and HD 556 at 950°C. These alloys seemed to resist carburization, and there was very little evidence of carbon change in the test samples.

Small heats of three modifications of Inconel 617 containing from 12 to 22% chromium and 2% titanium were obtained commercially as 1/2-in.-thick plate. The three alloys had about the same creep strength and were slightly weaker than standard Inconel 617. The lower strength may have been due to the modified alloys being cleaner. The modified alloys generally have very high fracture strains, but the room temperature impact results show that they are subject to an aging reaction that peaks at 704°C and decreases in magnitude with decreasing chromium content. The lowest value obtained was 24 J for the alloy containing 22% chromium after aging 10,000 h at 704°C. This is close to the values noted for standard Inconel 617. There was considerable scatter in the posttest carbon analyses, such that it is very uncertain whether any of the alloys were carburized. Standard Inconel 617 would carburize under these conditions, and the difference in behavior is attributed to the 2% titanium in the modified alloys rather than the variations in the chromium concentration.

IN-519 is a very special alloy that could be used for some parts that could be centrifugally cast. The alloy normally contains about 1.5% niobium. We statically cast samples containing niobium and one containing

titanium, but the properties of the material containing 1.5% niobium were the most desirable. The creep data for these two alloys are limited, but the niobium-containing alloy appears to be almost as strong as the high-nickel alloys. These alloys contain about 0.3% chromium, and no change could be detected following exposure to HTGR-He.* Six test samples reached 5500 h at 871°C, and the carbon concentration varied only ±8% from the initial value. Thus, these alloys seem quite resistant to carburization.

Cabot alloy 214 is a developmental alloy and contains a small amount of yttrium for oxidation resistance. Our tests indicated that the alloy undergoes an aging reaction very rapidly at 871°C and more slowly at lower temperatures. The aging reaction results in Charpy V impact energies as low as 11.6 J. At high stresses, alloy 214 creeps more slowly than Hastelloy X, but alloy 214 is weaker at lower stresses than Hastelloy X. The weld metal in this alloy was quite weak, and samples with transverse welds failed at low stresses. Carbon was analyzed only for a creep sample exposed to HTGR-He for 5759 h at 871°C, and the carbon content increased from 360 to 3800 ppm. Thus the carburization rate appears to be quite high.

## 12.3 NUCLEAR HEAT SYSTEM DESIGN CRITERIA (WBS 6600.01) – J. J. Blass

The objective of this task is to perform an assessment of the applicability of ASME Code Case N-47 to very-high-temperature reactor (VHTR) components and to identify shortcomings and development needs.

The current design methodology for Class 1, high-temperature reactor (HTR) system components is embodied in the criteria of ASME Code Case N-47 (ref. 2) and in the design requirements and guidance of NE standards F 9-4T (ref. 3) and F 9-5T (ref. 4). This methodology is currently limited primarily to liquid metal fast breeder reactor (LMFBR) materials and to temperatures not exceeding 815°C (1500°F) for types 304 and 316 stainless steels, 760° (1400°F) for alloy 800H, and 650°C (1200°F) for 2.25Cr-1Mo steel. In general, the methodology is based on a design-by-analysis concept addressing the several possible failure modes in high-temperature service: (1) ductile rupture from short-term loadings, (2) creep rupture

*A mixture of helium and other gases that simulates the impure helium found in an operating HTGR.

from long-term loadings, (3) creep-fatigue failure, (4) gross distortion due to incremental collapse and ratchetting, (5) loss of function due to excessive deformation, (6) buckling due to short-term loadings, and (7) creep buckling due to long-term loadings. The methodology includes many contributions in terms of both development and validation from the High-Temperature Structural Design Technology Program of ORNL.

The approach taken in this task is to develop further the existing LMFBR high-temperature design methodology for the particular alloys and conditions of interest in the very-high-temperature gas-cooled reactor (VHTGR). This will be accomplised in concert with the Task Force on Very High Temperature Design (TF-VHTD) established in March 1983 within the ASME code organization. The task force is to formulate design rules and procedures for Class 1 components of helium-cooled nuclear reactor plants operating at temperatures to 950°C (1742°F). A draft compilation of design rules is scheduled for completion by October 1989.

The rules will cover metal pressure boundary components designed for 20- to 40-year service. The materials receiving primary emphasis are alloy 800H, Hastelloy X, and Inconel 617. Secondary emphasis will be given to Inconel 618 and Nimonic 86. The rules will be consistent with applicable guidelines, will recognize inherent HTR characteristics (e.g., slow temperature changes), will differentiate between safety goals and economic goals, will avoid nonpertinent precedents, and will establish margins on a rational basis.

Based on Task Force deliberations thus far, significant departures from the ASME high-temperature Code Case N-47 are expected. Among these are inclusion of effects of aging on strength and ductility, elimination of the tertiary creep criterion from the time-dependent stress allowable, establishment of strain limits based on analysis of experimental data, modification of elastic ratchetting and creep fatigue rules to include rapid stress relaxation effects, consideration of mechanical behavior exhibiting little strain hardening, and explicit coverage of the effects of pernicious environments.

The Task Force has formulated an action plan, together with assignments of responsibility, to address key areas that have been identified for the development of very-high-temperature design rules. One of the

most important primary needs relates to obtaining valid representations of inelastic material behavior. Traditionally, "time-independent" stress-strain curves and time-dependent creep curves are represented and used, both in establishing allowables and in rules for guarding against excessive structural ratchetting. However, for the alloys and temperatures involved in VHTGRs, this distinction between time-independent and time-dependent behavior blurs; all behavior is time- and rate-dependent. To properly characterize such behavior, a so-called unified, or viscoplastic, constitutive model is needed. Such a model would readily describe both short- and long-term material behavior as a function of loading rate. It would have the bonus of describing multiaxial behavior and material response to time-varying thermal and mechanical loads. Thus, the unified representation would provide not only the information required for Code rule development but also the constitutive theory required for use in design analyses. Since ORNL developed a unified model under the liquid-metal reactor program, it was assigned responsibility for adapting that model to the VHTGR alloys.

The effort will consist of gathering available data from U.S. and foreign sources and of fitting the model to the data. First priority will be given to Inconel 617, then alloy 800H, and finally Hastelloy X. Temperatures to 950°C (1742°F) will be considered, where data are available. Data shortcomings and needs will be identified to the materials programs. The values of certain parameters in the model will be adjusted, and other refinements will be made in order to obtain an acceptable fit to the data. A computer program has been written to help accomplish this; it is based on a nonlinear, least-squares technique and numerical integration of the partial differential equations employed in the unified model. When an acceptable model has been obtained, then isochronous stress-strain curves for Code use will be generated, and Code ratchetting rules will be examined.

## 12.4 REFERENCES

1. H. E. McCoy, *Evaluation of Advanced Alloys for Gas-Cooled Reactors*, ORNL/TM-9891, February 1986.

2. Case N-47-22, "Class 1 Components in Elevated Temperature Service," Sect. III, Div. 1, *Cases of ASME Boiler and Pressure Vessel Code*, American Society of Mechanical Engineers, New York, April 5, 1984.

3. NE Standard F 9-4T, *Requirements for Design of Class 1 Elevated Temperature Nuclear System Components (Supplement to ASME Code Case N-47)*, U.S. Department of Energy, February 1984.

4. NE Standard F 9-5T, *Guidelines and Procedures for Design of Class 1 Elevated Temperature Nuclear System Components*, U.S. Department of Energy, March 1981.

HTGR-86-057
ORNL-6300
Distribution
Category UC-77T

## INTERNAL DISTRIBUTION

1–2. Central Research Library
3. Document Reference Section
4–5. Laboratory Records Department
6. Laboratory Records, ORNL RC
7. ORNL Patent Section
8. J. J. Blass
9. H. I. Bowers
10. D. G. Cacuci
11. J. C. Cleveland
12. J. M. Corum
13–15. W. P. Eatherly
16. R. L. Fellows
17. U. Gat
18. J. R. Hightower
19. L. B. Holland
20. D. T. Ingersoll
21. J. E. Jones Jr.
22–26. M. J. Kania
27–36. P. R. Kasten
37. C. R. Kennedy
38. J. F. King
39. D. A. Lee
40. F. C. Maienschein
41. J. C. Mailen
42. R. W. McClung
43. H. E. McCoy
44. D. L. Moses
45. F. R. Mynatt
46. D. J. Naus
47. M. F. Osborne
48. H. Postma
49–53. P. L. Rittenhouse
54. G. C. Robinson
55. J. P. Sanders
56. R. L. Senn
57. C. O. Slater
58. G. M. Slaughter
59. J. O. Stiegler
60. R. A. Strehlow
61. J. P. Strizak
62–64. P. T. Thornton
65. H. E. Trammell
66. D. B. Trauger
67. D. R. Vondy
68. C. D. West
69. R. P. Wichner
70. R. G. Wymer
71. G. T. Yahr

## EXTERNAL DISTRIBUTION

72–74. DOE, DIVISION OF HTGRs, NE-531, Washington, DC 20545

A. C. Millunzi, Acting Director
J. E. Fox
A. S. Mehner

75. DOE, OFFICE OF ADVANCED REACTOR PROGRAMS, NE-53, Washington, DC 20545

Director

76. DOE, SAN, 1333 Broadway, Oakland, CA 94612

J. Muhlestein

77. DOE, OAK RIDGE OPERATIONS OFFICE, P.O. Box E,
Oak Ridge, TN 37831

Office of Assistant Manager for Research and Development
ATTN: S. W. Ahrends/M. J. Rohr

78-136. DOE, TECHNICAL INFORMATION CENTER, P.O. Box 62,
Oak Ridge, TN 37831

For distribution as shown in TIC-4500, Distribution Category
UC-77T (Gas-Cooled Reactor Technology)